Magnetic dynamics in iron-based superconductors probed by neutron spectroscopy

Alice E. Taylor

Jesus College

Magnetic dynamics in iron-based superconductors probed by neutron spectroscopy

Alice E. Taylor
Jesus College, University of Oxford
DPhil Thesis, Trinity Term 2013

Abstract

This thesis describes inelastic neutron scattering (INS) experiments on several iron-based materials. The experiments were primarily designed to investigate the link between magnetic dynamics and superconductivity. The work contributes to evidence that magnetic fluctuations influence or are influenced by superconductivity. It is demonstrated that the INS response of a material, in conjunction with theoretical models, can provide valuable information about both superconductivity and magnetism.

I measured the magnetically ordered parent-compound $SrFe_2As_2$ to investigate the nature of magnetism in iron-based systems. Comparison of the data to models based on both itinerant and localised magnetism showed that an itinerant model offers the best description of the data.

LiFeAs is a superconductor that shows no magnetic order, however I was able to distinguish a magnetic signal in its INS spectrum. The signal is consistent with the magnetic resonance observed in several other iron-based superconductors. This indicates that LiFeAs likely hosts an $s_{\pm}$ gap symmetry.

I investigated two iron-phosphide systems, LaFePO and Sr_2ScO_3FeP, and in this case I was unable to identify any magnetic scattering. Comparison to LiFeAs showed that any signal in LaFePO is at least 7 times weaker. These results suggest that magnetic fluctuations are not as influential to the electronic properties of iron-phosphide systems as they are in other iron-based superconductors.

In $Cs_xFe_{2-y}Se_2$ I found two independent signals that appear to be related to phase-separated magnetic and superconducting regions of the sample. I showed that fluctuations associated with the magnetically ordered phase are consistent with localised magnetism, and do not respond to superconductivity. The second signal, however, increases in intensity below the superconducting transition temperature $T_c = 27\,\mathrm{K}$, consistent with a magnetic resonance. This could be indicative of a pairing symmetry in $Cs_xFe_{2-y}Se_2$ that is distinct from most other iron-based superconductors.

Finally, the molecular intercalated FeSe compound $Li_{0.6}(ND_2)_{0.2}(ND_3)_{0.8}Fe_2Se_2$ revealed strong magnetic fluctuations. Again the signal was consistent with a magnetic resonance responding to $T_c = 43\,\mathrm{K}$. The results suggest that $Li_x(ND_2)_y(ND_3)_{1-y}Fe_2Se_2$ is similar to the superconducting phase of $Cs_xFe_{2-y}Se_2$, placing constraints on theoretical models to describe the molecular intercalated FeSe compounds.

Acknowledgements

Contents

Publications

- A. E. Taylor, R. A. Ewings, T. G. Perring, D. R. Parker, J. Ollivier, S. J. Clarke, and A. T. Boothroyd.
  Absence of strong magnetic fluctuations in the FeP-based systems LaFePO and Sr_2ScO_3FeP
  J. Phys.: Condens. Matter **25**, 425701 (2013).

- A. E. Taylor, S. J. Sedlmaier, S. J. Cassidy, E. A. Goremychkin R. A. Ewings, T. G. Perring, S. J. Clarke, and A. T. Boothroyd.
  Spin fluctuations away from $(\pi, 0)$ in the superconducting phase of molecular-intercalated FeSe
  Phys. Rev. B **87**, 220508(R) (2013).

- A. E. Taylor, R. A. Ewings, T. G. Perring, J. S. White, P. Babkevich, A. Krzton-Maziopa, E. Pomjakushina, K. Conder, and A. T. Boothroyd.
  Spin-wave excitations and superconducting resonant mode in $Cs_xFe_{2-y}Se_2$
  Phys. Rev. B **86**, 094528 (2012).

- A. E. Taylor, M. J. Pitcher, R. A. Ewings, T. G. Perring, S. J. Clarke, and A. T. Boothroyd.
  Antiferromagnetic spin fluctuations in LiFeAs observed by neutron scattering
  Phys. Rev. B **83**, 220514(R) (2011).

- R. A. Ewings, T. G. Perring, J. Gillett, S. D. Das, S. E. Sebastian, A. E. Taylor, T. Guidi, and A. T. Boothroyd.
  Itinerant spin excitations in $SrFe_2As_2$ measured by inelastic neutron scattering
  Phys. Rev. B **83**, 214519 (2011).

Definitions

Definitions of acronyms and initialisms

AFM	Antiferromagnetic
ARPES	Angle-resolved photoemission spectroscopy
BZ	Brillouin zone
FC	Field-cooled
FM	Ferromagnetic
f.u.	Formula unit
FWHM	Full-width at half-maximum
ILL	Institut Laue–Langevin
INS	Inelastic neutron scattering
μSR	Muon spin rotation
NMR	Nuclear magnetic resonance
r.l.u.	Reciprocal lattice unit
SDW	Spin density wave
SQUID	Superconducting quantum interference device
ToF	Time-of-flight
2D	Two-dimensional
XRPD	X-ray powder diffraction
YBCO	Yittrium barium copper oxide
ZFC	Zero-field-cooled

Definitions of notation

A	: In chemical formulae, $A = $ K, Rb, Cs or Tl
X	: In chemical formulae, $X = $ Ca, Sr or Ba
T	: Temperature
λ	: Wavelength
J	: Exchange constant
Ω	: Solid angle
$\boldsymbol{a}$, $\boldsymbol{b}$, $\boldsymbol{c}$	: Real space unit cell parameters
$\boldsymbol{a}^*$, $\boldsymbol{b}^*$, $\boldsymbol{c}^*$	: Reciprocal lattice basis vectors
(H, K, L)	: Wavevector in reciprocal space, defined by $\boldsymbol{Q} = H\boldsymbol{a}^* + K\boldsymbol{b}^* + L\boldsymbol{c}^*$
T_{c}	: Superconducting transition temperature
T_{N}	: Antiferromagnetic ordering temperature
T_{s}	: Structural transition temperature
$T_{\mathrm{N,s}}$	: Structural and magnetic transition temperature
E_{r}	: Energy of the magnetic resonance
η	: Detector efficiency
Φ_0	: Incident flux of neutrons

$\boldsymbol{k}_{\mathrm{i}}$ ($\boldsymbol{k}_{\mathrm{f}}$)	: Initial (final) neutron wave vector
E_{i} (E_{f})	: Initial (final) neutron energy
E	: Energy transferred to a crystal in a neutron scattering process, $E = E_{\mathrm{i}} - E_{\mathrm{f}}$
$\boldsymbol{Q}$	: Scattering wavevector, $\boldsymbol{Q} = \boldsymbol{k}_{\mathrm{i}} - \boldsymbol{k}_{\mathrm{f}}$
2θ	: Scattering angle
$d^2\sigma/d\Omega dE_{\mathrm{f}}$	: Partial differential cross-section for neutron scattering
$f(\boldsymbol{Q})$	: Magnetic form factor
$S(\boldsymbol{Q}, E)$ or $\bar{S}(\boldsymbol{Q}, E)$	: Different forms of the magnetic scattering response function
χ	: Magnetic susceptibility
$\boldsymbol{M}$	: Magnetisation
$\boldsymbol{H}$	: Applied magnetic field
$\chi''(\boldsymbol{Q}, E)$	: Imaginary part of the generalised susceptibility
$\chi''(E)$	: Local susceptibility
$\Delta(\boldsymbol{Q}, E)$	: Superconducting gap function
$\delta(x)$	: Dirac delta function as a function of x
$\hbar$	: Reduced Planck constant, $\quad \hbar = 1.055 \times 10^{-34}\,\mathrm{J\,s}$
μ_0	: Permeability of free space, $\quad \mu_0 = 4\pi \times 10^{-7}\,\mathrm{H\,m^{-1}}$
m_{e}	: Electron mass, $\quad m_{\mathrm{e}} = 9.109 \times 10^{-31}\,\mathrm{kg}$
$-e$	: Charge on an electron, $\quad e = 1.602 \times 10^{-19}\,\mathrm{C}$
r_0	: Classical electron radius, $\quad r_0 = \mu_0 e^2/(4\pi m_{\mathrm{e}}) = 2.818 \times 10^{-15}\,\mathrm{m}$
m_{n}	: Neutron mass, $\quad m_{\mathrm{n}} = 1.675 \times 10^{-27}\,\mathrm{kg}$
m_{p}	: Proton mass, $\quad m_{\mathrm{p}} = 1.673 \times 10^{-27}\,\mathrm{kg}$
μ_{N}	: Nuclear magneton, $\quad \mu_{\mathrm{N}} = e\hbar/(2m_{\mathrm{p}}) = 5.051 \times 10^{-27}\,\mathrm{A\,m^2}$
μ_{B}	: Bohr magneton, $\quad \mu_{\mathrm{B}} = e\hbar/(2m_{\mathrm{e}}) = 9.274 \times 10^{-24}\,\mathrm{A\,m^2}$
$\boldsymbol{\mu}_{\mathrm{n}}$	: Magnetic moment of neutron, $\quad \boldsymbol{\mu}_{\mathrm{n}} = -1.913\mu_{\mathrm{N}} = 9.663 \times 10^{-27}\,\mathrm{A\,m^2}$
k_{B}	: Boltzmann constant, $\quad k_{\mathrm{B}} = 1.381 \times 10^{-23}\,\mathrm{J\,K^{-1}}$

Introduction

Contents

1.1 Superconductivity

Strongly correlated electron systems have motivated condensed matter physics research for decades, as it has long been clear that a non-interacting system of electrons cannot explain the properties of many materials. Models using non-interacting electrons have some successful applications, which are beautiful for their simplicity — a simple metal can be thought of as a sea of nearly-free electrons, whereas a simple insulator is described by tightly-bound electrons that do not move from their atomic site. Strongly correlated systems lie between these paradigms, and the electrons are able to interact with one another. Understanding the types of interactions and their relative strengths is a key motivating factor in condensed matter physics research. It is electronic correlations that lead to the discovery of collective phenomena and a range of interesting electronic and magnetic properties of materials. A prototypical example of collective effects is superconductivity. In superconductors the balance of interactions leads to attraction between pairs of electrons, at odds with the naive expectation that electrons should always repel. It is the desire to understand the novel state in superconducting materials that drives the work in this thesis.

The phenomenon of superconductivity was discovered over 100 years ago by Heike Kamerlingh Onnes [1]. In 1911 he made the unexpected discovery that below a finite critical temperature, T_c, of $4.2\,\mathrm{K}$ the electrical resistance of mercury falls to zero. In 1933 another property of superconductors was discovered, the Meissner effect, that is now considered a defining feature of superconductors.[1] Meissner and Ochsenfeld [2] found that a superconductor in an applied field will exclude the magnetic flux from its interior,[2] i.e. it becomes a perfect diamagnet. Although the discovery of superconductivity was made in 1911, it took over 50 years for a complete understanding of the underlying microscopic mechanism to be achieved. In 1957, Bardeen, Cooper and Schrieffer published a theory of superconductivity in which electrons form 'Cooper pairs' through interactions of electrons and phonons [3]. The electron pairs condense with their spins anti-aligned (i.e. in a singlet state) and this creates an energy gap between the ground state and the lowest quasiparticle excitation state. BCS theory explains why these pairs can travel through the material without scattering. This description, known as BCS theory, was a triumph in the field as it explained all of the superconductors known at that time. Unfortunately, however, BCS theory puts a limit on the maximum T_c of $\sim$30–40 K.

In 1979 the first unconventional superconductor, i.e. one that is not described by BCS theory, $CeCu_2Si_2$ was reported, but with a T_c of only $0.5\,\mathrm{K}$ [4]. It is believed that superconductivity in most unconventional materials is still caused by the formation of electron pairs, but the electron–phonon interaction is not strong enough to mediate this pairing as described in BCS theory. Unconventional superconductivity is an exciting area for research because there is no theoretical limit on T_c. The most important breakthrough in superconductivity, and arguably condensed matter physics, since the publication of BCS theory was the discovery of high-T_c superconductivity in a layered

---

[1]So as to distinguish them from perfect conductors.
[2]Below a critical value of applied field, H_c.
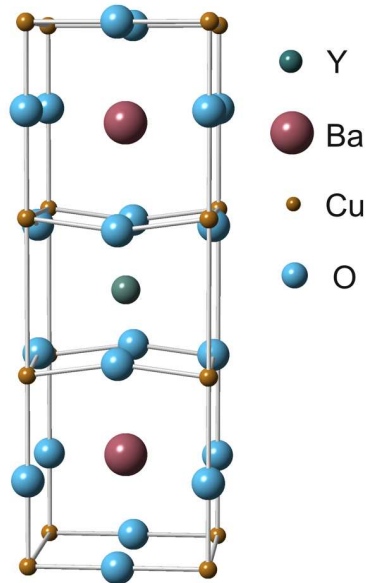
Figure 1.1: Structure of YBCO. One unit cell demonstrating the crystal structure of YBCO for the stoichiometric undoped material.

copper-oxide compound in 1986 [5]. These unconventional superconductors provide a useful context for the materials subsequently discussed in this thesis.

1.2 Copper-oxide superconductors

The copper-oxide superconductors are composed of layers containing copper and oxygen which are separated by other elements. The structure of $YBa_2Cu_3O_{7-\delta}$ (YBCO) is shown in Fig. 1.1 as an example — the copper–oxygen layers are visible with yttrium and barium in between. This particular material became famous for being the first superconductor to show a T_c (93 K) above liquid nitrogen temperature (77 K) [6]. Generally speaking, the undoped parent compounds of cuprate superconductors are described as Mott insulators,[3] in which strong local-coulomb interactions cause the material to be insulating instead of metallic. Within this Mott-insulator state, anti-ferromagnetic (AFM) ordering of the copper ions within the copper–oxygen planes is found (depicted in Fig. 1.2(b)).

The phase diagram of a cuprate superconductor is illustrated in Fig. 1.2(a); it shows how the properties of such materials evolve with both temperature and chemical doping. The AFM ordering (Fig. 1.2(b)) is only present in a narrow region of the phase diagram and is quickly suppressed by hole doping. It is clear that the superconductivity only emerges after the static AFM order has been suppressed. Strong AFM fluctuations, however, are still expected in regions of the phase diagram close to magnetic

---

[3]More formally the cuprates are better described as charge-transfer band insulators, but they are commonly referred to as Mott insulators in the literature. For a discussion and explanation of the difference see the review by Armitage *et al.* [7].
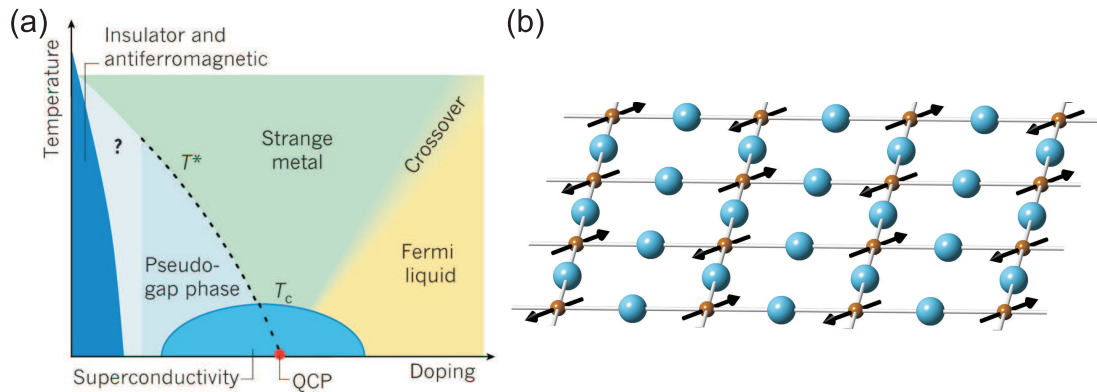
Figure 1.2: Generalised cuprates' phase diagram and magnetic order. (a) The generalised phase diagram of the cuprate superconductors, showing temperature against hole doping. Reprinted by permission from Macmillan Publishers Ltd: *Nature* **468**, 184–185, copyright (2010) [8]. (b) Simple representation of the AFM order in a CuO$_2$ layer in a cuprate material. Arrows represent the spin on a cooper ion. Adapted from Ref. [9].

order. This suggests that proximity to the magnetic phase might be essential to the superconductivity in the cuprates [9].

Magnetic and charge ordered phases, their associated dynamics, and their relationship with superconductivity in the cuprates is a diverse and complicated topic on which many reviews have been written, for example Refs. [10–12]. However, one important piece of evidence linking the magnetism in cuprates to superconductivity was the discovery of the *neutron scattering spin resonance* or *magnetic resonance* in superconducting YBCO [13], which is highly relevant to the work presented in this thesis.

The magnetic resonance is a feature in the INS response of a material. It is a localised enhancement in the intensity of magnetic fluctuations observed below T_c. The signal is localised at a particular energy transfer, E, and momentum transfer, $\boldsymbol{Q}$. In the cuprates, the wavevector of the resonance is usually $\boldsymbol{Q}_{\mathrm{AFM}}$, the wavevector associated with the AFM ordering of the parent phase (Fig. 1.2(b)), but the resonance is observed in samples that host superconductivity and no magnetic order.

This important observation, discussed further in § 2.4–§ 2.6, was subsequently reproduced in other cuprate materials as well as the heavy fermion superconductors, suggesting a possible commonality to unconventional superconductors [9]. This link between magnetism and T_c suggests that magnetic fluctuations could be involved in the superconducting pairing mechanism. Despite this, a description of the mechanism still evades the condensed matter physics community and remains a topic of intense research.

1.3   Iron-based superconductors

In 2008, shortly before I began the work discussed in this thesis, the field of superconductivity was opened up to a new area for the investigation of unconventional superconductivity and magnetism. A T_c of 26 K was discovered in LaFeAsO$_{1-x}$F$_x$ by Kamihara

et al. [14]; the material was immediately recognised as falling into a new class of unconventional superconductor. Many iron-pnictide and iron-chalcogenide compounds, which are more widely discussed in Chapter 2, were soon found to show superconductivity up to a maximum T_c of 56 K [15]. These T_cs cannot be explained by a phonon-mediated electron-pairing interaction. The iron-based systems were soon shown to have parent phases that magnetically order antiferromagnetically in a spin density wave (SDW) state [16].

These materials present a novel playground for investigating the magnetic interactions that may be the cause of the superconducting pairing process. The presence of iron immediately hints that strong magnetic correlations could be dominant in the materials, so the field of research was quickly directed to investigating magnetic order and dynamics. This thesis adds to the body of evidence indicating the importance of magnetic fluctuations in iron-based superconductors, which must ultimately be accounted for in a theory of the systems.

A description of the general properties of the iron-based superconductors and the prevailing theoretical model of their magnetic response is given in Chapter 2, as a setting to the work in this thesis. Chapter 3 gives the necessary background on the experimental techniques used. The remaining chapters predominantly concern the results of INS experiments to measure magnetic dynamics in a range of iron-based superconductors. The first of these chapters, Chapter 4, discusses an investigation of the non-superconducting parent-compound $SrFe_2As_2$, showing the form of the magnetic fluctuations that are a precursor to the superconducting phase. Chapters 5–8 then describe experiments that searched for magnetic responses linked to the superconducting state in a variety of materials. Conclusions and outlook from the work presented in this thesis are given in Chapter 9.

Iron-based superconductors

Contents

Figure 2.1: Structures of LaFeAsO, BaFe$_2$As$_2$ and FeSe. Crystallographic unit cells of the undoped materials are shown, for tetragonal ($T > T_s$) structures. The solid lines mark one unit cell for each material.

2.1 Introduction

Research on the iron-based superconductors began in 2008 when bulk superconductivity at $T_c = 26$ K was discovered in LaFeAsO$_{1-x}$F$_x$ [14]. Hundreds of papers were published on the topic in the same year. It is worth noting that superconductivity in this family had actually been discovered by the same group of researchers in isostructural LaFePO, which I discuss in Chapter 6, two years earlier; because of the low T_c in this material, $T_c \approx 4$ K, the significance of this finding was not recognised. The relatively high T_c of LaFeAsO$_{1-x}$F$_x$ was a promising indication of unconventional superconductivity and the potential for higher T_cs in similar materials. Many more superconducting systems were soon discovered, all containing iron coordinated with As, P, Se or Te in layers. It is the unpaired electrons in iron that appear to be responsible for both superconductivity and magnetism [15]. The current maximum T_c of $\sim$56 K was found in Gd$_{1-x}$Th$_x$FeAsO [17], although recently FeSe single-layer films have shown $T_c \sim 53$ K [18], with indications that T_cs as high as 65 K might be possible [19].

2.2 Structure

The common structural form of iron-based superconductors consists of layers containing Fe with one of As, P, Se or Te, nominally in a 1:1 ratio, in a tetrahedral arrangement. These layers are usually separated by other ions or collections of atoms called *blocking layers*. As the iron is found in separated layers, the systems can usually be considered quasi-two-dimensional, with minimal electronic coupling along the c-axis. Some important examples of this structural form are illustrated in Fig. 2.1, which shows the parent phases of LaFeAsO, $BaFe_2As_2$ and FeSe systems, all of which have tetragonal crystal symmetry at room temperature. The iron in these systems is divalent with electronic configuration $3d^6$. In the cases of LaFeAsO and $BaFe_2As_2$, the iron layers are separated by blocking layers. These two parent compounds are not superconducting themselves under ambient conditions, but require chemical doping or application of pressure to induce superconductivity [14, 20]. LaFeAsO and $BaFe_2As_2$ undergo small structural distortions from the tetragonal structures shown in Fig. 2.1, becoming orthorhombic below $T_s = 155\,\mathrm{K}$ [21], and $T_s = 140\,\mathrm{K}$ [22], respectively. The structural distortion is suppressed as these materials are chemically doped towards their maximum T_cs (see Fig. 2.3).

Many systems require doping in order to reach a superconducting state and/or their maximum possible T_c. However, this can often be achieved by isovalent doping, suggesting that the tuning of structural properties is important. The composition of the blocking layer affects both the Fe–As–Fe tetrahedral angle and the length of the c-axis, and these properties are thought to tune the superconductivity [15]. The highest T_cs are usually found only when the Fe–As–Fe angle is closest to the ideal tetrahedral angle of 109.47° [23]; the length of the c-axis is thought to affect the two-dimensionality of the systems and therefore the Fermi-surface properties that are key to superconductivity, as discussed in § 2.5 and § 2.6.

2.3 Magnetism

Magnetism, related to the presence of divalent Fe, is thought to be extremely important to superconductivity in these systems. Magnetic order is found in many systems below some transition temperature, T_N [24, 25]. For example in LaFeAsO and $BaFe_2As_2$ (among others) an ordered SDW state is found in the orthorhombic phase, which is illustrated in Fig. 2.2. The iron layer in the a–b plane of one of these systems is shown, with AFM alignment of iron spins along the orthorhombic a-axis and ferromagnetic (FM) alignment along the b-axis. The various unit cells used to describe these systems are shown. Unless otherwise specified, I will use the notation of the one-Fe (also known as square-lattice or unfolded) unit cell throughout this thesis, as it was shown by Park *et al.* [26] that the INS signal is described by the symmetry of this cell. The in-plane wavevectors associated with SDW order are $(0.5, 0)$ and equivalent positions, where wavevectors are expressed in reciprocal lattice units (r.l.u.) of the one-Fe unit cell.

Understanding the SDW state (Fig. 2.2) is thought to be of great importance in these systems because the suppression of the SDW order correlates with the emergence
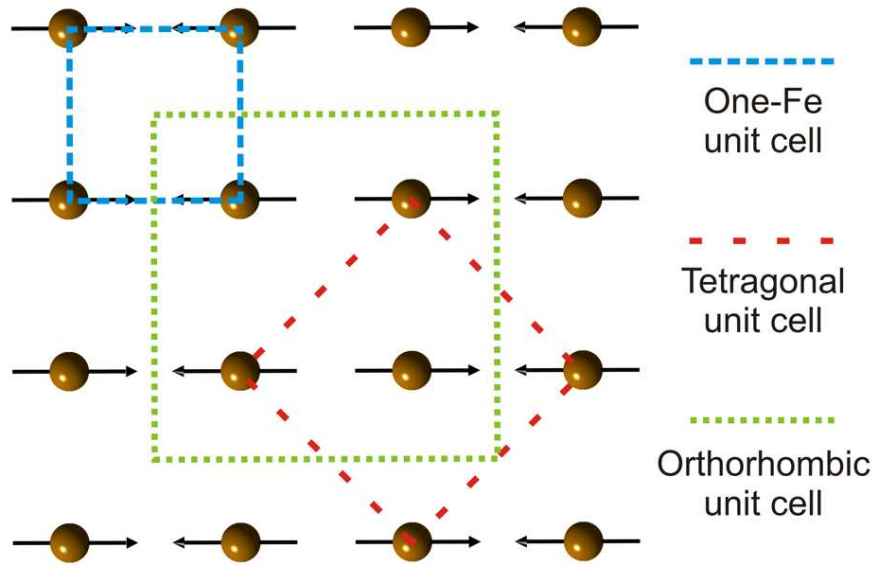
Figure 2.2: Typical iron layer. Single layer of iron in the a–b plane, with SDW ordering shown (other atoms have been omitted for clarity). The arrows represent the direction of spin on the irons. The in-plane part of the various units cells that are used to described these systems are shown; for the one-Fe and tetragonal unit cells $a=b$, for the orthorhombic unit cell the a-axis lies along the line of the Fe spins and is elongated with respect to the b-axis (not illustrated).

of superconductivity [25, 27, 28]. This is illustrated in the phase diagram of $BaFe_2As_2$ in Fig. 2.3. The maximum T_cs on either side of the phase diagram are achieved when the SDW has been suppressed, although there are small regions where the SDW and superconductivity coexist on a microscopic scale [27, 29–31]. This sort of magnetic order could result from ordering of local moments on the iron sites, or be due to itinerant electron ordering. The strength of correlations in the iron-based superconductors is the subject of current research, as will be discussed in Chapter 4.

The striking similarity to the cuprates' phase diagram can be seen by comparing Fig. 2.3 with Fig. 1.2(a) — in both cases the superconducting dome appears in close proximity to the suppression of an antiferromagnetically ordered state. However, the details of the magnetism in these systems are actually quite different. The superconductivity in the cuprates emerges from a Mott insulator state, whereas the iron-based superconductors are generally thought to be semi-metals, with a paramagnetic phase as a precursor to magnetism and superconductivity. In both cases, however, where there is suppression of the magnetic order, strong magnetic fluctuations are expected, as was discussed in the case of the cuprates in § 1.2.

2.3.1 Localised and itinerant magnetic fluctuations

As mentioned above, the magnetic order depicted in Fig. 2.2 could originate from either localised or itinerant magnetism. In this section, I will briefly discuss how both of these
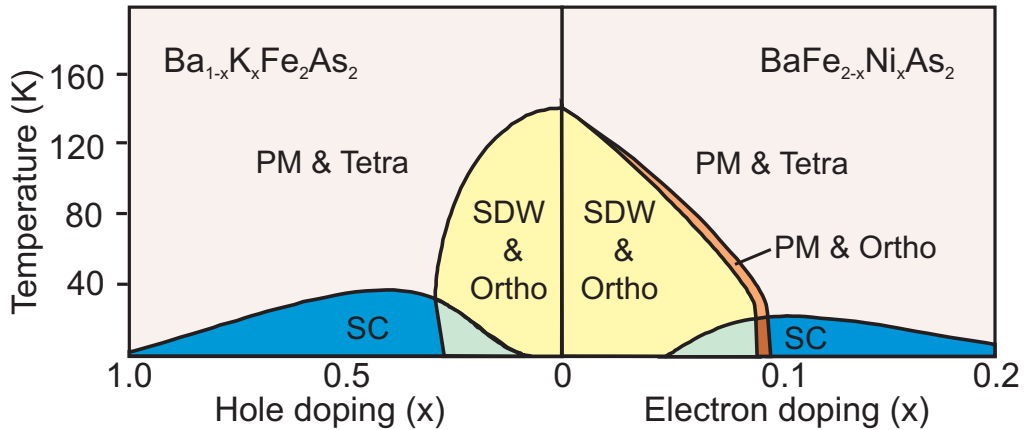
Figure 2.3: Phase diagram of an iron-based superconductor. Phase diagram of the material $BaFe_2As_2$, considered an archetypal system, for both hole and electron dopings. PM stands for paramagnetic, SC stands for superconducting, and tetra and ortho refer to the structural symmetry of the system. Adapted from Ref. [25].

result in spin fluctuations that can be measured by INS. For detailed discussions of exchange interactions and spin dynamics see Refs. [32, 33]. I discuss INS measurements in Chapter 3.

Localised magnetism occurs via interactions between electrons that are confined to particular magnetic sites. For example, even though the electrons are not free to move throughout the crystal, the kinetic energy of a system can be reduced if electrons on adjacent ions are allowed to move between those ions. This is only possible if the exchange symmetry of the electrons is preserved. It is therefore energetically favourable for the electrons to adopt a spin state that allows them to visit an adjacent site while obeying the Pauli exclusion principle. This can lead to long-range magnetic order. Magnetic excitations will always exist in systems in which magnetic exchange interactions are present. The magnetic excitations in magnetically-ordered systems are called spin waves, and they are quantised as magnons, in analogy with phonons in an ordered solid. The behaviour of magnons is characterised by a dispersion relation. In localised magnets spin waves have a sharp dispersion in (Q, E)-space, as illustrated in Fig. 2.4(a).

Itinerant electron magnetism occurs in systems in which the electrons are free to move throughout the crystal. The electrons are not bound to the magnetic ions; they are not, however, free from interactions. The electrons interact both with the periodic potential of the ions and through mutual Coulomb interactions. The effects of exchange, ultimately caused by Coulomb interactions, can cause ordering to occur by splitting of the spin-up and spin-down electronic bands. This means that magnetic excitations will occur in itinerant systems including spin-wave-type collective excitations. In itinerant systems, however, electron–hole excitations across the spin-split bands will also occur [34]. This creates a continuum of excitations in a large region of (Q, E)-space, an example of which is illustrated by the grey shaded region in Fig. 2.4(b). This so called Stoner continuum introduces a decay path for the collective excitations, there-
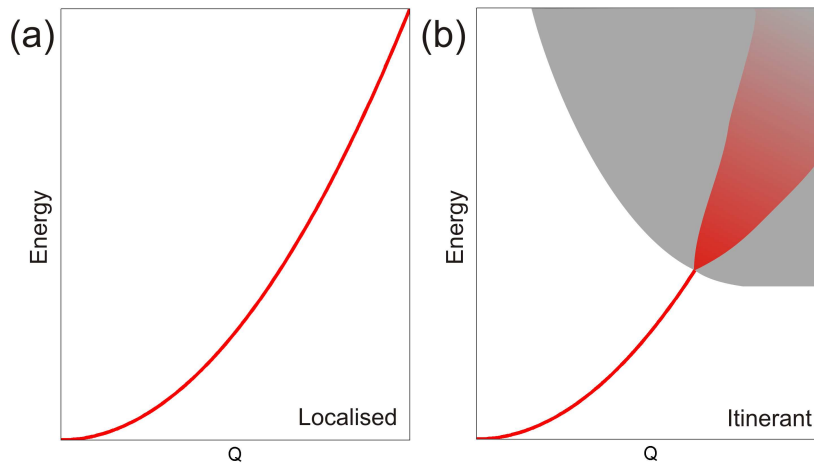
Figure 2.4: Schematic magnetic excitation spectra. Representation of a possible magnetic excitation spectrum in an INS experiment for (a) localised and (b) itinerant magnetic systems. The red line represents the sharp scattering intensity expected from spin waves. The light grey shaded region in (b) indicates the electron–hole excitation continuum. The red shaded region indicates the broadening of the collective excitations due to decay into the single electron excitation channel.

fore decreasing their lifetime and causing significant broadening of the dispersion in the continuum region. Spin-wave-type excitations merging into a Stoner continuum were first observed ferromagnetic systems MnSi [35], Ni [36] and Fe [37]. In Fe, for example, the intensity of the spin-wave scattering was found to drop by an order of magnitude in the Stoner excitation continuum region. The broadening of collective excitations in an itinerant system is illustrated schematically by the red shaded region in Fig. 2.4(b).

As the magnetic interactions of neutrons are well understood (Chapter 3), the excitation spectrum expected from either itinerant or localised magnetic systems can often be calculated. This allows direct comparison between theory and experiment, and has been used to shed light on the nature of the magnetic state that exists in the iron-based superconductors, as will be discussed in Chapter 4.

2.4 Observation of the magnetic resonance

The presence of magnetism in the phase diagrams of the iron-based superconductors immediately leads to the question: is there a signal in the magnetic excitation spectrum similar to the magnetic resonance found in the cuprates (see § 1.2)? Initial investigations of the magnetic dynamics led to observations of two-dimensional (2D), steeply-dispersing magnetic fluctuations. These emerge from the point in reciprocal space associated with the SDW order — $\boldsymbol{Q}_{\mathrm{SDW}} = (0.5, 0)$ — found in parent-phases $BaFe_2As_2$ [38] and $LaFeAsO$ [39]. At about the same time, Christianson *et al.* [40] used INS to probe the magnetic fluctuations in a $T_{\mathrm{c}} = 38\,\mathrm{K}$ superconductor, polycrystalline $Ba_{0.6}K_{0.4}Fe_2As_2$. A signal characteristic of a magnetic resonance was found, as shown in Fig. 2.5.
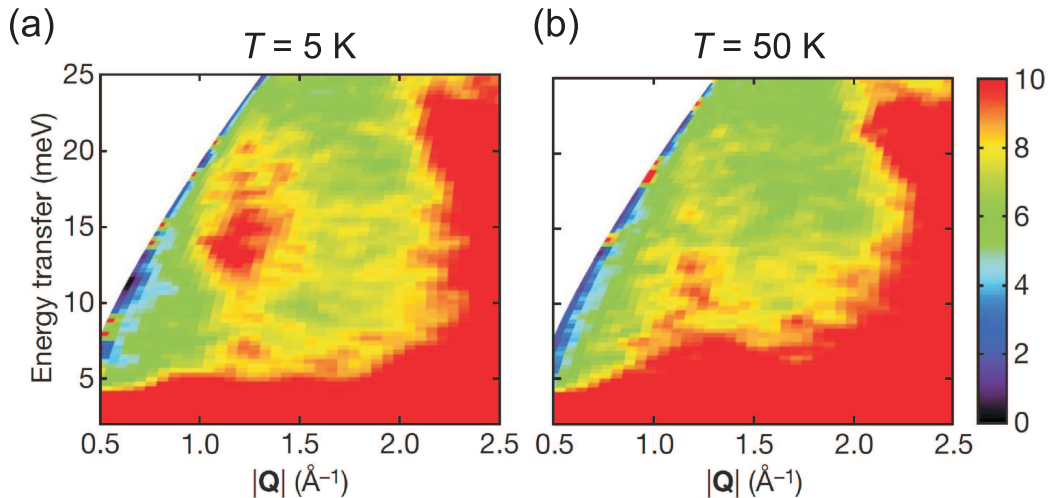
Figure 2.5: Observation of the magnetic resonance in Ba$_{0.6}$K$_{0.4}$Fe$_2$As$_2$. INS measurement of the excitation spectra from polycrystalline Ba$_{0.6}$K$_{0.4}$Fe$_2$As$_2$ from both (a) below T_c and (b) above T_c. The colour scale represents intensity measured in units of mb sr^{-1} meV^{-1} mol^{-1}. Reprinted by permission from Macmillan Publishers Ltd: *Nature* **456**, 930–932, copyright (2008) [40].

In Fig. 2.5 it is clear that in a localised region of (Q, E)-space there is enhanced scattering at 5 K compared with 50 K. The intensity of the signal increases with decreasing temperature below T_c, approximately following an order parameter type curve of the form $A \left(1 - \left(\frac{T}{T_c} \right)^2 \right)^{1/2} + B$. The intensity peaks in wavevector at $Q \approx 1.15\,\text{Å}^{-1}$ and in energy at $E \approx 14\,\text{meV}$. These values are important for comparison to both theory and to other empirical observations. The powder-averaged position $Q \approx 1.15\,\text{Å}^{-1}$ is equivalent to $Q_{\text{SDW}} = |(0.5, 0)|$, the magnitude of the wavevector associated with SDW order, even though this material itself is not magnetically ordered. The peak energy of the resonance, E_r, gives the relationship $E_r = 4.3\,k_B T_c$, which is close to the empirical relation found in the cuprate superconductors of $E_r \approx 5\,k_B T_c$.[1] These results are replicated across many iron-based superconductors, and measurements of single crystals have confirmed that the signal does indeed result from scattering from the position $\boldsymbol{Q}_{\text{SDW}} = (0.5, 0)$ [43–45]. Even superconducting FeSe$_{1-x}$Te$_x$ shows the magnetic resonance in its INS spectrum at $\boldsymbol{Q}_{\text{SDW}}$, despite the fact that the magnetic order observed in the parent-phase FeTe is not SDW order [46]. In all cases the intensity of the magnetic scattering at $\boldsymbol{Q}_{\text{SDW}}$ is enhanced as the material is cooled below T_c.

The ubiquity of the magnetic resonance across the iron-based superconductors (as well as cuprates and heavy fermion superconductors) is often cited as evidence that the

---

[1]A more complete analysis considers the scaling relation between E_r and the gap energy Δ. The relationship $E_r/2\Delta = 0.64$ holds across many unconventional superconductors, including the heavy fermion compounds [41], not just the cuprates and iron-based superconductors [42]. However, the relationship $E_r \approx 5\,k_B T_c$ appears to hold true in the iron-based systems [15, 24] and is easily accessible in the experiments presented in this thesis, so I will discuss this relationship throughout.
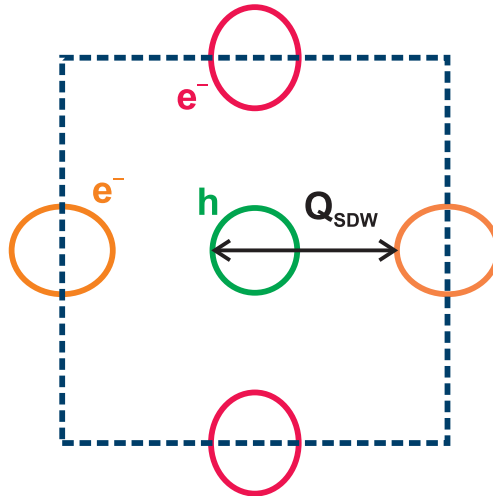
Figure 2.6: Simplified Fermi surface of an iron-based superconductor. Schematic representation of the generalised in-plane Fermi surface proposed to capture the essential physics of the iron-based superconductors. Electron and hole pockets are labelled as e^- and h respectively. The blue dashed square marks the one-Fe-cell first-BZ boundary.

magnetic fluctuations are linked to the superconducting pairing mechanism [9, 15, 24, 25, 47–49]. The key features from empirical observations — $\boldsymbol{Q} = \boldsymbol{Q}_{\mathrm{SDW}} = (0.5, 0)$ and $E_{\mathrm{r}} \approx 5k_{\mathrm{B}}T_{\mathrm{c}}$ — give important insights into this relationship, as they can be reproduced by certain theoretical models.

2.5 Theoretical treatment of the resonance

As discussed above, an SDW ordered state could be due to either localised or itinerant electronic interactions, both resulting in magnetic fluctuations. The most common description of the iron-based systems, however, is that itinerant electrons are responsible for both superconductivity and the magnetic resonance (Chapter 4 discusses attempts at local-moment modelling of the magnetism). They are thought to be semi-metallic systems, with the density of states at the Fermi energy dominated by the iron $3d$ orbitals [50]. A band theory description is therefore required to encompass the behaviour of the $3d$ electrons, and the structure of the Fermi surface is crucial to understanding the materials.

The structure of the Fermi surface can be measured by angle-resolved photoemission spectroscopy (ARPES) or quantum oscillations experiments on single crystal samples [51–55]. These types of measurement led to the determination of the Fermi surface in materials of which single crystals were available soon after the discovery of iron-based superconductors, such as $BaFe_2As_2$ [56, 57]. They revealed hole pockets at the centre of the Brillouin zone (BZ), and electron pockets at positions $(0.5, 0)$ and equivalent, as shown schematically in Fig. 2.6. Because of the layered structure of these systems the Fermi surface is quasi-2D; therefore these hole and electron pockets can be considered as cylinders with their axis along the $\boldsymbol{c}^*$ direction, i.e. out of the plane of Fig. 2.6.

Here I outline the basic features of a theoretical description based on this generalised Fermi surface [47, 58]. The hole and electron pockets are *quasi-nested*. The nesting condition holds when two sections of a Fermi surface are parallel and separated by a wavevector $\boldsymbol{Q}_{nest}$, such that there is a high density of states for scattering at $\boldsymbol{Q}_{nest}$. This can drive the system to a magnetically ordered state. In the case of $\mathrm{BaFe_2As_2}$, the hole and electron pockets separated by $\boldsymbol{Q}_{\mathrm{SDW}}$ (see Fig. 2.6) are not exactly parallel, hence the term quasi-nested, but there is still a high density of states for scattering at $\boldsymbol{Q}_{\mathrm{SDW}}$ and this can drive the formation of the SDW state [50].

To relate the Fermi surface structure to the magnetic resonance a treatment based on results known from BCS theory of conventional superconductors is used [9, 59–61]. Although a full theoretical treatment of the resonance and its behaviour is more complicated, within an itinerant model the occurrence of the resonance can be explained by an enhancement in the band electron susceptibility, $\chi(\boldsymbol{Q}, E)$, caused by the BCS coherence factor, C. This coherence factor describes neutron spin-flip scattering (i.e. magnetic scattering), and states that the rate of spin flip scattering for a quasiparticle scattered between portions of the Fermi surface from $\boldsymbol{k}$ to $\boldsymbol{k} + \boldsymbol{Q}$ is determined by

$$C = \frac{1}{2}\left(1 - \frac{\Delta(\boldsymbol{k})\Delta(\boldsymbol{k} + \boldsymbol{Q})}{E(\boldsymbol{k})E(\boldsymbol{k} + \boldsymbol{Q})}\right), \tag{2.1}$$

where $\Delta(\boldsymbol{k})$ is the value of the superconducting gap at point $\boldsymbol{k}$ on the Fermi surface, and $E(\boldsymbol{k})$ is the quasiparticle energy, $E(\boldsymbol{k}) = \sqrt{\varepsilon_k^2 + \Delta^2(\boldsymbol{k})}$. The ε_k are the band energies measured relative to the Fermi energy. Therefore, at threshold for quasiparticle scattering, the value of C is determined by the sign of the gap function, $\mathrm{sgn}[\Delta(\boldsymbol{k})]$, in the following way

$$C \rightarrow \begin{cases} 0 & \text{for } \mathrm{sgn}[\Delta(\boldsymbol{k} + \boldsymbol{Q})] = +\mathrm{sgn}\,[\Delta(\boldsymbol{k})] \\ 1 & \text{for } \mathrm{sgn}[\Delta(\boldsymbol{k} + \boldsymbol{Q})] = -\mathrm{sgn}\,[\Delta(\boldsymbol{k})] \ . \end{cases} \tag{2.2}$$

Equation 2.2 determines under what conditions increased neutron scattering will be seen at momentum $\boldsymbol{Q}$ upon the formation of superconducting pairs, i.e. below T_c. The resonance occurs at a wavevector $\boldsymbol{Q}$ that (i) contributes significantly to the scattering, and (ii) links two sections of the Fermi surface on which the gap has opposite sign. In the case of iron-based superconductors the quasi-nesting at wavevector $\boldsymbol{Q}_{\mathrm{SDW}}$ means that condition (i) is met, therefore the observation of a magnetic resonance indicates that the gap should meet condition (ii) on the appropriate sections of the Fermi surface.

2.6 Proposed gap symmetries

As the iron-based systems are understood to be singlet superconductors [15, 49, 58, 62], i.e. the electrons pair with their spins aligned antiparallel, this limits the possible symmetries of the gap function. Figure 2.7 illustrates the gap functions that have been proposed to describe the superconducting states in the iron-based systems [58]. Comparing to Fig. 2.6 shows that the gap changes sign between the sections of Fermi
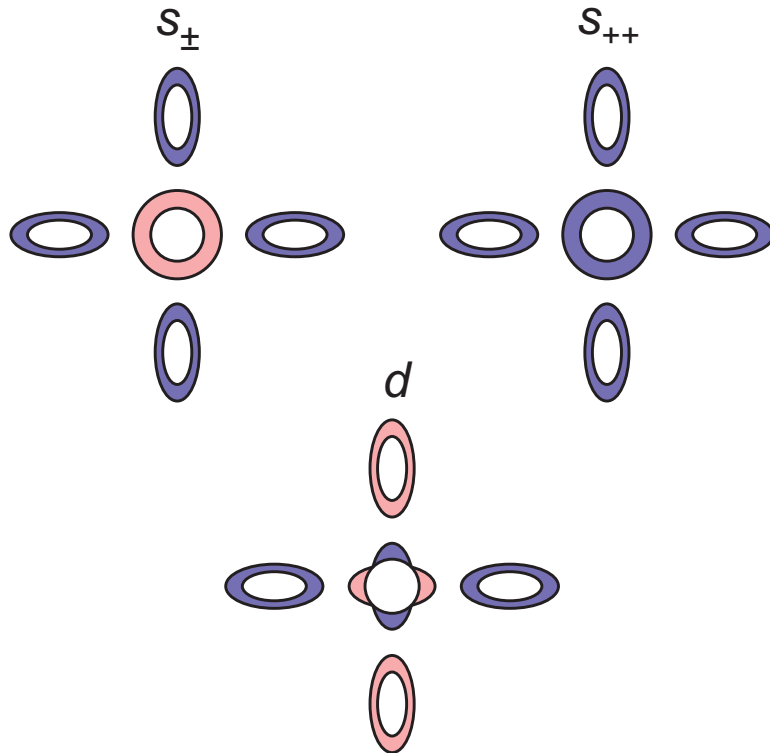
Figure 2.7: Proposed symmetries of the superconducting gap. Schematic representation of the in-plane component for various superconducting gap symmetries that have been proposed to describe the iron-based superconductors. The different colours represent opposite signs of the gap. Adapted from Ref. [58].

surface separated by $\boldsymbol{Q}_{\mathrm{SDW}}$ for $s_{\pm}$ and d-wave gap symmetries. Comparisons of theory to a variety of experiments led to the conclusion that the $s_{\pm}$ symmetry best describes these systems, unlike the cuprates which are described by the d-wave state [47, 63].[2] The observation of the magnetic resonance at $\boldsymbol{Q}_{\mathrm{SDW}}$ has been cited as confirming the $s_{\pm}$ pairing symmetry, in accordance with the coherence factor description as outlined above [40, 61, 62, 66].

Clearly the s_{++} state depicted in Fig. 2.7 cannot satisfy the condition in Eq. 2.2 for $C \to 1$. Many have therefore excluded this symmetry as a possibility. However, there are some suggestions that this state cannot be dismissed if an orbital (rather than spin) fluctuation model is used to describe the systems [67, 68]. The spatial symmetry of the gap function is the same as for the $s_{\pm}$ gap and therefore the difference cannot be determined by Fermi surface measurements such as ARPES [58]. There are some claims that the orbital s_{++} model could still lead to an enhancement in INS intensity at $\boldsymbol{Q}_{\mathrm{SDW}}$ below T_{c} [69, 70]. This uncertainty reflects the difficulty in modelling these

---

[2]The 3.4 K superconductor $\mathrm{KFe_2As_2}$ has actually been suggested to host a d-wave superconducting state. However, if a d-wave symmetry does exist, it can be understood in terms of the evolution of the Fermi surface with doping in the $\mathrm{Ba_{1-x}K_xFe_2As_2}$ series which causes the dominant pairing to evolve from an $s_{\pm}$ to d-wave state [64, 65]. The possible d-wave state in $\mathrm{KFe_2As_2}$ therefore does not detract from the discussions throughout this thesis.

itinerant d-electron systems where a multi-band approach is required for a complete theory [71]. Further discussion of the s_{++} model is beyond the scope of this thesis, as it should be noted that the literature on iron-based superconductors is overwhelmingly in support of an $s_{\pm}$ pairing symmetry for superconductivity in the archetypal families $BaFe_2As_2$, $LaFeAsO$ and $FeSe$.

2.7 Summary

Iron-based superconductors present a new opportunity for investigating the interplay between superconductivity and magnetism. The layered structures appear to promote superconductivity, and allow for quasi-2D models to capture the behaviour of the systems. Magnetism is found close to the superconducting state, suggesting the intimate link between superconductivity and magnetism that has been experimentally confirmed. Theories to describe the systems must consider the five d electron bands of the Fe ions. Although modelling and determining the leading instabilities in these multi-orbital systems is difficult, careful comparison to experimental results makes it possible to learn important details about the superconducting state.

It has been established that an $s_{\pm}$ gap symmetry seems to describe the superconductivity in the materials discussed in this chapter. The technique of INS made a significant contribution to the evidence in favour of the $s_{\pm}$ state by revealing the magnetic resonance feature in the excitation spectrum. The position, $\boldsymbol{Q} = \boldsymbol{Q}_{\mathrm{SDW}} = (0.5, 0)$, and energy scale, $E_{\mathrm{r}} \approx 5 k_{\mathrm{B}} T_{\mathrm{c}}$, of the resonance both provide valuable information about the superconducting state, and must be reproducible in any theory describing these systems. Thus there is a necessity to investigate the link between magnetic fluctuations and superconductivity further, and this thesis contributes to this field.

Experimental techniques

Contents

3.1 Solid-state synthesis

The powder samples I have investigated were made by solid-state-chemistry synthesis techniques either by myself, samples in Chapter 6, or others, Chapters 5 and 8. The basic principles of these techniques are described here. The single crystal, Chapters 4 and 7, and soft-chemical, Chapter 8, growth techniques used to produce samples will be mentioned in those chapters.

The synthesis technique I used to produce samples is called the *ceramic method* and is used to produce high-quality powders. It involves weighing out precise stoichiometric amounts of high-purity starting materials, then grinding them to a very fine powder with a pestle and mortar. Grinding ensures intimate mixing of the reagents as well as increased contact area, which increases the reaction rate. Often the powder is then pressed into a dense pellet to maximise surface contact between the grains. The powder or pellet must then be heated to very high temperatures (600–1500 °C) to overcome the kinetic barrier to the reaction before the final product forms.

Often the reactants are air sensitive even at room temperature, so the whole process must be carried out with the sample in an inert atmosphere. All manipulations reported here were carried out in a Glove Box Technology argon-filled glove box. This recirculates argon through a copper catalyst and molecular sieve bed to remove oxygen and water respectively, maintaining the glove box atmosphere with an O_2 concentration < 5 parts per million under normal working conditions.

The material has to be removed from the glove box in order to place it in a furnace; to maintain the inert atmosphere the sample is sealed inside an unreactive ampoule. This is achieved by placing the sample in an alumina crucible inside a silica glass tube that has been presealed at one end. The crucible is required because the silica could react with the sample material if they were in contact at high temperatures. The tube is temporarily sealed with a Young's tap and can then be taken out of the glove box. The tap is attached to a vacuum line and then the tube is sealed under vacuum by glassblowing. As some of the reagents I used are particularly moisture sensitive, I pretreated the silica tubes to remove any trapped moisture by heating them to 1000 °C for several hours under dynamic vacuum of 10^{-2} mbar.

In cases where volatile metals are used as starting materials, these have to be pre-reacted inside an inert metal reaction vessel. This is because these volatile metals, when heated, create a high pressure of corrosive vapour that could easily explode a silica vessel. In this case, the metal is prepared in a niobium tube that is sealed under an argon atmosphere by arc welding. Niobium does not react with the synthesis reagents, but would react with atmospheric oxygen at high temperatures. To avoid corrosion the niobium is sealed inside a silica ampoule as above, but without the need for pretreating the silica.

3.2 Characterisation measurements

After synthesis, the high-quality polycrystalline materials need to be checked for purity, composition and physical properties. The main characterisation methods used for

the work in this thesis were x-ray diffraction and magnetometry, so these are briefly described here.

3.2.1 X-ray diffraction

Diffraction is a well-known technique used to determine the structure of crystalline materials, which takes advantage of the coherent, constructive interference of radiation scattered by a sample. Interference causes a high intensity of elastic scattering at certain positions in reciprocal space. This is governed by Bragg's law:

$$n\lambda = 2d_{hkl}\sin\theta, \tag{3.1}$$

where λ is the wavelength of the radiation, n is an integer, θ is half the angle between the incident and outgoing radiation (as defined below by the scattering triangle in § 3.4.1 and Fig. 3.1) and d_{hkl} is the crystal lattice d-spacing that relates to the magnitude of the scattering vector, Q, by $d_{hkl} = 2\pi/Q$.

X-ray diffraction is commonly used for characterisation because x-rays can be easily produced in a laboratory. To perform x-ray powder diffraction (XRPD) measurements I used a PANalytical X'Pert Pro diffractometer, which is a high-resolution, high-intensity diffractometer that produces Cu $K_{\alpha 1}$ monochromatic radiation. It performs measurements by scanning the angle 2θ and measuring intensity. I used the Rietveld refinement package GSAS+EXPGUI [72, 73] to refine structural models to data. This method allows refinement of unit cell parameters, atomic positions, site occupancies, and relative fractions of any impurity phases present in the material.

3.2.2 Magnetometry

As discussed in § 1.1, the superconducting state is not defined by zero electrical resistance alone, but also by the perfect diamagnetic response of a superconductor in an applied magnetic field.[1] Measurement of this response is a good method for checking whether a sample is a superconductor and for finding T_c. Results from magnetometry are common because it is a bulk measurement that can easily be made in the laboratory down to ~ 2 K, and it avoids the need to connect electrical contacts to the sample.

Perfect diamagnetism is defined by a magnetic susceptibility, χ, of $\chi = -1$, where

$$\boldsymbol{M} = \chi\boldsymbol{H} \tag{3.2}$$

and $\boldsymbol{M}$ is the magnetisation of the sample in response to an applied field $\boldsymbol{H}$. χ is a dimensionless parameter in SI units, with a minimum of -1 corresponding to total exclusion of magnetic flux. $\boldsymbol{M}$ (or a quantity proportional to it) can be measured using a superconducting quantum interference device (SQUID) magnetometer with the sample in a chosen $\boldsymbol{H}$, therefore χ can be calculated. In principle, if 100% of the volume of the sample is superconducting it will give a response $\chi = -1$; if only 50%

---

[1] Below a critical value of applied field, above which the superconductor either enters the mixed state or superconductivity is completely destroyed.

of the sample is superconducting it will give a response $\chi = -0.5$, etc. The fraction of the sample that is superconducting is known as the *volume fraction*.

The SQUID measurements I report here were performed on a Quantum Design MPMS SQUID magnetometer, and were predominantly measurements of powder samples so only a powder-averaged M (not $\boldsymbol{M}$) was measured. In practice, the mass and density of the sample are required in order to work out M and χ. The mass is measured to a precision of $0.1\,\mathrm{mg}$ before performing measurements (on masses of typically $40\,\mathrm{mg}$). The density, however, is not well known, particularly for powders in which the packing density is unknown. Additionally, in a real set-up the measured response depends on sample geometry and demagnetisation effects, and surface screening effects. This means that the value of χ calculated is not actually a good measure of the superconducting volume fraction, and -1 is not a rigorous lower bound on the experimental value. For all of the results I present, I give the χ calculated directly from the measurement using the formula:

$$\chi = \frac{4\pi\rho\zeta}{Hm}, \tag{3.3}$$

where ρ is the density of a unit cell in $\mathrm{g\,cm^{-3}}$ as determined in GSAS, H is the magnitude of the applied field in units Oe,[2] m is the mass of the sample in g, and ζ is the moment of the sample measured by the SQUID in units emu. Despite the difficulty in determining the absolute magnitude of χ, the sign of χ can be correctly determined. Therefore, when χ is measured as a function of temperature in a superconductor, the sharp downturn in the curve to negative values allows T_c to be accurately determined. The shape of this curve can also provide clues as to whether bulk superconductivity has been achieved (see, for example, Fig. 5.3(b)).

3.3 Neutron scattering

Neutrons are an extremely useful probe for investigations in condensed matter physics, and in particular magnetic systems, for a variety of reasons. Firstly, interactions in the thermal range, i.e. $\sim 25\,\mathrm{meV} \equiv 290\,\mathrm{K}$, are typically of interest; the advantage of neutrons is that their de Broglie wavelength at this energy is $\lambda = 1.8\,\text{Å}$, comparable to interatomic distances. The wave-like nature of the neutron at the scale of interest means that interference effects occur between scattered neutrons. This is exploited to reveal information about a sample. Secondly, neutrons respond to both nuclear and magnetic interactions, allowing both structural and magnetic correlations in a material to be probed. These interactions between neutron and sample are well understood, so the results of neutron scattering experiments can be modelled and directly compared to theory — this is in contrast to x-ray scattering where modelling of magnetic scattering is much more difficult. The neutron interacts with a nucleus via the strong force, which is powerful but only acts over a very short length scale. Magnetic scattering is due to the neutron's spin interacting with unpaired electrons in an atom's outer shells via electromagnetism. This is a much weaker force but it acts over a larger length

---

[2] $1\,\mathrm{Oe} = 10^3/4\pi\,\mathrm{A\,m^{-1}}$.

scale. This means that in both cases the overall scattering cross-section for neutrons is relatively small, which leads to the third major advantage of neutrons: they are a bulk probe. As they are only weakly scattered, neutrons can propagate through an entire sample and scatter from all parts of it. This means that, unlike many techniques, neutron scattering does not just probe the surface of a sample.

In contrast to § 3.2.1, where I discussed the use of x-ray scattering to determine the static structure of a material, this thesis is predominantly concerned with the use of neutron scattering to measure the magnetic dynamics. Just as structural fluctuations (phonons) can occur in a system, magnetic fluctuations are present in systems with magnetic atoms, as discussed in § 2.3.1. As the neutron interacts magnetically, it can exchange energy and momentum with magnetic fluctuations. Thus, by determining the energy, momentum, and spin of neutrons before and after scattering, the properties of the fluctuations can be inferred.

In the following section, I discuss the basic principles required for understanding the INS results presented in this thesis. The results all concern coherent, inelastic, magnetic neutron scattering using an unpolarised neutron beam,[3] so the discussion will focus on this subset of neutron scattering techniques. Full theoretical treatments can be found in textbooks [74–76], and Ref. [77] gives a clear account of neutron scattering instrumentation, so in § 3.4 and § 3.5 I simply introduce the main concepts that are important for the work presented in this thesis.

3.4 Neutron scattering theory

3.4.1 Basic scattering concepts

I start by considering a neutron with an initial wavevector $\boldsymbol{k}_i$ and energy E_i. It is incident on the sample and is scattered through an angle 2θ to a final state with wavevector $\boldsymbol{k}_f$ and energy E_f. In this process the momentum, energy and spin of the neutron can change. Energy and momentum are conserved in the scattering process, and the momentum and energy transferred to the sample, $\hbar\boldsymbol{Q}$ and E respectively, are defined by:

$$\boldsymbol{Q} = \boldsymbol{k}_i - \boldsymbol{k}_f \tag{3.4}$$

$$E = E_i - E_f. \tag{3.5}$$

$\boldsymbol{Q}$ is known as the *scattering vector*. This process is shown schematically in Fig. 3.1, where $\boldsymbol{k}_i$, $\boldsymbol{k}_f$ and $\boldsymbol{Q}$ form the *scattering triangle*.

For an inelastic scattering process k_i is not equal to k_f, and the change in energy of the neutron can be expressed in terms of k_i and k_f as:

$$E = \frac{\hbar^2}{2m_n} \left(k_i{}^2 - k_f{}^2 \right), \tag{3.6}$$

---

[3]As the neutron has a moment, it is possible to spin polarise a neutron beam, which allows more information about the magnetic scattering to be determined, at the expense of neutron intensity. For a detailed discussion of the topic see Ref. [74].
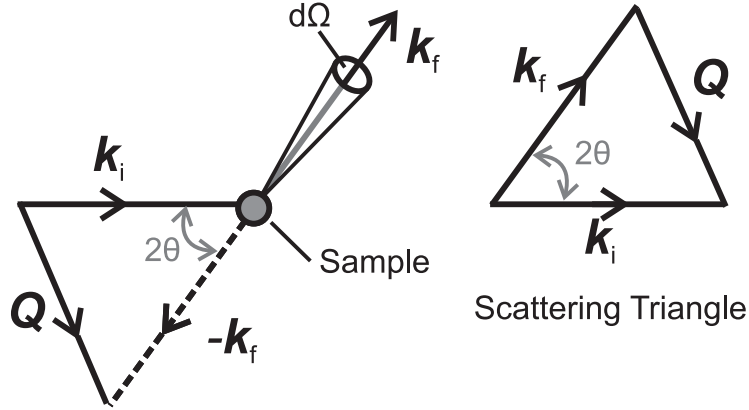
Figure 3.1: Scattering geometry. Schematic representation of the geometry of a neutron scattering experiment. $d\Omega$ is the unit of solid angle subtended by the detector.

where m_n is the mass of the neutron. With reference to Fig. 3.1, Eqs. 3.4 and 3.6 allow the wavevector and energy for a scattering event to be calculated.

3.4.2 Neutron scattering cross-section

In a neutron scattering experiment the neutron will only be detected if it reaches the detector, which subtends a solid angle $\Delta\Omega$, and has an energy within an acceptable range ΔE_f of the nominal E_f. So if the detector has an efficiency η and the incident flux of neutrons is Φ_0, then the measured count rate during a neutron scattering experiment is

$$\eta\Phi_0 \frac{d^2\sigma}{d\Omega dE_\mathrm{f}} \Delta\Omega\Delta E_\mathrm{f}, \tag{3.7}$$

where $d^2\sigma/d\Omega dE_\mathrm{f}$ is the *partial differential cross-section*. $d^2\sigma/d\Omega dE_\mathrm{f}$ is the property that it is actually desirable to measure, so for the rest of this treatment I will assume the other terms in Eq. 3.7 are known (see § 3.5.5), and focus solely on the partial differential cross-section.

The partial differential cross-section is defined as

$$\frac{d^2\sigma}{d\Omega dE_\mathrm{f}} = \frac{\left(\begin{array}{c} \text{number of neutrons scattered per second} \\ \text{into the solid angle } d\Omega \text{ in the direction } \theta, \phi \\ \text{with final energy between } E_\mathrm{f} \text{ and } E_\mathrm{f} + dE_\mathrm{f} \end{array}\right)}{\Phi_0 d\Omega dE_\mathrm{f}}. \tag{3.8}$$

Quantum mechanics can be used to obtain an expression for the cross-section from first principles, by considering the probability of the neutron–sample system making a transition from an initial state λ_i to a final state λ_f. The neutron is a weak probe, so its interaction potential can be treated as a perturbation on the system and therefore the Born approximation can be used to calculate the transition probability. This means that both incident and outgoing neutrons are treated as plane waves. The summation over all initial and final states, with the assumption of an unpolarised beam of neutrons,

leads to:

$$\frac{d^2\sigma}{d\Omega dE_f} = \frac{k_f}{k_i} \left(\frac{m_n}{2\pi\hbar^2}\right)^2 \sum_{\lambda_i,\lambda_f} p_{\lambda_i} |\langle\lambda_f|V(\boldsymbol{Q})|\lambda_i\rangle|^2 \, \delta(E + E_i - E_f), \qquad (3.9)$$

where p_{λ_i} is the probability distribution of initial states, and $V(\boldsymbol{Q})$ is the Fourier transform of the interaction potential $V(\boldsymbol{r})$, i.e.

$$V(\boldsymbol{Q}) = \int V(\boldsymbol{r})e^{i\boldsymbol{Q}\cdot\boldsymbol{r}} d\boldsymbol{r}. \qquad (3.10)$$

The scattering cross-section therefore depends on the type of interaction between the neutron and the matter it scatters from, and this general expression can be applied to different interaction potentials.

3.4.3 Nuclear interaction

Although in this thesis I am interested in measuring magnetic scattering, the dominant contribution in a neutron scattering experiment will come from nuclear scattering. It will give strong backgrounds to magnetic measurements, so I give a brief summary of nuclear interactions here. The interaction results from the strong force acting between the neutron and nuclei in the sample, over a very short range. It is approximated by

$$V_N(\boldsymbol{r}) = \frac{2\pi\hbar^2}{m_n} \sum_j b_j \delta(\boldsymbol{r} - \boldsymbol{r}_j), \qquad (3.11)$$

where a neutron at position $\boldsymbol{r}$ interacts with the jth nucleus at position $\boldsymbol{r}_j$. b_j is the scattering length, which represents the amplitude with which neutrons are scattered by the atomic species at $\boldsymbol{r}_j$. The values of b_j have been determined experimentally and are tabulated in Ref. [78].

It is possible to express the partial differential cross-section as a sum of a coherent term and an incoherent term:

$$\frac{d^2\sigma}{d\Omega dE_f} = \left.\frac{d^2\sigma}{d\Omega dE_f}\right|_{coh} + \left.\frac{d^2\sigma}{d\Omega dE_f}\right|_{inco}. \qquad (3.12)$$

Equations 3.9, 3.10 and 3.11 can be used to show that coherent scattering results from interference effects between the nuclei — resulting in (elastic) Bragg scattering and (inelastic) phonon scattering. Incoherent scattering is related to time correlations for individual atom environments — such as isotope effects and vibrational transitions. Usually in crystalline solids the incoherent scattering is observed as an isotropic background and is disregarded.

3.4.4 Magnetic interaction

The magnetic scattering interaction is between the magnetic dipole moment of the neutron and the magnetic fields within the sample. These fields are produced by the

spin and orbital momentum of unpaired electrons. The magnetic moment of the neutron is

$$\boldsymbol{\mu}_{\mathrm{n}} = -\gamma \mu_{\mathrm{N}} \boldsymbol{\sigma}, \tag{3.13}$$

where μ_{N} is the nuclear magneton, $\gamma = 1.913$, and $\boldsymbol{\sigma}$ is the Pauli spin operator. The interaction potential is then of the form

$$V_{\mathrm{M}}(\boldsymbol{r}) = -\boldsymbol{\mu}_{\mathrm{n}} \cdot \boldsymbol{B}(\boldsymbol{r}), \tag{3.14}$$

where $\boldsymbol{B}(\boldsymbol{r})$ represents the magnetic flux density within the sample. Using Maxwell's equations, $\boldsymbol{B}(\boldsymbol{r})$ can be related to the magnetisation $\boldsymbol{M}$, so that the Fourier transform of the interaction potential is found to be

$$V_{\mathrm{M}}(\boldsymbol{Q}) = -\boldsymbol{\mu}_{\mathrm{n}} \cdot \boldsymbol{B}(\boldsymbol{Q}) = -\mu_0 \boldsymbol{\mu}_{\mathrm{n}} \cdot \boldsymbol{M}_{\perp}(\boldsymbol{Q}), \tag{3.15}$$

where $\boldsymbol{M}_{\perp}(\boldsymbol{Q})$ is the component of the magnetization perpendicular to the scattering vector $\boldsymbol{Q}$.

In general $\boldsymbol{M}_{\perp}(\boldsymbol{Q})$ is complicated, but here an approximation for the case of $3d$ electrons can be used, as I am interested in magnetic scattering from Fe^{2+}. For iron, and many other $3d$ transition metal ions in solids, the orbital angular momentum is usually quenched and this allows the magnetisation to be written as

$$\boldsymbol{M}(\boldsymbol{Q}) = -g \mu_{\mathrm{B}} f(\boldsymbol{Q}) \boldsymbol{S} = f(\boldsymbol{Q}) \boldsymbol{\mu}. \tag{3.16}$$

$\boldsymbol{\mu}$ is the dipole moment of the scattering electrons, $\boldsymbol{S}$ is the spin quantum number, and $g = 2$ for fully quenched orbital angular momentum. $f(\boldsymbol{Q})$ is known as the *magnetic form factor*, and it accounts for the finite spatial extent of the interaction.

The magnetic form factor is ion specific and an estimation of its functional form for many ions can be calculated from tables (see Ref. [79]). From Eq. 3.9 it is known that terms in the interaction potential are squared when they appear in the partial differential cross-section, so it is $f^2(\boldsymbol{Q})$ that affects the intensity of scattered neutrons. The form of $f^2(\boldsymbol{Q})$ for Fe^{2+} is plotted in Fig. 3.2, which shows that $f^2(\boldsymbol{Q})$ — and therefore the scattering intensity — decreases quickly with increased Q. This sharp decrease does not occur for the nuclear scattering where the interaction potential is so short range that it is described by a delta function (Eq. 3.11). The Q dependence of the scattering is one way of separating nuclear and magnetic contributions.

3.4.5 Inelastic cross-section and response function

Returning to the expression for the partial differential cross-section, for magnetic inelastic scattering it is useful to express $d^2\sigma/d\Omega dE_{\mathrm{f}}$ as

$$\frac{d^2\sigma}{d\Omega dE_{\mathrm{f}}} = \left(\frac{\gamma r_0}{2}\right)^2 g^2 f^2(\boldsymbol{Q}) \frac{k_{\mathrm{f}}}{k_{\mathrm{i}}} \bar{S}(\boldsymbol{Q}, E), \tag{3.17}$$
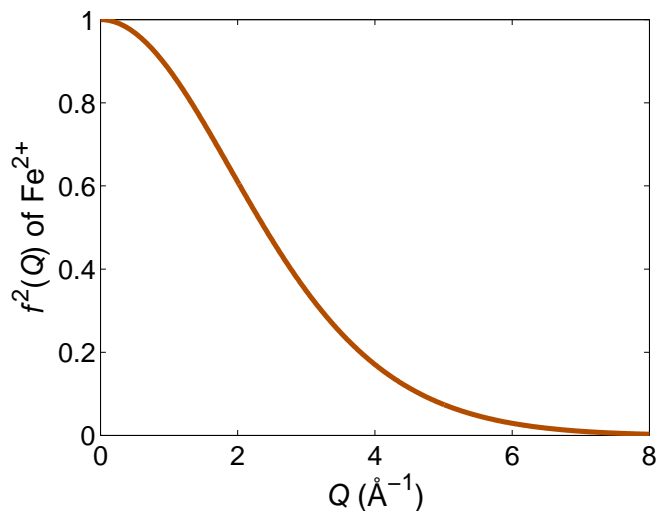
Figure 3.2: Squared form factor of Fe^{2+} Q dependence of the square of the magnetic form factor for an Fe^{2+} ion. Estimated from the $\langle j_0 \rangle$ contribution as detailed in Chapter 2.5 of Ref. [79].

where $r_0 = \mu_0 e^2/(4\pi m_e)$ is the classical radius of the electron and $\bar{S}(\boldsymbol{Q}, E)$ is a form of the *response function*. $\bar{S}(\boldsymbol{Q}, E)$ is related to the Fourier transform of the time-dependent correlation function for the magnetisation, and can be written as

$$\bar{S}(\boldsymbol{Q}, E) = \sum_{\alpha\beta}(\delta_{\alpha\beta} - \hat{Q}_\alpha \hat{Q}_\beta) S^{\alpha\beta}(\boldsymbol{Q}, E), \tag{3.18}$$

$$S^{\alpha\beta}(\boldsymbol{Q}, E) = \frac{1}{2\pi\hbar} \int_{-\infty}^{\infty} \langle \boldsymbol{S}^\alpha(-\boldsymbol{Q}, 0)\boldsymbol{S}^\beta(\boldsymbol{Q}, t)\rangle e^{-iEt/\hbar} dt, \tag{3.19}$$

where $\{\alpha, \beta\} = \{x, y, z\}$ are cartesian components. This includes the scattering which is dependent on the magnetic fluctuations in the system. The $(\delta_{\alpha\beta} - \hat{Q}_\alpha \hat{Q}_\beta)$ term selects only the component of magnetisation which is perpendicular to the scattering vector $\boldsymbol{Q}$.

Defining $d^2\sigma/d\Omega dE_\mathrm{f}$ and $\bar{S}(\boldsymbol{Q}, E)$ in this way is helpful as it separates the contribution due to the experimental set-up from a term depending only on $\boldsymbol{Q}$ and E. In general it is $\bar{S}(\boldsymbol{Q}, E)$ that can be calculated from theory and compared between experiments.

In a real system at a given temperature, T, there will be a number of excitations present in the system due to thermal population. The proportion in which the excited state and ground states are occupied is given by the Boltzmann factor. Therefore, there is a relationship between the number of scattering events that arise from neutron energy gain and those from neutron energy loss. This relationship is taken account by the *principle of detailed balance*, resulting in

$$\bar{S}(\boldsymbol{Q}, E) = e^{E/k_\mathrm{B}T}\bar{S}(-\boldsymbol{Q}, E).^4 \tag{3.20}$$

---

[4] In this definition elastic scattering is not included in $\bar{S}(\boldsymbol{Q}, E)$.

3.4.6 Relationship with susceptibility

In § 3.2.2 I discussed the magnetic susceptibility of the form $\boldsymbol{M} = \chi\boldsymbol{H}$. This, however, ignores variation of $\boldsymbol{H}$ in space and time. In general $\boldsymbol{M}$ and $\boldsymbol{H}$ are not in phase and χ is therefore complex, $\chi(\boldsymbol{Q}, E) = \chi'(\boldsymbol{Q}, E) - i\chi''(\boldsymbol{Q}, E)$. As the neutron effectively provides a magnetic perturbation to the system that varies in space and time, this dynamic or generalised susceptibility must be considered. The *fluctuation dissipation theorem*, along with the detailed balance factor, allows the dynamic response function for INS to be related to the imaginary part of the magnetic susceptibility.

$$\chi''(\boldsymbol{Q}, E) = \pi \left(1 - e^{-E/k_{\mathrm{B}}T}\right) \bar{S}(\boldsymbol{Q}, E) \tag{3.21}$$

The imaginary part of the susceptibility has the character of an absorption coefficient, i.e. it describes the absorption of energy due to magnetic fluctuations. The term $\left(1 - e^{-E/k_{\mathrm{B}}T}\right)^{-1}$ is known as the *Bose population factor*, and can be used to adjust for thermal population of states when comparing data sets taken at different temperatures.

It is also useful to define a property called the *local susceptibility*, or Q-averaged susceptibility, because it gives a measure of local magnetic correlations and the overall strength of excitations. It is defined as

$$\chi''(E) = \frac{\int \chi''(\boldsymbol{Q}, E) d\boldsymbol{Q}}{\int d\boldsymbol{Q}}, \tag{3.22}$$

where the average is over all BZs.

3.5 Neutron scattering experiments

I will now discuss some of the practical elements of performing a neutron scattering experiment. Due to the difficulty and expense of producing a beam of neutrons, these sorts of experiment are carried out at large central facilities — the results presented in this thesis are from experiments performed at the ISIS neutron and muon facility, UK, and at the Institut Laue Langevin (ILL), France, and I will briefly discuss the alternative methods they use to produce neutrons. All of the INS measurements I report were performed using the time-of-flight (ToF) technique on direct-geometry chopper spectrometers. I will describe this type of instrument, then discuss the form of the resulting datasets, and finally discuss the environment and containment of the sample during these experiments.

3.5.1 Neutron Sources

Neutrons are produced by two methods for use in experiments, by spallation (as at the ISIS facility) or by a nuclear reactor (as at the ILL). At a spallation neutron source a beam of protons is accelerated to high speeds before being directed towards a heavy metal target. In the target the process of spallation occurs: the impact of the protons excites the nuclei in the metal, which then undergo neutron emission until they relax

to a stable nuclear state. The beam of protons is pulsed, so small bunches of protons arrive at the target at a well defined time and produce pulses of neutrons as a result. At a reactor source uranium fuel is used to produce neutrons by the nuclear fission reaction

$$^{227}\text{U} + \text{n} \rightarrow 2.5\text{n} + 250\,\text{MeV} + \text{nuclei}. \tag{3.23}$$
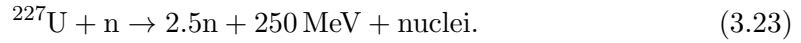
The nuclear reactor is designed to produce more neutrons than required to maintain the reaction process, so that some may exit the reactor and be used for scattering experiments. In fact, reactor sources produce a very high continuous flux of neutrons.

In both cases, after the processes above, the neutrons pass through a *neutron moderator* to modify their energy spectrum. This is a volume of material (e.g. water) placed immediately after the target/reactor, with which neutrons exchange energy. This lowers their energies to a range that is useful for experiments. All the processes described take place on a timescale short enough that they can be neglected with respect to the time between pulses on a spallation source, so well-defined pulses of neutrons are produced at these sources.

3.5.2 Time-of-flight technique

The ToF technique relies on measuring the time at which scattered neutrons reach the detector. Provided that the time at which the neutrons reach the sample is known, their arrival time at the detectors allows their velocity to be inferred, and therefore their energy. In the experiments of interest only neutrons with a small range of energies, centred on E_i, are allowed to reach the sample. Therefore, there is a well defined time, t_0, at which neutrons that elastically scatter reach a detector. Neutrons arriving with time $t_\text{ToF} < t_0$ have gained energy in the scattering process; neutrons with $t_\text{ToF} > t_0$ have lost energy. Because the flight path of the neutron is known, the energy transferred to the sample, E, can be calculated from $E = \frac{1}{2}m_\text{n}v^2 = \frac{1}{2}m_\text{n}L_2^2/(t_\text{ToF} - t_0)^2$, where L_2 is the distance from sample to detector (Fig. 3.3(a)).

This scenario also allows the determination of $\boldsymbol{Q}$. Because $E_\text{f} = E_\text{i} - E$ is known, k_f can be determined from $k_\text{f} = \sqrt{2m_\text{n}E_\text{f}/\hbar^2}$. The position of the detector that the neutron hits is also known, so $\boldsymbol{k}_\text{f}$ can be determined. $\boldsymbol{k}_\text{i}$ is known from the instrument set-up, so it simply a case of using the standard scattering triangle (see Fig. 3.1) to determine $\boldsymbol{Q}$.

This is practically feasible because neutrons in the thermal energy range are travelling at velocities of order $2000\,\text{ms}^{-1}$, so their energy can be determined if L_2 is of the order of meters. The ToF technique is well suited to spallation sources where the neutron beam is pulsed, so the neutrons in one pulse are scattered by the sample and detected before the next pulse arrives at the sample. At a reactor source, where the beam is continuous, disk choppers must be used to make a pulsed beam, which results in the loss of most of the available neutron flux. However, because of the very high continuous flux of neutrons at a reactor source like the ILL, it is still practically useful to build this sort of instrument.
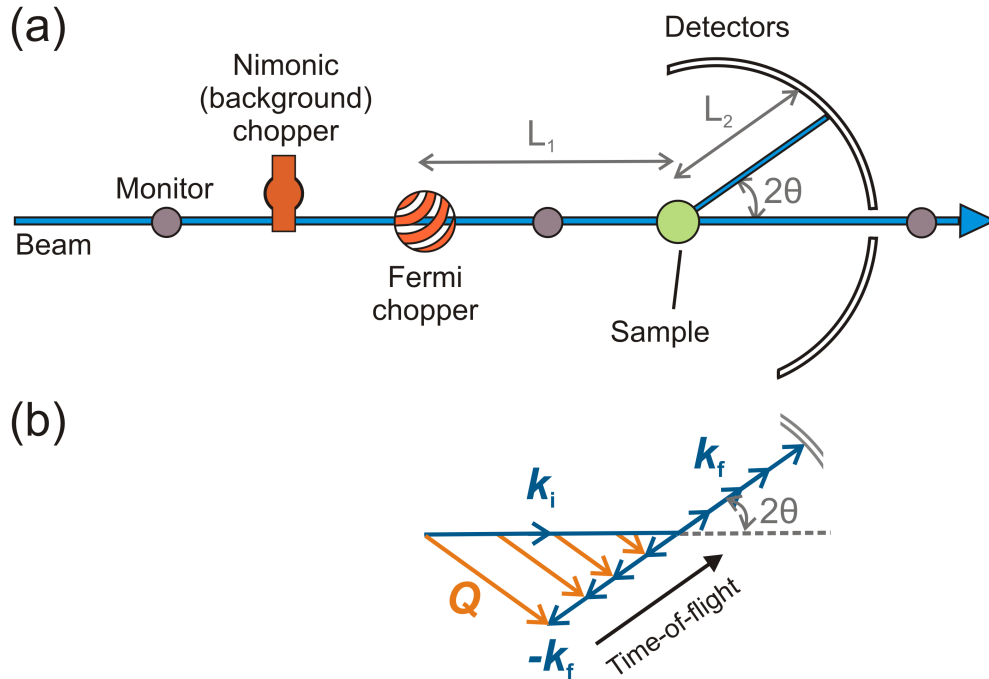
Figure 3.3: Direct-geometry spectrometer and scattering vectors. (a) Schematic representation of the main components of a direct-geometry chopper spectrometer, with unscattered and 2θ scattering beam paths shown. This view is a horizontal section, as if looking down on the instrument from above. (b) The scattering triangle for scattering into one small section of the detectors, at an angle 2θ. A range of $\mathbf{k}_\mathrm{f}$s, and corresponding $\mathbf{Q}$s, are shown. Neutrons with these $\mathbf{k}_\mathrm{f}$s would all be detected in the same section of the detectors, but they would arrive at different times. The time of arrival at the detector increases with decreasing k_f, as indicated by the black arrow.

3.5.3 Direct-geometry spectrometers

The vast majority of the results I present in this thesis are from experiments performed on the MERLIN chopper spectrometer at the ISIS facility; details of this instrument can be found in Ref. [80]. In Chapter 6, I also present results from the IN5 chopper spectrometer at the ILL facility; more details of this instrument can be found in Ref. [81]. The following discussion, therefore, is focused towards a discussion of MERLIN's features, but is also largely applicable to IN5.

The basic set-up of a direct-geometry chopper spectrometer is shown in Fig. 3.3(a). The beam of neutrons from a pulsed source must initially pass through a nimonic chopper. This blocks very fast neutrons and other high-energy radiation that are emitted from the moderator shortly after the proton pulse hits the target. If they were not blocked by the chopper, these neutrons would 'catch up' with slow neutrons (that scattered with large energy loss) from the previous pulse and cause a large background on the high-E data.

The beam then passes through a Fermi chopper, which is carefully designed to

select a single neutron energy, E_i, for the experiment. It is a cylindrical drum that rotates about its axis and consists of alternate slats of neutron absorbing and neutron transparent materials (such as B and Al, respectively). These slats are curved so that, as the drum rotates, only neutrons of a particular energy can follow the path of a transparent slat and reach the other side without being absorbed. The range of energies that can actually traverse the Fermi chopper, $E_i \pm \Delta E_i$, is determined by the frequency of rotation — higher frequencies give better resolution (smaller ΔE_i therefore smaller ΔE_f), but at the expense of flux — optimal conditions are chosen for the particular experiment being performed.

There are also monitors placed at various positions along the beam path, which are essentially very inefficient neutron detectors (so that they do not significantly reduce the beam flux). These allow variations in beam intensity to be accounted for (§ 3.5.5).

The detectors that finally measure scattered neutrons must give both the arrival time and position of the neutron. The time of interest is

$$t = \left(\frac{m_n}{2}\right)^{\frac{1}{2}} \left(\frac{L_1}{E_i^{\frac{1}{2}}} + \frac{L_2}{E_f^{\frac{1}{2}}}\right), \tag{3.24}$$

the flight time of the neutron from the Fermi chopper position — where E_i is selected — to the detectors. This equation is solved to find E_f and in turn E is found. The large area of detector coverage around the sample is a key feature of the direct-geometry chopper spectrometer set-up — in particular on MERLIN where the detectors cover a very large angular range. To understand the significance of this it is helpful to consider the scattering triangles depicted in Fig. 3.3(b). All neutrons that are scattered by an angle 2θ will reach the same point in the detectors. However, because the magnitude of their momentum, k_f, varies, they take different times to reach the detector. This allows the E_f and $\boldsymbol{Q}$ for each one to be determined. Combining this with the placement of detectors over a wide range of angles allows a huge range of possible $(\boldsymbol{Q}, E)$ scattering states to be detected. It is this property that makes direct-geometry chopper spectrometers so useful. Covering vast regions of $(\boldsymbol{Q}, E)$-space is highly advantageous when searching throughout the BZ for evidence of magnetic excitations, and is not possible by other conventional techniques.

The detectors depicted in Fig. 3.3(a) actually extend vertically out of the plane of the diagram, so there is angular coverage for scattering in two dimensions. This is made possible by ^{3}He detectors: long, narrow tubes that are position sensitive along their length. Many of these side by side around an arc, as indicated in Fig. 3.3(a), allow the position of detection of the neutron to be measured in two dimensions.

This set-up means that two of the four experimental dimensions of interest are coupled: Q_z and E out of (Q_x, Q_y, Q_z, E). Q_z is the component of momentum transfer along the direction of $\boldsymbol{k}_i$. For a three-dimensional (3D) system this means the crystal must be rotated and many measurements made in order to map out the excitations in all three directions in the BZ, (H, K, L). In a 2D system only two perpendicular wavevectors in the crystal, e.g. H and K, are of interest, so the crystal is simply aligned with $L \parallel \boldsymbol{k}_i$ to retrieve all of the desired information. I will return to this point

in Chapters 4 and 7.

3.5.4 Powder averaging

In this thesis I report several measurements of powder samples. The use of a polycrystalline material affects the information that can be extracted from the data. Although four experimental dimensions (Q_x, Q_y, Q_z, E) are still found, these can no longer be related to directions in the crystal's BZ. This is because the crystallites in the polycrystalline sample are randomly oriented. Consider scattering with a particular energy transfer E. Different wavevectors, e.g. (H_1, K_1, L_1) and (H_2, K_2, L_2), with the same magnitude, $|(H_1, K_1, L_1)| = |(H_2, K_2, L_2)|$, in different crystallites can cause neutrons to be scattered to the same point in the detectors, making the wavevectors indistinguishable. Additionally, because the direction of wavevector (H_1, K_1, L_1) is randomly oriented across crystallites, the (H_1, K_1, L_1) scattering will arrive in the detectors at all points that correspond to the magnitude $|(H_1, K_1, L_1)|$, i.e. all points of the detector that are at an angle 2θ (see Fig. 3.3(a)). This means that the intensity seen in the detectors due to scattering from (H_1, K_1, L_1) [and (H_2, K_2, L_2) etc.] is spread around a ring centred on $(0, 0, 0)$, not at a high-intensity point as in the single crystal case.

Powder averaging means that less information can be extracted from data collected from polycrystalline samples. The results of powder experiments are presented in (Q, E)-space rather than $(\boldsymbol{Q}, E)$-space. A less obvious disadvantage of powder measurements is that it is not always possible to determine the correct value of the magnitude, M, of the wavevector from which the scattering originates, $M = |(H, K, L)|$. Unless the scattering is sharp, as would be expected from a Bragg peak for example, then the position of the maximum intensity in Q does not equal M.

For example, consider a 2D magnetic system in which the magnetism is characterised by wavevector $(0.5, 0.25)$. This would produce a rod of scattering parallel to Q_z in (Q_x, Q_y, Q_z)-space. For a perfect crystal this rod would be a delta function in the (Q_x, Q_y)-plane centred on $(0.5, 0.25)$, with infinite extent in the Q_z direction. In reality, however, the scattering would have some width in Q_x and Q_y. I have modelled this using a 2D Gaussian: a function that has a Gaussian line shape in both Q_x-intensity and Q_y-intensity planes. The red line in Fig. 3.4 shows the shape of the peak that was produced by powder averaging a rod of scattering with an isotropic 2D Gaussian in-plane intensity profile. This model assumes that the 2D Gaussian is centred on wavevector $(0.5, 0.25)$ for a material with square-lattice parameter $a = 2.7\,\text{Å}$. The magnitude of this wavevector is $Q = |(0.5, 0.25, 0)| = 1.30\,\text{Å}^{-1}$ (see the dashed line in Fig. 3.4). The maximum value of the function plotted in red in Fig. 3.4 occurs at $Q = 1.36\,\text{Å}^{-1}$. This treatment has ignored the effect of the form factor (§ 3.4.4). Including this effect produces only a small change in the peak shape, as shown by the blue line in Fig. 3.4 which was calculated using the form factor for Fe^{2+}. In reality, the systems I discuss in this thesis are quasi-2D magnetic materials, so I expect the scattering to be intermediate between 2D and 3D. I discuss the effects of powder averaging in Chapters 5 and 8.
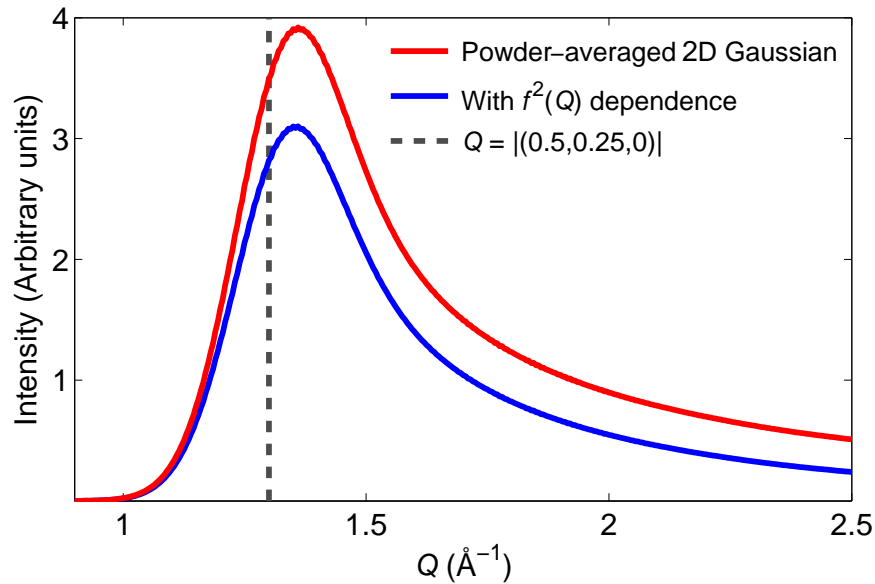
Figure 3.4: Powder-averaged 2D Gaussian functions. The red line is the result of a calculation of the effect of powder averaging a 2D Gaussian function, as described in the text. The blue line is the result of adding the effect of the form factor of Fe^{2+} to the calculation.

3.5.5   Normalisation of results

Equation 3.7 shows that the quantity measured in an experiment depends on the incident beam flux and efficiencies of the detectors. It is possible to correct for these effects on a direct-geometry spectrometer. The incident flux is known from the beam monitors (Fig. 3.3(a)) for each measurement of the sample. The detector efficiencies are found by making a measurement of a vanadium standard in addition to the measurement of the sample. Vanadium is used for the normalisation because it is an almost entirely incoherent scatterer. This means that vanadium gives a scattering response that is flat in Q (§ 3.4.3), so it will scatter isotropically into all detectors. A measurement of vanadium is made for every combination of Fermi chopper energy and frequency used to measure the sample. To process the data and perform the normalisation, a program called *Homer* [82] was used throughout this thesis. *Homer* requires input of the sample mass, the sample relative molecular mass and the mass of vanadium used. The data is converted to a normalisation that corresponds to a particular choice of the response function:

$$S(\boldsymbol{Q}, E) = \frac{k_\mathrm{i}}{k_\mathrm{f}} \frac{d^2\sigma}{d\Omega dE_\mathrm{f}} = \left(\frac{\gamma r_0}{2\mu_B}\right)^2 f^2(\boldsymbol{Q})\bar{S}(\boldsymbol{Q}, E), \tag{3.25}$$

where $S(\boldsymbol{Q}, E)$ [useful for the measurement] has been related to $\bar{S}(\boldsymbol{Q}, E)$ [useful for comparison to theory] using Eq. 3.17.

The units of $S(\boldsymbol{Q}, E)$ are $\mathrm{mb\,sr}^{-1}\,\mathrm{meV}^{-1}\,\mathrm{f.u.}^{-1}$, where mb is millibarns (mb = $10^{-31}\mathrm{m}$), sr is steradians, meV is milli-electron volts, and f.u. stands for formula unit (of the sample). Frequently throughout this thesis the results of experiments in terms

of $S(\boldsymbol{Q}, E)$ will simply be referred to as the *intensity* of the measurement in units $\mathrm{mb\,sr^{-1}\,meV^{-1}\,f.u.^{-1}}$. These units are often referred to as *absolute units* as they allow direct comparisons between intensities from different experiments.

3.5.6 Sample environment

To measure samples in the superconducting state, experiments have to be performed at low temperatures. For the experiments I report in this thesis, I achieved this by placing the samples inside a top-loading closed-cycle refrigerator, in the case of MERLIN experiments, and inside a helium cryostat, in the case of IN5 experiments. These are specially designed to minimise the amount of material in the neutron beam to ensure a minimum of background scattering. These set-ups protect samples from air exposure because the sample sits in an evacuated chamber and is only exposed to He exchange gas.

For the duration of an experiment the samples are contained within, or mounted on, specially designed aluminium holders. Aluminium is chosen as it has an extremely-low incoherent scattering cross-section, i.e. it gives a very low-background signal (§ 3.4.3). For measurements on powder samples, the powder is placed in an aluminium foil packet and this is wrapped in an annulus around the edge of of a cylindrical aluminium can. This set-up is chosen in order to have the thinnest possible sample, as this minimises absorption of the neutron beam passing through the sample. The container can be sealed in an He environment to protect the sample against air exposure while the can is loaded onto the instrument. For the experiments in this thesis, the quality of single crystals was checked on the ALF instrument at the ISIS facility. This instrument was also used for aligning crystals. Single crystals were first aligned individually, and then coaligned by attaching them to a specially designed array of aluminium holders.

Magnetic dynamics in the parent-phase $SrFe_2As_2$

Contents

4.1   Introduction

The role of magnetic fluctuations in high-temperature superconductors remains a controversial topic. In iron-based superconductors a key issue is whether the magnetism is better described by an itinerant [71] or a localised picture [83]. This will have a major impact on how the links between superconductivity and magnetism can be understood. One of the most direct ways to determine the nature of the magnetism is to use INS to probe the magnetic excitation spectrum. By comparing the results to theoretical models based on weak (itinerant) or strong (localised) coupling the character of the magnetism can be deduced (§ 2.3.1). In the iron-based superconductors it is helpful to make these measurements on the magnetically ordered parent-phase materials where the fluctuations are expected to be very strong. Once the spectrum of the magnetic fluctuations in the parent phase has been determined, similar measurements on the superconducting materials can be better understood. Here I discuss the parent-phase $SrFe_2As_2$, because it displays the structural distortion and SDW order described in § 2.2 and § 2.3 (see Fig. 4.1), and because single crystals were available for the measurement.

$SrFe_2As_2$ is from the XFe_2As_2 (where X = Ca, Sr or Ba) family of materials of which $BaFe_2As_2$, discussed in Chapter 2, is also a member. Previous INS measurements of the magnetic dynamics in XFe_2As_2 systems have been described in terms of linear spin-wave theory [38, 84, 85]. The models are local-moment 'J_1–J_2' models that include nearest-neighbour (J_1) and next-nearest neighbour (J_2) Fe–Fe exchange interactions. An interesting result from this analysis applied to $CaFe_2As_2$ is the very large difference between the two in-plane nearest neighbour exchange parameters, J_{1a} and J_{1b}, despite the small orthorhombic splitting [85]. Various mechanism have been proposed to explain this anisotropy, including electronic nematic ordering [86], orbital ordering [87], and the crystal structure itself [26]. An important piece of information, lacking up to now, is whether the anisotropy is modified on warming above the combined magnetic and structural transition temperature, $T_{N,s}$, i.e. whether the magnetic spectrum is responsive to the change of symmetry from orthorhombic to tetragonal. Most measurements in these systems, including those reported here, are made on twinned crystals because the orthorhombic a-axis can lie along two directions that were equivalent in the tetragonal symmetry. However, resistivity measurements performed on detwinned samples of $Ba(Fe_{1-x}Co_x)_2As_2$ found that there is a large electronic anisotropy that persists above $T_{N,s}$ [88]. Previous INS measurements of XFe_2As_2 systems above $T_{N,s}$ have only probed low energies [85, 89]. Given the possible role of magnetic fluctuations in the origin of superconductivity in iron-based systems, further data on the magnetic spectrum in the tetragonal phase, and its relation to that in the orthorhombic phase, are of great interest.

The questions I set out to answer in this chapter are: (i) are the magnetic interactions in $SrFe_2As_2$ anisotropic in the ordered state, like in other XFe_2As_2 systems (ii) do the spin excitation spectra change significantly on warming above $T_{N,s}$ and (iii) how robust is the local-moment description of the INS spectra? The results I describe probe the magnetic excitations in $SrFe_2As_2$ throughout the BZ over the energy range $5 < E < 260$ meV, below and above $T_{N,s}$. I compare the data to calculations for a lo-

calised J_1–J_2 model and a five-band itinerant model, and find that a better qualitative description comes from the itinerant model. The recorded spectrum is not significantly altered on warming above $T_{\mathrm{N,s}}$, and I will discuss the implications this has for theories of electronic and nematic ordering.

The results presented in this chapter have been published in Ref. [90]. I present simply a summary of the main results, rather than a detailed analysis of all the data, because this work sets the scene so that in subsequent chapters I can focus on measurements of superconducting materials, and because the crystal growth and data analysis presented here were performed by collaborators, as indicated below.

4.2 Crystal growth and characterisation

The single crystals of $SrFe_2As_2$ for this experiment were grown by Jack Gillett, Sitikantha D. Das, and Suchitra E. Sebastian in the Cavendish Laboratory, University of Cambridge, UK. The crystals were grown by the self-flux method as described in Ref. [91]. As well as characterisation by bulk property measurements, microprobe analysis was used to confirm the homogeneity of the crystals [91], and quantum oscillations experiments were performed on samples from the same growth [92].

The crystals show a well-defined magnetic-structural transition temperature of $T_{\mathrm{N,s}} = 192\,\mathrm{K}$. On cooling through $T_{\mathrm{N,s}}$, the crystal symmetry changes from tetragonal $I4/mmm$ to orthorhombic $Fmmm$, and the antiferromagnetic SDW state develops with propagation vector $\boldsymbol{Q} = (0.5, 0.5, 1)$ expressed in the $I4/mmm$ unit cell. The orthorhombic structure and magnetic order in the Fe-plane are shown in Fig. 4.1. The orthorhombic distortion is small in $SrFe_2As_2$, with lattice parameters $a = 5.578\,\text{Å}$ and $b = 5.518\,\text{Å}$ at $T = 90\,\mathrm{K}$; the c-axis is $12.297\,\text{Å}$ at the same temperature [93]. As the distortion is small and the magnetic dynamics in $SrFe_2As_2$ are relatively 2D, I will index wavevectors using only in-plane components expressed in the one-Fe unit cell (H, K) [§ 2.3]. The one-Fe cell has lattice parameter $a = b = 2.8\,\text{Å}$ in the paramagnetic phase. In this convention the magnetic propagation vector is $\boldsymbol{Q}_{\mathrm{SDW}} = (0.5, 0)$, i.e. corresponds to the point labelled 'X' in Fig. 4.5(b). All three relevant BZs are illustrated in this figure.

4.3 Experimental set-up

To obtain a sample with large enough mass to give an appreciable signal in INS experiments, many small single crystals had to be coaligned. Quality checking and coalignment of the individual crystals were performed on the ALF instrument at the ISIS facility. A total of twenty-one crystals were coaligned to give a mosaic sample of total mass $5.4\,\mathrm{g}$, with a uniform mosaic of $4°$ (from the full-width at half-maximum [FWHM] of representative Bragg peaks).

The INS experiments were performed on the MERLIN chopper spectrometer at the ISIS facility (§ 3.5). Spectra were recorded at temperatures of 6, 212($\approx T_{\mathrm{N,s}} + 20\,\mathrm{K}$), and $300\,\mathrm{K}$, with incident energies $E_{\mathrm{i}} = 50, 100, 180, 300$, and $450\,\mathrm{meV}$. The sample was aligned with the c-axis parallel to the incident neutron beam direction,
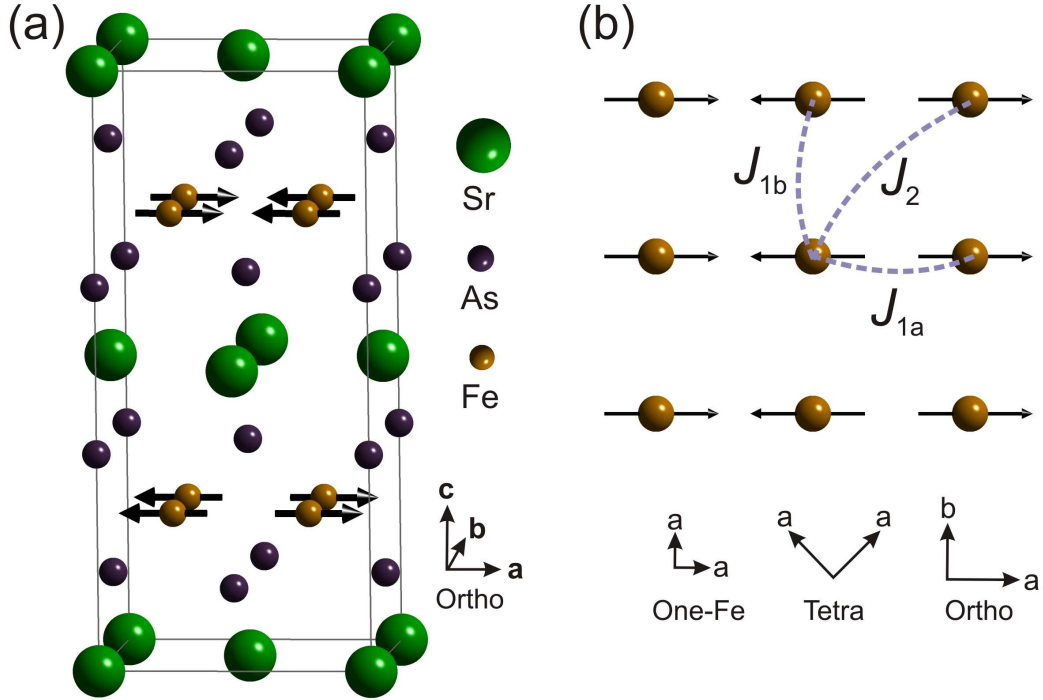
Figure 4.1: Crystal and magnetic structure of SrFe$_2$As$_2$. (a) One unit cell of SrFe$_2$As$_2$ in the low-temperature orthorhombic phase. The arrows represent the magnetic ordering associated with the iron sites in this phase. (b) One layer of Fe in the a–b-plane. Arrows again represent the spin associated with SDW order. The dashed lines represent the key exchange parameters in the J_1–J_2 model (see the main text).

and the a-axis in the horizontal plane, in order to access scattering in the (H, K)-plane. Data from equivalent positions in reciprocal space were averaged to improve statistics. Scattering from a standard vanadium sample was used to normalise the data, as described in § 3.5.5, where here the units mb sr^{-1} meV^{-1} f.u.$^{-1}$ refer to the f.u. SrFe$_2$As$_2$.

4.4   Results and analysis

The general form of the magnetic scattering from SrFe$_2$As$_2$ at $T = 6\,\mathrm{K} \ll T_{\mathrm{N,s}}$ is illustrated in Fig. 4.2(a). This energy-momentum slice shows intensity dispersing out of the $\boldsymbol{Q}_{\mathrm{SDW}}$ positions, similar to the magnetic spectrum observed in CaFe$_2$As$_2$ [84, 85]. These data are from the measurement with $E_{\mathrm{i}} = 450\,\mathrm{meV}$, and the intensities have been multiplied by E to enhance the high-energy part of the spectrum. Figures 4.2(b) and (c) show that at $T = 212\,\mathrm{K} > T_{\mathrm{N,s}}$ and $T = 300\,\mathrm{K} \gg T_{\mathrm{N,s}}$, the spectrum remains very similar to that in the ordered state, i.e. strong AFM correlations persist well into the paramagnetic phase of SrFe$_2$As$_2$. The dispersion is seen in more detail in Fig. 4.3, which presents constant-energy cuts of the 6 K data for four different energies. A single peak, centred on $\boldsymbol{Q}_{\mathrm{SDW}} = (0.5, 0)$ at low energies, splits into a pair of peaks at $\sim$75 meV,
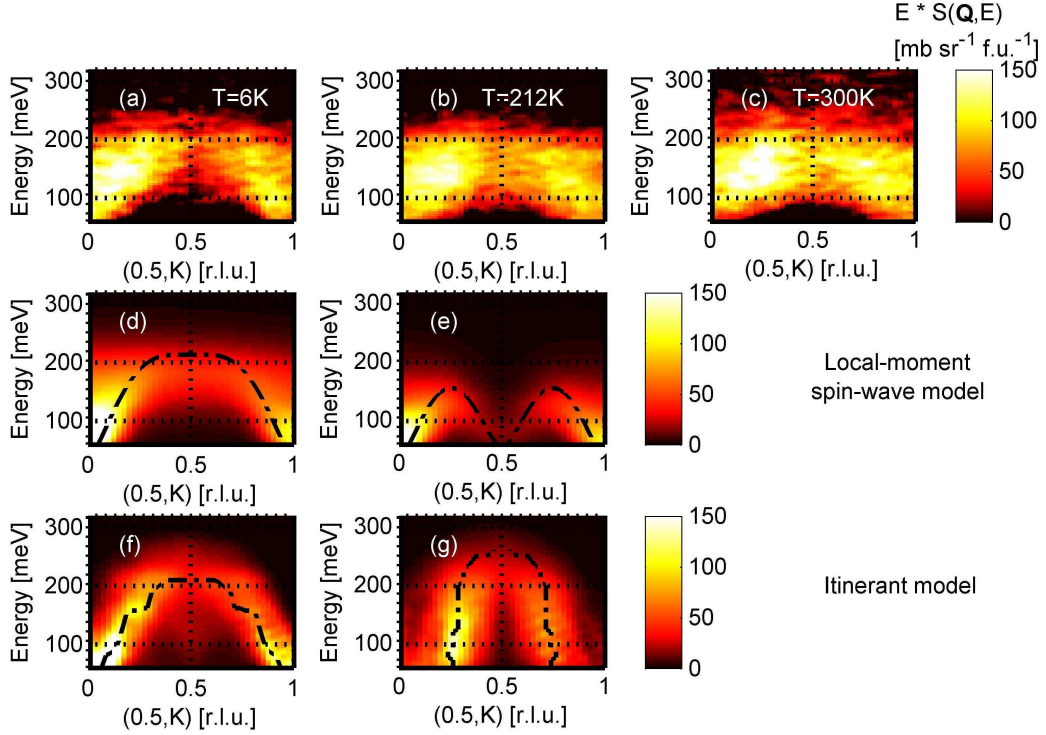
Figure 4.2: INS spectra from SrFe$_2$As$_2$ and theoretical models. The inelastic scattering response at (a) $T = 6\,\mathrm{K}$, (b) $T = 212\,\mathrm{K}$, and (c) $T = 300\,\mathrm{K}$. Simulations of the spectrum from a local-moment spin-wave model are shown in (d) for $J_{1\mathrm{a}} \neq J_{1\mathrm{b}}$ and (e) for $J_{1\mathrm{a}} = J_{1\mathrm{b}}$. The dashed lines in (d) indicate the simulated dispersion for the high-energy-fit parameters (see text) and in (e) for the $J_{1\mathrm{a}} = J_{1\mathrm{b}}$ calculation. (f) and (g) show the calculated $\chi''(\boldsymbol{Q}, E)$ for the SDW phase and the paramagnetic phase respectively, taken from Ref. [94] and convolved with the instrument resolution and rescaled in energy by 0.85. Dashed lines in these panels represent the loci of maximum intensity of the calculated $\chi''(\boldsymbol{Q}, E)$. The data shown in all panels have been multiplied by E to improve clarity. Reprinted figure from R. A. Ewings *et al.*, Phys. Rev. B, **83**, 214519, 2011 [90]. Copyright (2011) by the American Physical Society.

which continue to separate and broaden with increasing energy. These peaks converge on $\boldsymbol{Q} = (0.5, 0.5)$ at $E \sim 230\,\mathrm{meV}$.

Figure 4.4 provides a comparison of the spectra recorded at 6, 212, and 300 K for wavevectors near $(0.5, 0)$ and $(0.5, 0.5)$. The signals at higher temperatures are somewhat broader than at 6 K, but otherwise no marked differences associated with the change of structural symmetry were found, even well above $T_{\mathrm{N,s}}$.

To begin to address the questions set out in the introduction to this chapter, I compare the INS data with models of localised and itinerant behaviour. For the comparison to a local-moment Heisenberg-Hamiltonian model, the calculations and fitting were performed by Russell A. Ewings of the ISIS facility, Rutherford Appleton Laboratory, UK. The model is the standard one used to interpret the spin excitations in $X\mathrm{Fe}_2\mathrm{As}_2$ systems [38, 84, 85]; for a detailed description see R. A. Ewings *et al.* [90]. The key exchange parameters used in the model are illustrated in Fig. 4.1(b), as well as an
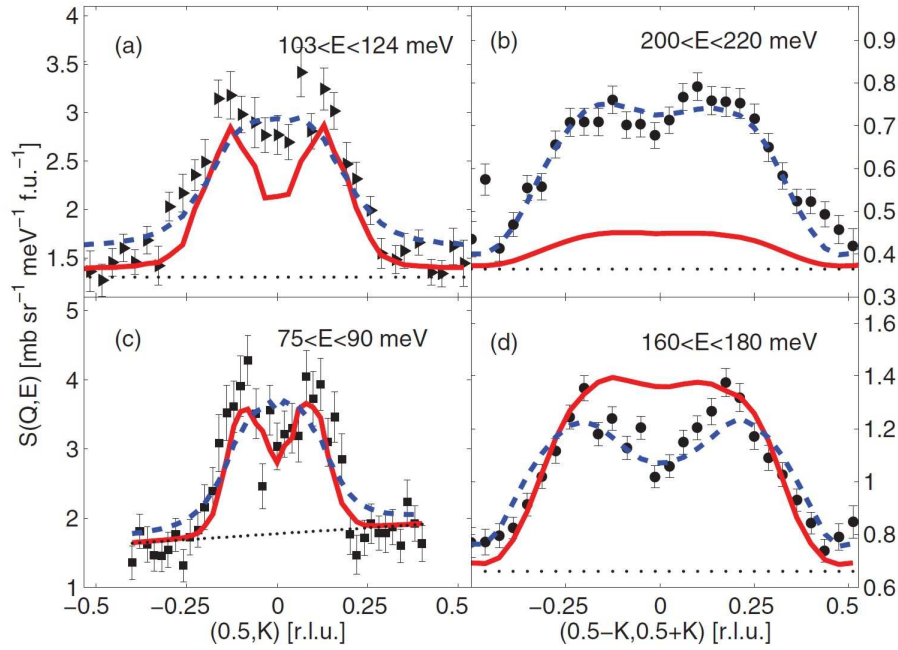
Figure 4.3: Constant-energy cuts. Cuts through the data taken at 6 K with incident neutron energies (c) $E_i = 180$ meV, and (a), (b), (d) $E_i = 450$ meV. Solid red lines and dashed blue lines are calculated from fits to the J_{1a}–J_{1b}–J_2 model with the low-energy and high-energy fit parameters, respectively. Dotted black lines indicate the estimated non-magnetic scattering from $Q = (1, 0)$. Reprinted figure from R. A. Ewings *et al.*, Phys. Rev. B, **83**, 214519, 2011 [90]. Copyright (2011) by the American Physical Society.

interplanar exchange, J_c, which is not illustrated. As discussed in § 3.5.3, because the c-axis was parallel to k_i, the $(0, 0, L)$ component of the spectrum was coupled to ToF. Hence the $(0, 0, L)$ component in the data is coupled to the energy transfer. However, determination of J_c is still possible by using several E_is in the fitting.

The simulations include the effect of the Fe form factor, and incorporated the resolution of the spectrometer in (Q, E)-space using the TOBYFIT software [95]. Fits were made to a set of one-dimensional data cuts over the entire energy range for which magnetic excitations were observed in the data. The calculations for different temperatures differ only in the damping. Good fits could only be achieved by fitting the lower energy ($E \lesssim 100$ meV) and higher energy ($E \gtrsim 100$ meV) parts of the low-temperature spectra separately. The best-fit parameters are summarised in Table 4.1, and Fig. 4.2(d) illustrates the results. Figure 4.2(e) illustrates the predicted scattering response if the crystal symmetry is imposed on the model, i.e. $J_{1a} = J_{1b}$.

To compare to an itinerant model, the results of Kaneshita and Tohyama [94] were used (Fig. 4.2(f) and (g)). They used a mean-field five-band model to described the XFe$_2$As$_2$ systems, and a random phase approximation treatment to calculate the imaginary part of the susceptibility $\chi''(Q, E)$ [Eq. 3.21]. Their results were convolved with the instrument resolution and the energy was rescaled by a factor of 0.85 to match the
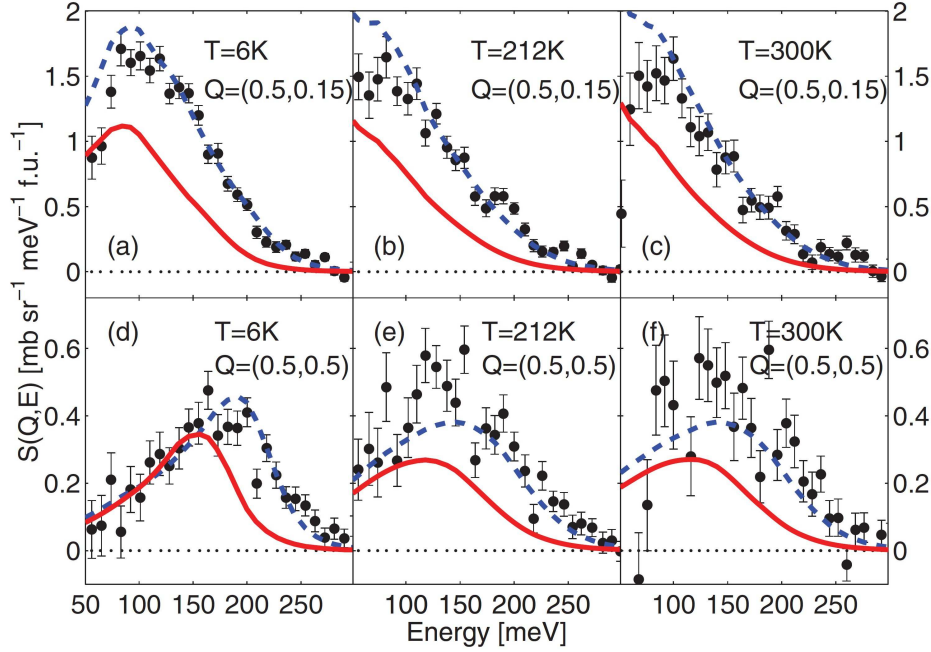
Figure 4.4: Constant-wavevector cuts. Cuts at constant in-plane $\boldsymbol{Q}$ through the data taken with $E_i = 450\,\text{meV}$. The left-hand panels show data at $T = 6\,\text{K}$, middle panels at $T = 212\,\text{K}$, and right-hand panels at $T = 300\,\text{K}$. (a), (b) and (c) show data from wavevector $\boldsymbol{Q} = (0.5, 0.15)$ and (d), (e) and (f) show data from wavevector $\boldsymbol{Q} = (0.5, 0.5)$. Solid red lines and dashed blue lines are calculated from the local-moment model low-energy and high-energy fit parameters, respectively. The dotted black lines represent the background, which is zero here because the non-magnetic background signal from $\boldsymbol{Q} = (1, 0)$ has been subtracted from these data for clarity. Reprinted figure from R. A. Ewings *et al.*, Phys. Rev. B, **83**, 214519, 2011 [90]. Copyright (2011) by the American Physical Society.

SrFe$_2$As$_2$ data. The calculated low-energy incommensurate behaviour in Fig. 4.2(g) is discussed in Ref. [94], and likely arises from limitations of the model discussed further below.

4.5   Discussion

The results of the experiments immediately show that there is little modification of the INS spectrum in SrFe$_2$As$_2$ upon crossing the structural and magnetic phase transition, even at temperatures significantly above $T_{\text{N,s}}$ (Fig. 4.2(a)-(c)). However, to understand the significance of this finding it should be put in context.

Superficially, the local-moment model appears to provide a reasonable overall description of the low-temperature data (see Fig. 4.2(a) and (d)). One robust outcome from the analysis is the large difference between J_{1a} and J_{1b}, if a local-moment model is to describe the systems. This is similar to the large anisotropy found in CaFe$_2$As$_2$ [85]. Another clear finding from the fitting is that the damping term in the spectrum is

	S_{eff}	SJ_{1a} (meV)	SJ_{1b} (meV)	SJ_2 (meV)	SJ_c (meV)
$E \lesssim 100\,\text{meV}$ fits	0.30(1)	31(1)	−5(5)	21.7(4)	2.3(1)
$E \gtrsim 100\,\text{meV}$ fits	0.69(2)	39(2)	−5(5)	27.3(7)	2.3(fixed)

Table 4.1: Results of local-moment model fitting. Best-fit parameters to the local-moment J_{1a}–J_{1b}–J_2 linear spin-wave model are summarised here. The errors are given in brackets. SJ_c cannot be determined from cuts taken above the maximum of the dispersion along $(0, 0, L)$, found to be $\sim$53 meV. Hence, for high-energy fits SJ_c was fixed to the value determined from the low-energy fits.

energy dependent, with a steady increase at low energies followed by a rapid increase at about 80 meV.

The spin-wave model, however, fails in two important respects. First, the modelling was only successful by fitting low and high energies ($E \lesssim 100\,\text{meV}$ and $E \gtrsim 100\,\text{meV}$) separately — the low-energy parameter set is unable to account for the existence of an appreciable signal above $\sim$200 meV (Figs. 4.3(b) and 4.4(d)) while the high-energy parameters predict that the spin-wave branches below $\sim$150 meV are unresolved, which is inconsistent with the data in Fig. 4.3(a) and (c). Second, the high-temperature spectra are inconsistent with the tetragonal symmetry, which constrains $J_{1a} = J_{1b}$ for $T > T_{\text{N,s}}$. This is illustrated in Fig. 4.2(e), which shows that when $J_{1a} = J_{1b}$ the spin-wave spectrum is gapless at $(0.5, 0.5)$.

In the local-moment model, the origin of this softening at $(0.5, 0.5)$ is frustration of the nearest-neighbour interactions, consider Fig. 4.1(b) for $J_{1a} = J_{1b}$. When this condition is met, the magnetic structure can be regarded as two decoupled interpenetrating AFM sublattices, as illustrated in Fig. 4.5(a). The unit cell of these sublattices is the same as the tetragonal crystal structure unit cell. The magnetic unit cell of the sublattices, however, corresponds to the orthorhombic crystal structure unit cell (but with $a = b$), illustrated in Fig. 4.5(a). This is significant because the wavevectors X and M, marked in 4.5(b), are both magnetic zone centres for the uncoupled AFM sublattices, and therefore equivalent by symmetry. For the one-Fe lattice relevant to a itinerant electron description, however, X= $(0.5, 0)$ and M= $(0.5, 0.5)$ are not equivalent positions. This shows that the fact that the spin-wave energy goes to zero at $(0.5, 0.5)$ for the tetragonal structure is purely a property of the local-moment treatment of the magnetic interactions.

This raises the question of whether a mechanism exists that maintains an anisotropic exchange coupling ($J_{1a} \neq J_{1b}$) in the paramagnetic phase, or whether the local-moment model must be abandoned. One possible mechanism is nematic order, which has been proposed to explain anisotropy in the in-plane resistivity [88] and elastic properties [96] of some iron-based superconductors. In some cases the electronic nematic order is predicted to persist above $T_{\text{N,s}}$, but for only a few degrees at most [86]. Thus any evidence of broken symmetry above $T_{\text{N,s}}$ is unlikely to be due to nematic order, but could perhaps be ascribed to nematic-like fluctuations as discussed in Ref. [96]. The results presented here include measurements at 20 K above and $\sim$90 K above $T_{\text{N,s}}$, and,
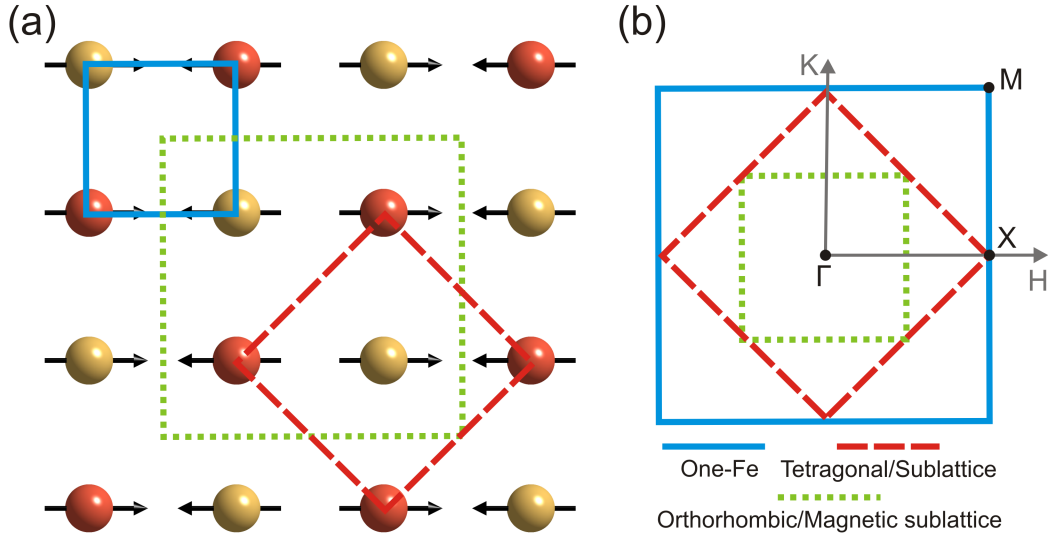
Figure 4.5: Magnetic structure and Brillouin Zones. (a) One layer of Fe in the a–b-plane, where arrows again represent the spin associated with iron ordering. The different coloured atoms denote the two decoupled sublattices for $J_{1a} = J_{1b}$ as described in the text. The solid blue square is the one-Fe unit cell. The dashed red square is the sublattice unit cell, and also corresponds to the tetragonal $I4/mmm$ crystal structure unit cell. The dotted green square is the unit cell of the magnetic order for the sublattices, and also corresponds to the orthorhombic $Fmmm$ crystal structure unit cell. (b) The first BZs of the different unit cells used to describe SrFe$_2$As$_2$. Significant positions in the BZ of the one-Fe BZ are marked with black dots and labelled.

as can be seen in Figs. 4.2(b) and (c) and Fig. 4.4, the neutron-scattering spectra are very similar. Although some change in the spectra might be expected over such a wide temperature range, the existence of nematic fluctuations cannot be completely ruled out.

It has been suggested that orbital ordering might explain the observed anisotropy [87]. In this case it has been predicted that a spin-wave mode would exist at high energies at $\boldsymbol{Q} = (0.5, 0.5)$. The same calculations also indicate that on warming the energy of this mode softens slightly, and the peak height of $\bar{S}(\boldsymbol{Q}, E)$ decreases rapidly. The lack of appreciable softening of the mode at $\boldsymbol{Q} = (0.5, 0.5)$ agrees with the data, however, as shown in Figs. 4.4(d)–(f), the peak intensity is essentially unchanged, at variance with the calculation.

If the local-moment model cannot be reconciled with the data, as appears likely, then what about itinerant electron models [94, 97], or hybrid models that combine both local moment and itinerant electrons [98]? In order to achieve a complete description of the data it is likely that a relatively detailed model will be required. A mean-field model based on a five-band structure appears to give quantitatively good agreement with some of the features observed here [94]. This is illustrated in Fig. 4.2(a), which shows the low-temperature INS data, and Fig. 4.2(f) which shows the calculated imaginary part of the susceptibility $\chi''(\boldsymbol{Q}, E)$, convolved with the instrument resolution. The locus of maximum intensity for the calculation is also plotted. This curve is more structured

than the smooth dispersion curves shown in Figs. 4.2(d) and (e), with several abrupt changes of gradient. This sort of behaviour is parametrised in a local-moment model by exchange constants that change with energy. The energy scale of the calculated $\chi''(\boldsymbol{Q}, E)$ has been changed by a factor of 0.85 compared to the published calculation. This rescaling is likely due to the fact that in a mean-field approximation the energy scale typically needs to be normalised down due to correlation effects not included in the model.

The fact that the model works reasonably well suggests that $SrFe_2As_2$ exhibits rather weak electron correlations. It is important to note that the calculations from Ref. [94] show that $\chi''(\boldsymbol{Q}, E)$ does not soften at $\boldsymbol{Q} = (0.5, 0.5)$ in the paramagnetic phase (Fig. 4.2(g)), which is in agreement with the data (Fig. 4.2(b)). However, the itinerant model does have some shortcomings, in particular the form of the scattering at low energies in the paramagnetic phase. The calculation yields a signal at an incommensurate wavevector, which is not seen in the data. Kaneshita and Tohyama [94] suggest that this arises from imperfect nesting of the Fermi surface, but is not reflected in the data due to finite temperature effects that are not included in their calculation. Thus, in order to obtain a better agreement between calculations and data, one would need to use a more detailed, experimentally-determined band structure, and also perhaps go beyond the mean-field approximation.

The key advantages of the itinerant model are thus that (i) it results in a more structured signal, (ii) it gives an explanation for the energy-dependent damping (§ 2.3.1), and (iii) no further phenomenological explanations are required to reproduce the signal at $\boldsymbol{Q} = (0.5, 0.5)$ in the paramagnetic phase.

As mentioned above, there have been proposals of hybrid models that combine both local moments and itinerant electrons [98]. In the SDW phase these calculations yield a structured dispersion with a high-energy mode at $\boldsymbol{Q} = (0.5, 0.5)$, as was observed here. It is not clear, however, how the spectra would change on heating above $T_{N,s}$, which is a crucial determinant between local-moment and itinerant models. Thus, further comment on this point is beyond the scope of this discussion.

4.6 Conclusions

The measurement of the magnetic dynamics in $SrFe_2As_2$ has been informative as to the nature of magnetism in this system, which is important in the wider context of superconductivity in the iron-based systems. The analysis shows that only a superficial explanation of the observed spin fluctuations at low temperatures can be achieved by a local-moment spin-wave model. Overall this model fails to replicate the data across the full energy range and for temperatures $T > T_{N,s}$. There are suggestions of additional modifications to a local-moment model, such as orbital and nematic effects, that might resolve these discrepancies. These models, however, require further development and would need to reproduce a wide range of experimental results in the iron-based systems before being generally accepted.

An itinerant model appears to offer a far better explanation of the data presented.

By measuring at both higher temperatures and higher energies than previously reported, I have been able to show that an appropriate model must explain the high-energy signal at $Q = (0.5, 0.5)$. Importantly, in the itinerant model it is not necessary to invoke further symmetry breaking to explain the lack of soft mode at this position.

These results provide a useful backdrop to the remaining chapters in this thesis. It is clear that strong magnetic fluctuations are present in the parent-phase of a superconducting family. At low energies these fluctuations appear at the wavevector $Q = Q_{\mathrm{SDW}} = (0.5, 0)$ that describes the magnetically ordered phase. The magnetic fluctuations appear to be best described by an itinerant model. While there is still debate about the true microscopic mechanism for magnetism in the iron-based superconductors, with many favouring a mixed itinerant plus local-moment model [25], a large itinerant effect is likely to be dominant in relation to the superconductivity. In the remainder of this thesis the discussion will focus on itinerant descriptions of the magnetism in iron-based superconductors, as was discussed in the introductory chapter (§ 2.5). This is justified by the evidence presented here and in subsequent work, which indicates that the model discussed in § 2.5–§ 2.6 captures the essential physics for understanding the link between magnetic fluctuations and superconductivity [9, 25, 47, 99].

Antiferromagnetic fluctuations in LiFeAs

Contents

5.1 Introduction

In the preceding chapter I showed that strong magnetic fluctuations are present in a parent phase of the iron-based superconductors. Here, I move on to investigate superconducting compounds, in which magnetic fluctuations appear to be of vital importance to the superconductivity (§ 2.3–§ 2.6). In this Chapter I discuss LiFeAs, which is a superconductor with $T_c \approx 17\,\text{K}$. I present results from an INS experiment to probe the spin fluctuations in LiFeAs at temperatures both above and below T_c.

LiFeAs exhibits several properties which apparently set it apart from the iron-based superconductors that were described in Chapter 2. Unlike other stoichiometric iron-arsenide compounds, LiFeAs is an intrinsic superconductor. It has a relatively high T_c without the need for carrier doping or application of pressure to induce superconductivity [100–103]. The superfluid stiffness, ρ_s, of LiFeAs is greater than in other iron-based superconductors, but both ρ_s and T_c decrease upon doping [104]. Accordingly, and again in contrast to other iron-based superconductors, no structural or magnetic phase transitions have been observed in stoichiometric LiFeAs. Contrary to some theoretical predictions [105–107], it does not undergo a tetragonal-to-orthorhombic phase transition, even up to pressures of $20\,\text{GPa}$ [108, 109], nor does it exhibit SDW order close to, or coexisting with, the superconducting regime [100, 103, 110]. These anomalous characteristics raise the possibility that some aspects of the superconductivity in LiFeAs may be different from the other iron-based superconductors.

The absence of SDW order in LiFeAs has been discussed in relation to its Fermi surface [111–113]. As described in § 2.5, SDW order in the iron-based superconductors has often been attributed to Fermi surface nesting between electron and hole pockets separated by the AFM wavevector $\mathbf{Q}_{\text{SDW}}$ (Fig. 2.6). In superconducting compounds where SDW order is suppressed or completely absent, AFM fluctuations persist and the magnetic resonance feature appears in the INS spectrum at the wavevector $(0.5, 0)$ at temperatures below T_c. This feature is consistent with a dominant spin-singlet $s_{\pm}$ pairing symmetry (§ 2.6).

ARPES studies, however, found that the Fermi surface of LiFeAs displays poor nesting properties [111]. The hole pockets at $(0, 0)$ are unusually shallow, as shown in Fig. 5.1. In Fig. 5.1(a) the hole pockets are visible centred on the Γ-point, which is $(0, 0)$ in both one-Fe and tetragonal unit cell notation. The outer pocket is larger and flatter than in other iron-based superconductors — compare to Fig. 2.6, in which only one hole pocket is illustrated for clarity — whereas the inner hole pockets are smaller (see the solid black lines in Fig. 5.1(a)[1]). Figure 5.1(c) shows that the small hole pocket creates a flat maximum at the Fermi energy. The electron bands can be seen in Fig. 5.1(a) centred on the M-point, which is the $(0.5, 0)$ point in one-Fe cell notation. None of the hole pockets are well nested with the electron pockets.

The ARPES results suggest that differences between the physical properties of LiFeAs and other iron-based superconductors could be due to differences in the electronic structure. An electronic structure model for LiFeAs based on the ARPES results

---

[1] The apparent 'butterfly' shape of the pockets near the Γ-point in the data in Fig. 5.1(a) is explained in the details of the experiment, see Ref. [111].
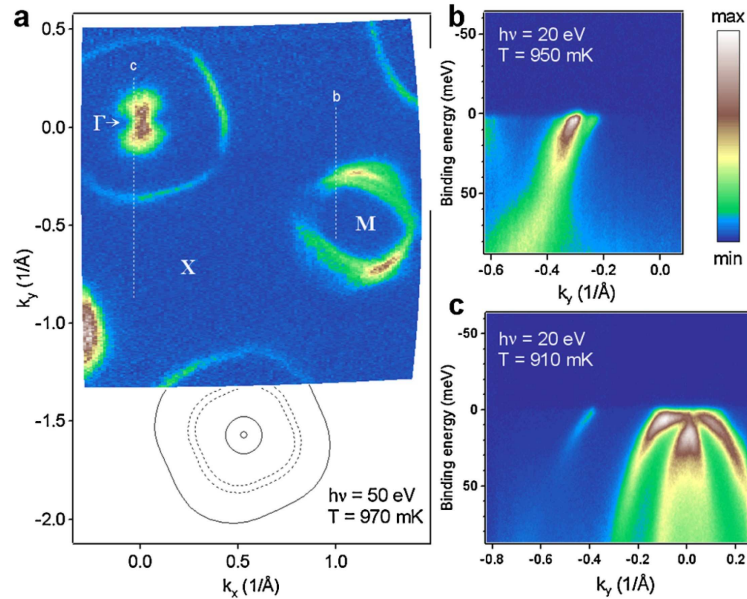
Figure 5.1: Fermi surface of LiFeAs. Results of ARPES measurement on LiFeAs [111], represented in the tetragonal unit cell of the LiFeAs crystal structure (see Figs. 5.2 and 2.2). (a) Photoemission intensity integrated in range of 5 meV around the Fermi level. Solid black lines represent $(0,0)$-centred Fermi contours, dashed lines represent the most pronounced Fermi contours centred on the $(0.5, 0.5)$ point, which is equivalent to $(0.5, 0)$ in the one-Fe unit cell. (b) and (c) Momentum-energy cuts along the vertical directions marked by the white dashed lines in panel (a). Reprinted figure with permission from S. V. Borisenko *et al.*, Phys. Rev. Lett., **105**, 067002, 2010 [111]. Copyright (2010) by the American Physical Society.

supports this notion [113]. The calculations based on a 3-band model find that SDW order is absent, and instead predict FM or 'almost' FM fluctuations, i.e. fluctuations either with $\boldsymbol{Q} = (0,0)$, or with an incommensurate wavevector close to $(0,0)$. Brydon *et al.* [113] find that these fluctuations drive an instability towards spin-triplet superconductivity — i.e. that superconducting electrons pair with their spins aligned in parallel. Consequently, to satisfy the Pauli exclusion principle in this model, the superconducting gap symmetry cannot be *s*-wave, but instead could be *p*-wave. The character of the spin fluctuations will reflect the pairing symmetry and is thus pivotal to the superconducting pairing state, according to these models. Experimental measurements of the spin fluctuation spectrum of LiFeAs are therefore of great interest.

Here I report an INS study of the momentum-resolved magnetic spectrum of polycrystalline superconducting LiFeAs. I aim to answer the questions (i) what is the character of the magnetic fluctuations in LiFeAs, if any exist, and (ii) is there a signal consistent with the magnetic resonance that is observed in many other iron-based superconductors? The INS measurements probed a large area of (Q, E)-space, up to energies of ~ 30 meV, for a range of temperatures crossing T_c. A strong magnetic signal was observed at wavevector $Q = 1.18\,\text{Å}^{-1}$, which is consistent with $\boldsymbol{Q}_{\text{SDW}}$, and the strength of the scattering increases upon cooling below T_c. I will comment on the
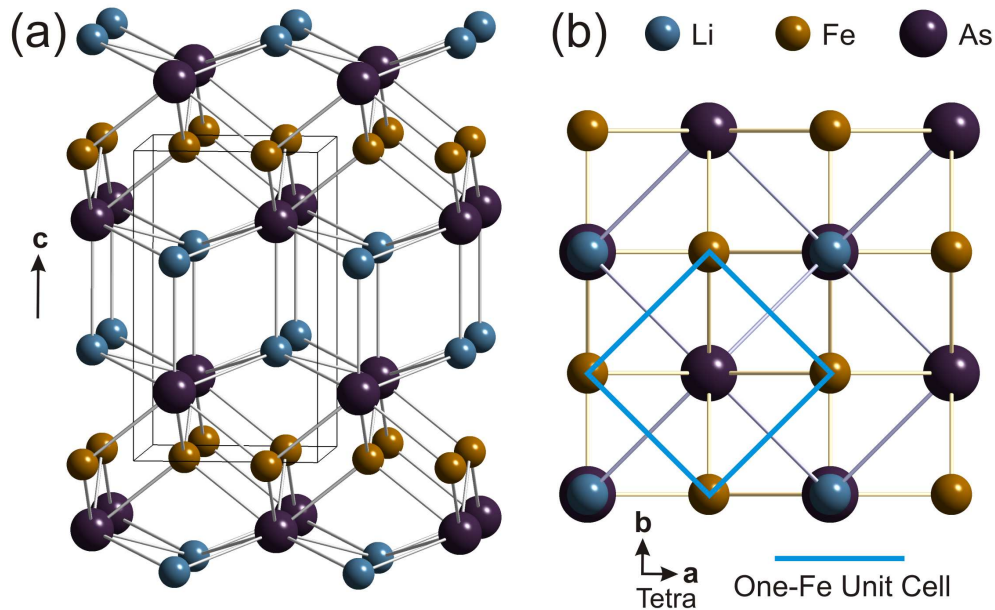
Figure 5.2: Crystal structure of LiFeAs. (a) The structure of LiFeAs, which crystallises in space group $P4/nmm$, with one tetragonal unit cell marked by the black lines. (b) A projection onto the a–b-plane, with the in-plane one-Fe unit cell marked.

implications of these results for the theoretical prediction of triplet superconductivity, and discuss what they reveal about the relationship of LiFeAs with other iron-based superconductors.

The results presented in this chapter have been published in Ref. [114].

5.2 Synthesis and characterisation

At the time of the experiment single crystals of LiFeAs were not available, so a powder sample was prepared. The sample used for this experiment was prepared by Michael J. Pitcher of the Inorganic Chemistry Laboratory, University of Oxford, UK, following a ceramic synthesis route similar to that described in §3.1. The polycrystalline LiFeAs was prepared from high-purity elemental reagents ($>99.9\,\%$); the method is described in detail in Ref. [104]. The sample 'MP127' discussed in Ref. [104] was used for the experiment reported here.

The crystal structure of LiFeAs is shown in Fig. 5.2. It has tetragonal symmetry with space group $P4/nmm$, and lattice parameters $a = b = 3.777\,\text{Å}$ and $c = 6.356\,\text{Å}$. In some samples that nominally consist of LiFeAs, substitution of Li by Fe has been shown to destroy superconductivity even at the $2\,\%$ level [104]. Joint synchrotron XRPD (see Fig. 5.3(a)) and neutron powder diffraction refinements against data from the sample established that the material was phase pure and that there was no detectable substitution of Li by Fe. Magnetic susceptibility measurements made by SQUID magnetometry confirmed a sharp onset of superconductivity at $T_{\text{c}} = 17\,\text{K}$, as illustrated in
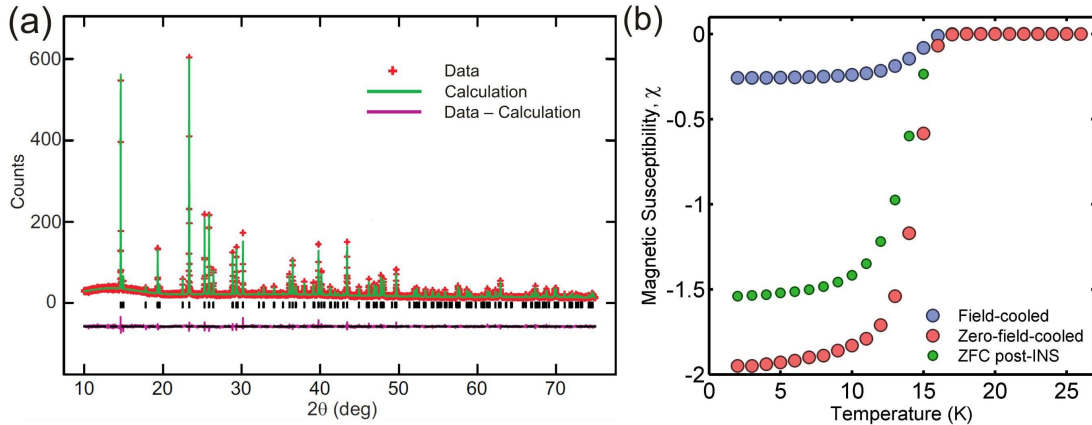
Figure 5.3: Characterisation of LiFeAs. (a) Rietveld refinement of XRPD data collected on instrument I11 at Diamond Light Source by M. J. Pitcher, showing that the sample is phase pure with lattice parameters $a = 3.77657(1)$ Å, and $c = 6.35527(2)$ Å corresponding to stoichiometric LiFeAs [104]. Adapted from Ref. [114]. (b) The magnetic susceptibility of portions of the sample measured before the neutron scattering experiment (blue and pink symbols), and after the experiment (green symbols). The measurements were made in an applied field of 50 Oe under zero-field-cooled (ZFC) and field-cooled (FC) conditions as indicated.

Fig. 5.3(b).

5.3 Experimental set-up

The INS experiments were performed on the MERLIN chopper spectrometer at the ISIS Facility (§ 3.5). Approximately 7.5 g of LiFeAs powder was sealed inside a cylindrical aluminium can and mounted in a top-loading closed-cycle refrigerator (§ 3.5.6). Due to the extreme air sensitivity of the sample, care was taken to ensure all handling was done in an inert atmosphere. After the experiment the sample was rechecked by XRPD and magnetometry and its properties were found to be the same as before the experiment. Figure 5.3(b) illustrates a clear downturn in the ZFC susceptibility measured after the experiment, indicating that T_c is unchanged. The small difference in absolute magnitude is not unexpected given the competing effects discussed in § 3.2.2. Spectra were recorded with incident neutron energies $E_i = 15$, 25 and 50 meV and Fermi chopper frequencies of 150, 150 and 200 Hz, respectively. These set-ups resulted in energy resolutions of 1.1 meV, 2.1 meV and 4.4 meV on the elastic line, estimated from the FWHM of the incoherent scattering. Measurements were recorded at the following temperatures: $T = 6$, 7.5, 10.5, 12, 15, 20, 25.6, 30.9 and 34 K. The scattering from a standard vanadium sample was used to normalise the spectra, as described in § 3.5.5, where here the units mb sr^{-1} meV^{-1} f.u.$^{-1}$ refer to the f.u. LiFeAs.
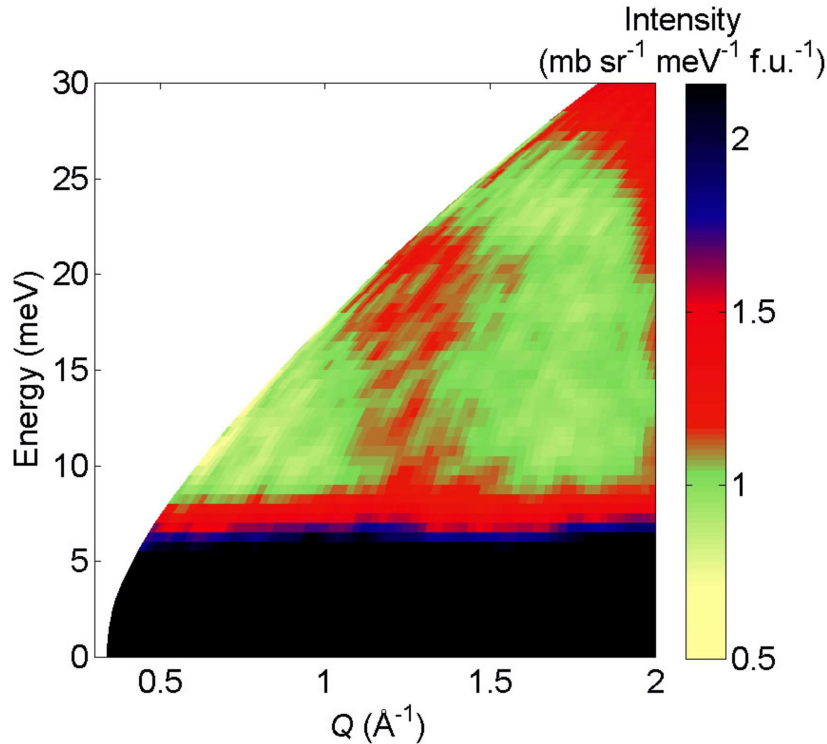
Figure 5.4: INS spectrum from LiFeAs. Neutron scattering spectrum of polycrystalline LiFeAs. The data were recorded on MERLIN at a temperature of 6 K with an incident neutron energy of 50 meV. Reprinted figure from A. E. Taylor *et al.*, Phys. Rev. B, **83**, 220514(R), 2011 [114]. Copyright (2011) by the American Physical Society.

5.4 Results

The general features of the data are illustrated in Fig. 5.4, which is a colour plot of the measured inelastic scattering intensity as a function of momentum transfer and energy transfer. Because a polycrystalline sample was measured, as opposed to a single crystal, only the magnitude of the momentum transfer is known (§ 3.5.4). At low energies there is strong scattering from the elastic line (which includes both coherent and incoherent scattering) and from phonons. However, a vertical column of scattering centred on $Q \approx 1.2 \, \text{Å}^{-1}$ stands out from the phonon background and extends in energy throughout the accessible region of (Q, E)-space. The spectrum bears a close resemblance to that of polycrystalline $BaFe_2As_2$ [38], $Ba_{1-x}K_xFe_2As_2$ [40] and LaFeAsO [39], and based on this the column of scattering at $Q \approx 1.2 \, \text{Å}^{-1}$ can be confidently attributed to magnetic fluctuations close to Q_{SDW}.

Figure 5.5 presents a selection of cuts taken through the data at different energies. The cuts all contain a rising signal at higher Q due to phonon scattering and — at all but the lowest energy — a peak centred on $Q \approx 1.2 \, \text{Å}^{-1}$. To analyse the peak quantitatively I fitted the cuts to a Gaussian function on a linear background using a least-squares fitting routine [115]. Initial fits were made in which the width, centre, and amplitude of the Gaussian, and the slope and intercept of the linear background, were
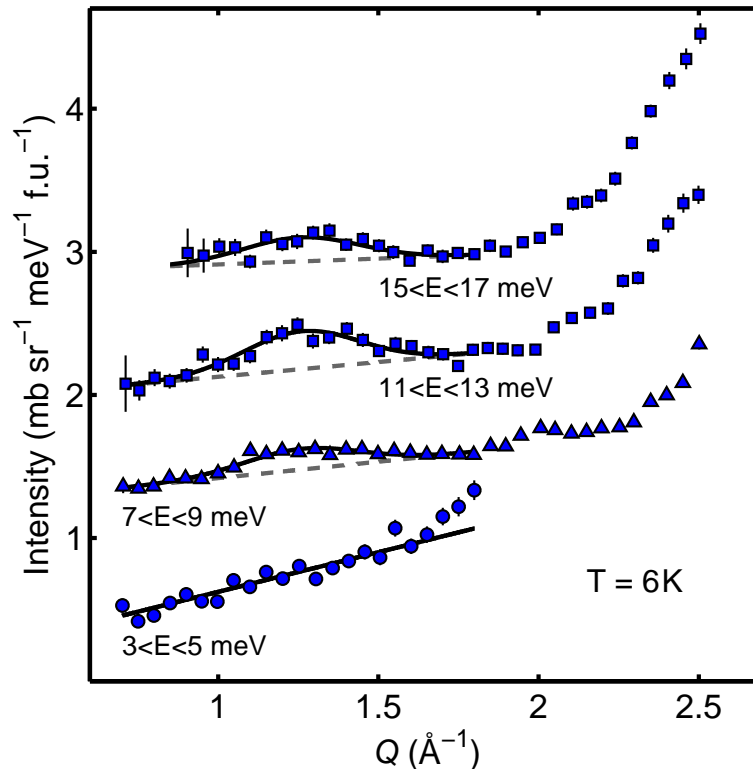
Figure 5.5: Constant-energy cuts. Constant-energy cuts showing the magnetic signal at $Q \approx 1.2\,\text{Å}^{-1}$ at different energies for a fixed temperature of 6 K. Data were averaged over the indicated energy intervals. Successive cuts are displaced vertically for clarity. The symbols represent different neutron incident energies: squares $E_i = 50\,\text{meV}$, triangles $E_i = 25\,\text{meV}$, circles $E_i = 15\,\text{meV}$. The full lines are fits to Gaussian peaks centred at $Q = 1.24\,\text{Å}^{-1}$ with standard deviation $0.18\,\text{Å}^{-1}$ on a linear background (broken lines).

allowed to vary. The peak centre and width were found not to vary significantly with energy or temperature, with average values $Q = 1.24 \pm 0.02\,\text{Å}^{-1}$ and $\sigma = 0.18 \pm 0.02\,\text{Å}^{-1}$, respectively. For all subsequent fits I fixed the centre and width of the Gaussian to these values. This is physically reasonable because the magnetic interactions are strong and the dispersion very steep (see Fig. 5.4) as found in other iron-based superconductors [24]. In most cases these constraints do not significantly affect the values of the fitted intensities, but at the lowest energies where the signal is small, and at the highest energies where there is limited data on the background on the low-Q side of the peak, they reduce the uncertainties in the fitted peak intensities.

I also performed fits with a powder-averaged 2D Gaussian function, described in § 3.5.4, a model that assumes no variation of intensity with out-of-plane momentum or with energy. This method put the centre of the 2D Gaussian at $Q = 1.14 \pm 0.02\,\text{Å}^{-1}$. In reality the magnetic correlations are expected to be quasi-2D (i.e. intermediate between 2D and 3D due to non-negligible c-axis coupling, as observed in other iron arsenides [24]). This means the true characteristic wavevector of the fluctuations is expected to be in the range $Q = 1.14 - 1.24\,\text{Å}^{-1}$, consistent with the AFM wavevector
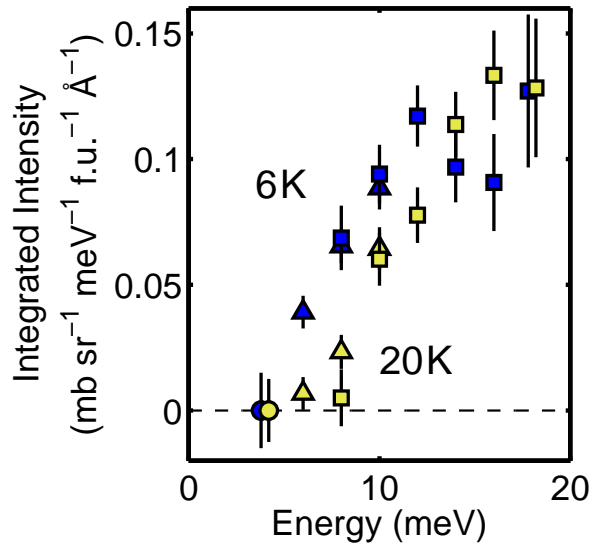
Figure 5.6: Energy dependence of signal. The integrated intensities of fitted Gaussian peaks (like those in Fig. 5.5) as a function of energy for temperatures of 6 K (blue) and 20 K (yellow). The 6 K and 20 K points at 4 meV and 18 meV are in reality almost coincident, but have been separated horizontally by 0.5 meV to make them visible. The symbols represent different neutron incident energies: squares $E_i = 50$ meV, triangles $E_i = 25$ meV, circles $E_i = 15$ meV.

$\boldsymbol{Q}_{\mathrm{SDW}} = (0.5, 0, L)$, which has magnitude $Q_{\mathrm{SDW}} = 1.18\,\text{Å}^{-1}$ for $L = 0$.

Figure 5.6 presents a plot of the integrated intensities of the fitted Gaussian peak as a function of energy for the accessible range of energies. The integrated intensity is a measure of the spectral weight of the fluctuations centred at $Q \approx 1.2\,\text{Å}^{-1}$. Data are shown for temperatures of 6 K $(T < T_{\mathrm{c}})$ and 20 K $(T > T_{\mathrm{c}})$. At 20 K there is no measurable intensity up to an energy of about 5 meV, at which point the intensity increases sharply with energy. This could indicate that there is a spin gap in the normal state of up to ~10 meV. At 6 K there is additional intensity in the energy range between about 4 meV and 12 meV.

Figure 5.7 shows a series of cuts taken through data collected at different temperatures. All these data are from measurements with $E_i = 25$ meV, and the cuts are averaged over an energy interval of 6–11 meV. Small peaks visible near $Q \approx 2\,\text{Å}^{-1}$ are from phonons since they increase with temperature. I used the same fitting procedure as described above to obtain the temperature variation of the magnetic signal. Again, the centre and width of the Gaussian were fixed, and only the peak amplitude and linear background were varied. Examples of the Gaussian fits are shown as solid lines in Fig. 5.7. The signal is visible above the non-magnetic background (dashed lines) at all temperatures, but appears to be larger for $T = 6$ and 12 K, i.e. $T < T_{\mathrm{c}}$. To begin to address the question of whether the signal is consistent with a magnetic resonance feature, the temperature dependence is assessed quantitatively as shown in Fig. 5.8. This figure shows the integrated intensity of the fitted Gaussian peak as a function of temperature. The integrated intensity increases sharply below the superconducting
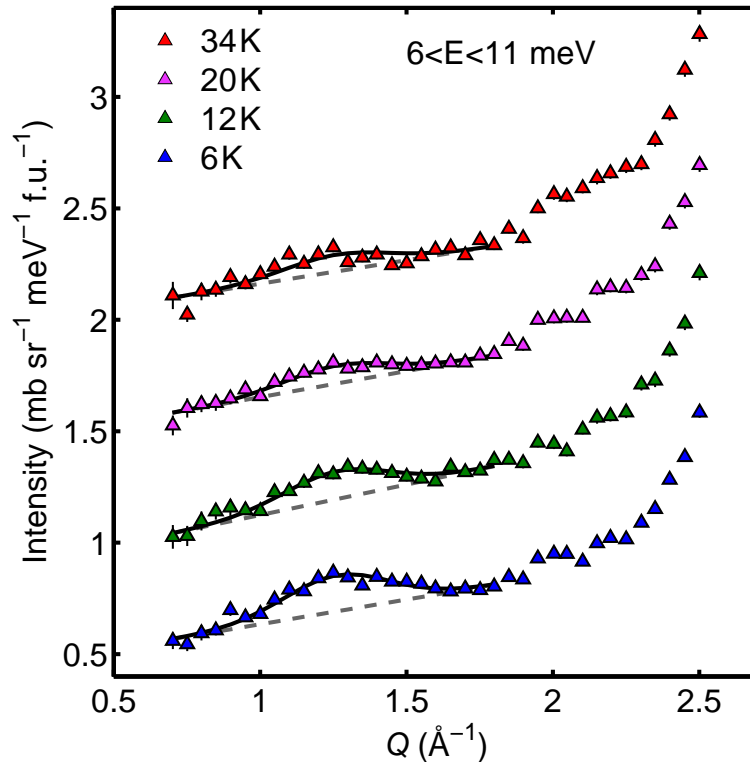
Figure 5.7: Temperature dependence of cuts. Constant-energy cuts showing the temperature dependence of the magnetic signal at $Q \approx 1.2\,\text{Å}^{-1}$. Data in each cut were recorded with an incident energy $E_\text{i} = 25\,\text{meV}$ and have been averaged over an energy range 6–11 meV. Successive cuts are displaced vertically for clarity. Full lines are fits to Gaussian peaks centred at $Q = 1.24\,\text{Å}^{-1}$ on a linear background (broken lines).

transition temperature $T_\text{c} = 17\,\text{K}$.

5.5 Discussion

The measurements I have reported here reveal two pieces of new information about LiFeAs. The first is that cooperative spin fluctuations exist and have a characteristic wavevector close to $Q_\text{SDW} = 1.18\,\text{Å}^{-1}$. The data indicate that LiFeAs has similar spatial magnetic correlations to those in other iron-arsenide superconductors. The absolute values of the integrated intensity shown in Fig. 5.6 are comparable to those obtained for $BaFe_2As_2$ by the same technique [38], which suggests that the size of the fluctuating moments are similar in the two materials.

At the same time I find no evidence for near-FM fluctuations, which would result in strong scattering at FM wavevectors. The closest FM wavevectors to the observed magnetic signal are $Q_{(001)} = 0.99\,\text{Å}^{-1}$ and $Q_{(002)} = 1.98\,\text{Å}^{-1}$. It is evident from Figs. 5.4, 5.5, and 5.7 that no detectable magnetic signals exist at these positions. The direct observation of SDW fluctuations, as opposed to FM fluctuations, in the momentum-resolved magnetic spectrum is consistent with the interpretation of nuclear magnetic
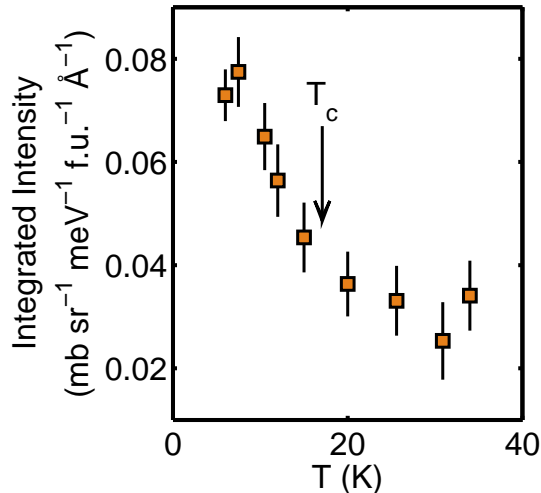
Figure 5.8: Temperature dependence of signal. The integrated intensities of Gaussian peaks fitted to $6 < E < 11\,\text{meV}$ cuts (like those in Fig. 5.7) as a function of temperature. The arrow marks the T_c of LiFeAs.

resonance (NMR) [116–118], and muon spin rotation (μSR) [110] data suggesting that LiFeAs is close to a magnetic instability.

The existence of strong SDW fluctuations, and lack of FM fluctuations, is perhaps surprising given (i) the results from ARPES which indicate poor nesting between electron and hole pockets separated by $\boldsymbol{Q}_{\text{SDW}}$ [111] (Fig. 5.1), and (ii) the theoretical calculations based on those results which predict near-FM fluctuations to be the dominant pairing interaction [113]. It is probable, therefore, that nesting is not an essential feature of the Fermi surface providing the driving mechanism for the magnetic fluctuations. This conclusion is supported by more detailed calculations that were performed using a functional renormalisation group method, subsequent to the publication of the work presented in this chapter [119]. These calculations indicate that although FM fluctuations are present as a competing instability, AFM fluctuations dominate at the low energy scales relevant for superconductivity and could drive an instability towards $s_\pm$ superconducting pairing in LiFeAs. This is supported by recent experimental evidence that FM correlations develop at $T \gtrsim 100\,\text{K}$ only in Li-deficient (non-superconducting) samples [120]. The calculation is also consistent with experiments which found that the magnetic penetration depth [121] and anisotropy of the upper critical field H_{c2} [122] in superconducting LiFeAs are consistent with $s_\pm$ models.

The second notable feature of the results is the increase in spectral weight on cooling below $T \approx T_c$ at low energies (Figs. 5.6 and 5.8). This behaviour is qualitatively consistent with a superconductivity-induced magnetic resonance, as reported in the $X\text{Fe}_2\text{As}_2$, $\text{FeSe}_{1-x}\text{Te}_x$ and LaFeAsO systems, see Chapter 2. Recalling the approximate scaling between the resonance energy and T_c (§ 2.4), $E_r/k_B T_c \approx 5$, a magnetic resonance is predicted near $7.5\,\text{meV}$ for LiFeAs. This is in the middle of the range in which additional scattering intensity is observed below T_c (see Fig. 5.6). On balance, therefore, the results point towards the existence of a magnetic resonance below T_c in LiFeAs.

Subsequent to the work presented here, small single crystals of LiFeAs became available, and the results of INS experiments on both superconducting LiFeAs [45] and non-superconducting $Li_{1-x}FeAs$ [123] crystals were published. These results confirmed the presence of magnetic fluctuations close to $(0.5, 0)$, but Qureshi *et al.* [45] found that the magnetic INS signal in superconducting LiFeAs originates from an incommensurate wavevector, $(0.5, \pm 0.07)$. As discussed in § 3.5.4, due to the limitations of a powder measurement it is not possible to determine the precise position in reciprocal space from which the magnetic fluctuations originate in polycrystalline LiFeAs. $|(0.5, \pm 0.07)| = 1.19 \, \text{\AA}^{-1}$ is consistent with the results reported in this chapter. It is not possible to resolve an incommensurate splitting of this size after powder-averaging.

In light of Qureshi *et al.*'s [45] finding of an incommensurate wavevector, Knolle *et al.* [124] performed further ARPES experiments to determine the detailed structure of the electron and hole pockets centred around $(0.5, 0)$ and $(0, 0)$, respectively. They found that the incommensurate wavevector $(0.5, \pm 0.07)$ observed in their INS experiment is consistent with the separation of the electron and hole pockets. Quantum oscillation experiments were also interpreted as implying that the electron and hole pockets are 'almost nested' in a superconducting sample of LiFeAs [125]. This implies that the interpretation of the resonance in terms of the BCS coherence factor, as discussed in § 2.5, holds for LiFeAs, and therefore explains the evidence of a resonance in polycrystalline LiFeAs presented here.

The results from single crystal INS experiments also reveal more about the size of the spin gap in LiFeAs. For $T < T_c$, to within experimental error, I found no signal from magnetic scattering in the energy range $3 < E < 5 \, \text{meV}$ (see Fig. 5.6) but found an appreciable signal at higher energies. This is consistent with the INS results on the superconducting single crystal [45], which indicate a suppression of magnetic scattering below $\sim 5 \, \text{meV}$ for $T < T_c$ and showed increased scattering in the energy range 6–10 meV. However, the results are not consistent for $T > T_c$. Qureshi *et al.* [45] found increased scattering intensity at low energies in the normal state. This is at odds with the observation here of zero magnetic scattering intensity to within experimental error at low energies for $T > T_c$ (Fig. 5.6). In the non-superconducting sample of $Li_{1-x}FeAs$ measured by Wang *et al.* [123] a spin gap of $\sim 13 \, \text{meV}$ was found. It is possible that all three samples have different normal state spin gaps, which could be explained by slight differences in each of their electronic structures. If the polycrystalline sample had a normal-state spin gap, Δ_n, that satisfied $\Delta_n > E_r$, then for $T < T_c$ spin fluctuations would appear in the INS spectrum at an energy less than Δ_n, consistent with the data. It is also possible that the simple modelling of the non-magnetic scattering I used does not properly account for the powder-averaged phonon scattering, and therefore masks some magnetic scattering in the data. Unfortunately, Fermi surface measurements that would help to clarify this point are not possible on a polycrystalline sample.

5.6 Conclusions

I have reported results that provide firm evidence that LiFeAs behaves in a similar way to other iron-based superconductors and is not in fact anomalous. Measurement of the scattering response of LiFeAs provided clear evidence for strong magnetic fluctuations with a characteristic wavevector close to Q_{SDW}. The analysis has shown that the data do not support a theoretical prediction of spin-triplet p-wave superconductivity [113], which would have resulted from a dominant FM instability. In the case of triplet superconductivity, strong scattering from FM fluctuations would be expected, but no such signal was found. Instead the results show that the magnetic fluctuations in LiFeAs are consistent with $\boldsymbol{Q}_{\mathrm{SDW}}$, and appear at energies in the region $\sim 5k_{\mathrm{B}}T_{\mathrm{c}}$, similar to other iron-based superconductors.

At low energies the intensity of the magnetic scattering increases upon cooling below T_{c}. This indicates that the signal is consistent with a superconductivity-induced magnetic resonance, which suggests that the resonance is common across the iron-based superconductors despite the poor Fermi surface nesting properties in LiFeAs [111]. This might appear to contradict the discussion of the resonance presented in § 2.5. However, more detailed ARPES measurements and calculations [124] found that the LiFeAs Fermi surface could still drive SDW-type fluctuations and produce a resonance at an incommensurate wavevector $\boldsymbol{Q} = (0.5, \delta)$. This interpretation explains single crystal measurements of LiFeAs, which found $\delta = 0.07$ [45], and is consistent with the results presented in this chapter.

The results show that, despite the absence of SDW order in the system, fluctuations at wavevector $Q = Q_{\mathrm{SDW}} = |(0.5, 0)|$ persist in LiFeAs. The poorly nested hole and electron pockets centred around $(0, 0)$ and $(0.5, 0)$, respectively, appear to be sufficient for the BCS coherence factor (Eq. 2.1) to drive an enhancement in the susceptibility $\chi(\boldsymbol{Q}, E)$ below T_{c}, as discussed in § 2.5. The results suggest that the mechanism for superconductivity in LiFeAs is similar to that in other iron-based superconductors, with magnetism intimately connected to superconductivity.

Inelastic neutron scattering from iron phosphides

Contents

Figure 6.1: Crystal structures of LaFePO and Sr_2ScO_3FeP. The structures of (a) LaFePO and (b) Sr_2ScO_3FeP are shown, indicating the tetrahedrally coordinated iron–phosphorus layers and the blocking layers stacked along the c-axis. Both crystal structures are described by tetragonal space group $P4/nmm$.

6.1 Introduction

In this chapter I present results from experiments on two iron-phosphide-based materials, as opposed to the iron-arsenide compounds discussed in the previous two chapters. I have investigated two families of superconductors, LaFePO and Sr_2ScO_3FeP. Both of these have iron-pnictide layers similar to those found in iron-arsenide systems, but with arsenic replaced by phosphorus, as illustrated in Fig. 6.1 (compare to Fig. 2.1). As mentioned in Chapter 2, superconductivity in iron-based systems was first discovered in LaFePO in 2006, with $T_c \approx 4\,\mathrm{K}$ [126]. However, because of its relatively low T_c, it was not recognised as the discovery of a new class of superconductors. Since the discovery of $LaFeAsO_{1-x}F_x$ [14] there has been heightened interest in LaFePO. Despite this, up to now no measurements of the momentum-resolved spin dynamics in the phosphide systems have been made.

Notwithstanding the structural similarity and the observation of superconductivity, the iron-phosphide systems differ in several respects from their arsenide counterparts. They generally have lower T_cs, they have lower resistivity in the normal state, and they do not undergo magnetic or structural phase transitions [126–130]. Evidence has been
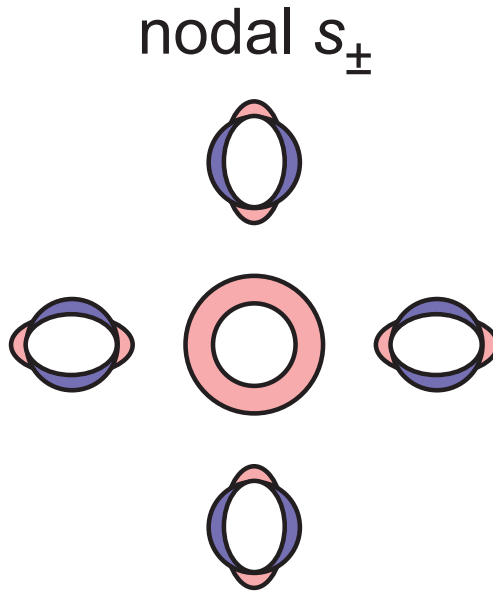
nodal $s_\pm$

Figure 6.2: Nodal gap structure. Schematic representation of the in-plane component for a nodal $s_\pm$ gap symmetry. The different colours represent opposite signs of the gap. Adapted from Ref. [58].

found for a nodal superconducting order parameter (Fig. 6.2) in LaFePO [131–133], Sr_2ScO_3FeP [134] and LiFeP [135], in contrast to many iron-arsenide and iron-selenide superconductors.

For the nodal $s_\pm$ gap structure the gap function crosses zero at points on the electron Fermi surface (see Fig. 6.2). Therefore, there are small portions of the electron pocket on which the gap has opposite sign to the gap on the rest of the electron pocket. Considering the theoretical treatment in § 2.5 and § 2.6, this has implications for the spin fluctuations in the systems. The direct wavevector $\boldsymbol{Q}_{SDW}$ now connects portions of the Fermi surface with the same sign of the gap, compare Fig. 2.6 and Fig. 2.7 with Fig. 6.2. Consequently, for a nodal $s_\pm$ gap symmetry the BCS coherence factor will tend to zero (Eq. 2.2) for scattering between the portions of Fermi surface separated by $\boldsymbol{Q}_{SDW}$. This does not, however, mean that no magnetic resonance feature will appear in the INS spectrum of a nodal superconductor. The sign-changed portion of the Fermi surface is small, and wavevectors $\approx \boldsymbol{Q}_{SDW}$ still connect sections of Fermi surface which have opposite sign of the gap. Calculations by Maier *et al.* [136] based on a 5-band model found that for a nodal $s_\pm$ state a resonance would still appear in the INS spectrum, although would be broader in $\boldsymbol{Q}$ than the signal calculated for a nodeless $s_\pm$ model. A resonance has, in fact, been observed at $Q \approx Q_{SDW}$ in INS data from polycrystalline $BaFe_2(As_{0.65}P_{0.35})_2$, which is a nodal superconductor with $T_c = 30\,\mathrm{K}$ [137].

As far as experimental indications of spin fluctuations in the phosphides are concerned there is conflicting evidence. Optical and charge transport studies have concluded that electron correlations are significantly weaker in the phosphides than in the arsenides [138, 139], whereas measurements of the Fermi surface indicate that corre-

lations could be of similar strength in the two systems [51]. Furthermore, evidence of spin correlations in phosphides has been reported in NMR and μSR studies [140, 141].

The differences between the systems raise the possibility that the pairing mechanism in the iron phosphides might not be the same as that in the higher-T_c iron-based superconductors. In particular, the role of magnetic fluctuations in the pairing mechanism of the iron phosphides remains unresolved, and this provides a strong incentive to obtain experimental information on the momentum-resolved magnetic fluctuation spectrum. Here I present results of INS measurements designed to search for magnetic fluctuations in LaFePO and Sr_2ScO_3FeP. Despite LaFePO's relatively low T_c of 4.5 K, it is of interest because of evidence that it might be close to an SDW instability driven by Fermi surface nesting [51, 142]. Sr_2ScO_3FeP is of interest because it was reported to show the highest $T_c (\approx 17 \, \text{K})$ among the known phosphide superconductors [128].

In this Chapter I set out to answer the question: are magnetic fluctuations present in the INS spectrum of iron-phosphide materials, like those that are observed in many other iron-based superconductors? The INS measurements probed a large area of (Q, E)-space, with E in the range from 0.5 to 20 meV. In the analysis I pay particular attention to $Q \sim 1.2 \, \text{Å}^{-1}$ that corresponds to the wavevector Q_{SDW}. Despite having performed careful measurements above and below T_c, no signal attributable to magnetic fluctuations is found in either system. I discuss what these results imply about the relative importance of magnetic fluctuations for superconductivity in the iron-phosphide systems, compared to other iron-based superconductors.

The results presented in this chapter have been published in Ref. [143].

6.2   Synthesis

At present large single crystals of iron phosphides are not available, so I undertook synthesis of polycrystalline samples of LaFePO and Sr_2ScO_3FeP for the experiments. I also prepared a sample of LaZnPO, a structural analogue of LaFePO that contains no magnetic ions, to use for a non-magnetic background comparison. I prepared the samples following the principles of the solid-state ceramic method described in § 3.1. I describe the details of the synthesis for each compound below.

6.2.1   LaFePO

High-quality LaFePO has previously been prepared by solid-state synthesis, and is generally found to be a good superconductor with an estimated volume fraction of ~20 % [126, 144]. Although McQueen *et al.* [127] reported that stoichiometric LaFePO is non-superconducting, this goes against the majority of the literature, and is likely due to their precise synthesis conditions and resulting stoichiometry. I prepared LaFePO by a method based on a combination of the reaction routes reported by Kamihara *et al.* [126] and McQueen *et al.* [127].

I first prepared the starting materials La_2O_3, La and P. La_2O_3 powder was prepared by dehydrating commercial powder (Alfa 99.99 %) at 600 °C for 10 hours. This ensures that any absorbed moisture is removed before use, and can be checked by x-ray

diffraction. I prepared fresh La metal filings from lumps of La (Alfa 99.9 %), after first filling off the tarnished surface of the metal lumps. Powdered phosphorus was prepared by grinding lumps of red P (Alfa 99.9999 %) with a pestle and mortar. I then mixed La, P and commercial Fe powder (Alfa 99.998 %) in the ratio 1:3:3 and placed them in an alumina crucible in an evacuated silica ampoule. The elements were heated at $0.5 \,°C/min$ to $700 \,°C$ and held for ~12 hours to produce a stoichiometric mixture of the compounds LaP, FeP and Fe_2P. This mixture and La_2O_3 were then ground together to a very fine powder — I found this process to be strongly linked to sample quality, so I ground each batch of material (~2.5 g) for 3 hours to ensure minimal amounts of impurity in the final product. This fine powder was then placed in an alumina crucible; another crucible containing a LaFePO getter (synthesised in a similar way) was placed on top.[1] This was all sealed in a silica ampoule under $200 \,mbar$ of high-purity argon gas (rather than vacuum) in order to prevent collapse of the silica upon heating at close to the softening temperature of silica. This was heated at $1 \,°C/min$ to $1250 \,°C$ and held for 24 hours. The final product was removed and ground to a fine powder.

6.2.2   LaZnPO

I prepared LaZnPO following the route described by Kayanuma *et al.* [145]. Fresh La metal filings and red P powder, as above, were placed in an alumina crucible and sealed in a silica ampoule. This was heated to $700 \,°C$ and held for 10 hours to produce a stoichiometric mixture of LaP. The LaP mixture was ground together with commercial ZnO (Alfa 99.99 %) powder, and then pressed into a pellet before being sealed inside silica. This was heated at $2 \,°C/min$ to $1000 \,°C$ and held for 10 hours.

6.2.3 Sr_2ScO_3FeP

Sr_2ScO_3FeP was reported to be a superconductor at $17 \,K$ by Ogino *et al.* [128], but their synthesis resulted in a compound with a 9:1 ratio of Sr_2ScO_3FeP to a secondary phase $SrFe_2P_2$ (which is non-superconducting to $1.8 \,K$ [146]). I synthesised Sr_2ScO_3FeP by devising a slightly modified route.

To ensure high-purity unoxidised Sr metal, commercial Sr (Aldrich 99 %) was sublimed under high vacuum at $850 \,°C$ prior to use. A mixture of small pieces of Sr and powdered red P in the ratio 1:1 was sealed in a Nb tube inside a protective silica tube. This was heated at $2 \,°C/min$ to $800 \,°C$ and held for 3 days. The resulting mixture was ground to a fine powder. SrO powder was prepared by the thermal decomposition of $SrCO_3$ (Alfa 99.99 %) by heating to $850 \,°C$ and holding for 16 hours, then $1100 \,°C$ for 4 hours, under dynamic vacuum. SrO, the SrP mixture, Sc_2O_3 powder (Metall Rare Earth Limited, Shenzhen, China, 99.99 %), Fe powder (Alfa 99.998 %), and Fe_2O_3 powder (Alfa 99.998 %) were mixed according to the stoichiometry Sr_2ScO_3FeP. After homogenisation by grinding in a pestle and mortar, this powder was pelletised and placed in an alumina crucible, then sealed in an evacuated silica ampoule. This was

---

[1]A getter is used to remove any residual gas from an evacuated vessel [127].
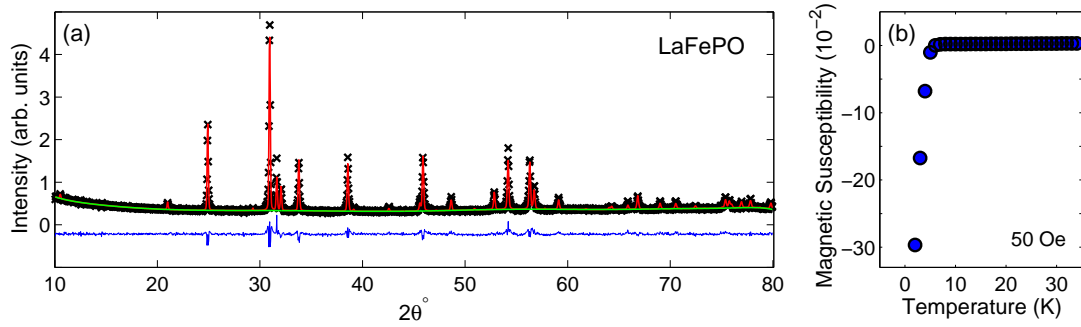
Figure 6.3: Characterisation of LaFePO. (a) Rietveld refinement against XRPD data (black crosses) taken at room temperature, the calculation (red line), the calculated background (green line) and the difference between calculation and data (blue line) are shown. (b) The results of a magnetic susceptibility measurement made on a portion of the sample in an applied field of 50 Oe under ZFC conditions. Susceptibility is expressed in SI units (see § 3.2.2).

heated at $2\,^\circ\mathrm{C/min}$ to $1200\,^\circ\mathrm{C}$ and held for 10 hours. The final product was removed and ground to a fine powder.

6.3 Characterisation

Room temperature XRPD was used to assess the phase purity of all the products (see § 3.2.1). Structural refinements against XRPD data were carried out using the Rietveld refinement package GSAS + EXPGUI. DC susceptibility measurements were performed from 2 K to 300 K in a measuring field of 50 Oe (§ 3.2.2).

6.3.1 LaFePO

A typical result of the characterisation of LaFePO is shown in Fig. 6.3. Figure 6.3(a) shows XRPD data together with the calculated pattern based on the results of the Rietveld refinement. The refinement gave lattice parameters $a = b = 3.9646(2)\,\text{Å}$ and $c = 8.5187(5)\,\text{Å}$ for space group $P4/nmm$, where the error is the estimated standard deviation calculated by GSAS. The standard deviation of lattice parameter values measured on several samples was $\sigma(a) = 0.0003\,\text{Å}$ and $\sigma(c) = 0.001\,\text{Å}$. Figure 6.3(b) shows a ZFC magnetic susceptibility measurement on the same sample. This confirms $T_\mathrm{c} \approx 4.5\,\text{K}$, and I estimate the overall superconducting volume fraction of the sample used for the neutron scattering experiments to be $\sim$20 % at 2 K, consistent with previous reports [126, 144].

6.3.2 LaZnPO

LaZnPO is isostructural with LaFePO and was synthesised to use as a non-magnetic background for comparison to LaFePO in the neutron scattering experiments. XRPD
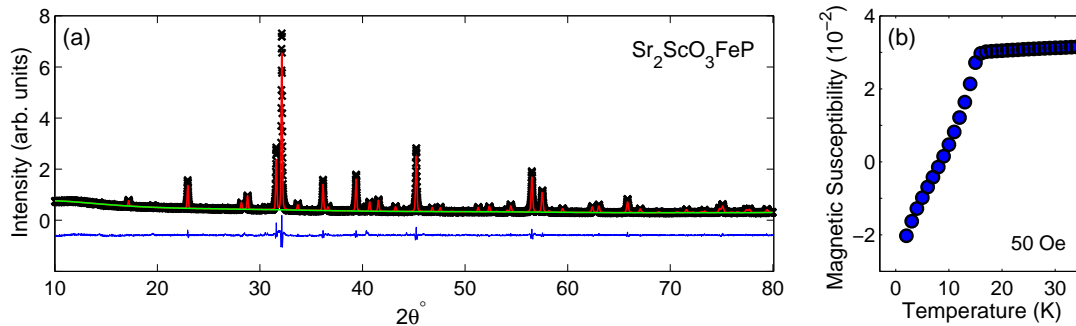
Figure 6.4: Characterisation of Sr_2ScO_3FeP. (a) Rietveld refinement against XRPD data (black crosses) taken at room temperature, the calculation (red line), the calculated background (green line) and the difference between calculation and data (blue line) are shown. (b) The results of a magnetic susceptibility measurement made on a portion of the sample in an applied field of 50 Oe under ZFC conditions. Susceptibility is expressed in SI units (see § 3.2.2).

revealed a phase pure sample and the refined structure gave lattice parameters $a = b = 4.04203(3)$ Å and $c = 8.90626(9)$ Å with space group $P4/nmm$.

6.3.3 Sr_2ScO_3FeP

A typical result of the characterisation of a Sr_2ScO_3FeP sample is shown in Fig. 6.4. Figure 6.4(a) shows XRPD data along with the calculated pattern based on the results of the Rietveld refinement for Sr_2ScO_3FeP with space group $P4/nmm$. Unlike the previous report on this material by Ogino *et al.* [128], in which they found Sr_2ScO_3FeP and $SrFe_2P_2$ in the ratio 9:1, the Sr_2ScO_3FeP phase alone describes the data very well (Fig. 6.4(a)). The Rietveld refinement gave lattice parameters $a = b = 4.0148(3)$ Å with $\sigma(a) = 0.002$ Å and $c = 15.551(2)$ Å with $\sigma(c) = 0.02$ Å, where errors are determined as described above for LaFePO. These lattice parameters are similar (within the error) to those previously reported [128]. Magnetic susceptibility measurements shown in Fig. 6.4(b) established that the onset of superconductivity occurs at $T_c \approx 15$ K, but it appears to be related to a superconducting volume fraction of only a few percent. By contrast, the sample reported by Ogino *et al.* [128] that contained small amounts of impurity phases was a bulk superconductor. This suggests that the superconducting phase is most likely a slightly off-stoichiometric form of Sr_2ScO_3FeP, and that Sr_2ScO_3FeP is close to a superconducting instability but may not be an intrinsic bulk superconductor. Further investigation on this point is beyond the scope of this thesis, but the results of the INS experiments are discussed with this in mind.

6.4 Experimental set-up

The INS experiments were performed on the ToF chopper spectrometers MERLIN at the ISIS Facility, and IN5 at the ILL (see § 3.5). Both of these instruments allow measurement of vast regions of (Q, E) space, which is advantageous when searching
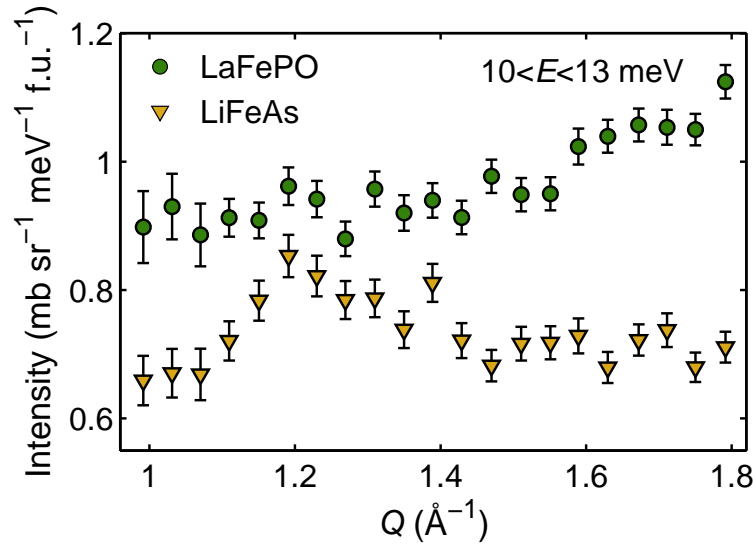
Figure 6.5: LaFePO and LiFeAs constant-energy cuts. Cuts showing the magnetic signal at $Q \approx 1.2\,\text{Å}^{-1}$ in LiFeAs, and the same region in (Q, E) space for LaFePO. Data were measured on MERLIN at $T = 20\,\text{K}$, with an incident energy $E_\text{i} = 25\,\text{meV}$, and have been averaged over an energy range of 10–13 meV.

throughout the BZ for evidence of magnetic excitations. For each measurement I sealed the powder in an annulus around the edge of a cylindrical aluminium can (§ 3.5.6). 10.6 g of LaFePO, 8.8 g of $\text{Sr}_2\text{ScO}_3\text{FeP}$ and 7.9 g of LaZnPO powder were measured. On MERLIN LaFePO and $\text{Sr}_2\text{ScO}_3\text{FeP}$ were measured with incident neutron energies $E_\text{i} = 25$ and 50 meV at temperatures of $T = 6$ and 20 K. On IN5 LaFePO and LaZnPO were measured with incident neutron energies $E_\text{i} = 3.27$, 4.23 and 7.51 meV at temperatures of $T = 1.6$ and 10 K. In all cases the spectra were normalised (§ 3.5.5) to place them on an absolute intensity scale with units $\text{mb}\,\text{sr}^{-1}\,\text{meV}^{-1}\,\text{f.u.}^{-1}$, where the f.u. is of LaFePO, LaZnPO or $\text{Sr}_2\text{ScO}_3\text{FeP}$, as appropriate.

6.5 Results

Figures 6.5 and 6.6 compare the INS response of the phosphide materials with that of LiFeAs. The LiFeAs measurement was described in Chapter 5. The conditions on MERLIN for the phosphides measurements were matched to those used for the LiFeAs measurement. The data in these figures are at 20 K, which is greater than T_c in all cases, to ensure comparison of the normal state in all samples. In Fig. 6.5, I compare constant-energy cuts from LaFePO ($T_\text{c} \approx 4.5\,\text{K}$) and LiFeAs ($T_\text{c} = 17\,\text{K}$) data sets. The peak resulting from quasi-2D spin fluctuations with characteristic in-plane wavevector close to $\boldsymbol{Q}_\text{SDW} = (0.5, 0)$ [Chapter 5] is visible in the LiFeAs data at $Q \approx 1.2\,\text{Å}^{-1}$. No such peak is present in the LaFePO data, whose intensity increases smoothly with Q due to phonon scattering.

I quantified this by attempting to fit a Gaussian peak at $Q \approx 1.2\,\text{Å}^{-1}$ to the LaFePO

data, and found an upper limit of about 15 % on the size of any such peak relative to the LiFeAs peak. To do this I fitted the LiFeAs data to a Gaussian peak on a linear background, then constrained the peak width ($\sigma = 0.18\,\text{Å}^{-1}$)[2] and centre ($Q = 1.2\,\text{Å}^{-1}$) and fitted the LaFePO data to the same function. This resulted in a peak amplitude consistent with zero, with a fitting error 15 % of the size of the LiFeAs peak amplitude. As the spectra are normalised to one f.u. and one f.u. contains one Fe atom in both materials, a magnetic signal of given intensity per Fe would appear the same size in both spectra. Therefore, assuming the spin fluctuations have a similar character in both materials, the spin fluctuations are at least 7 times weaker in LaFePO than in LiFeAs.

Figure 6.6 shows the same LiFeAs data, this time compared to a constant-energy cut from the Sr_2ScO_3FeP ($T_c = 15\,\text{K}$) data measured at $20\,\text{K}$. The Sr_2ScO_3FeP data have been shifted down by one unit to aid comparison. The non-magnetic signal appears larger for Sr_2ScO_3FeP than LiFeAs because the spectra are normalised to one f.u. and the f.u. of Sr_2ScO_3FeP contains more atoms than that of LiFeAs. By performing a similar analysis as for LaFePO, I found an upper limit of 25 % on the size of any LiFeAs-type magnetic peak in the Sr_2ScO_3FeP data.

Figure 6.7(a) shows constant-energy cuts through LaFePO data averaged over 1.8 to $2.2\,\text{meV}$, covering the energy where a magnetic resonance would be expected, assuming the scaling relation $E_r \approx 5k_B T_c$ (§ 2.4). Data are shown from measurements at temperatures of $10\,\text{K}$ and $1.6\,\text{K}$, i.e. above and below T_c. The peak centred at $Q \approx 1.05\,\text{Å}^{-1}$ is a feature of the non-magnetic background. This is demonstrated in Fig. 6.7(b), which contains the same LaFePO $1.6\,\text{K}$ data together with an equivalent cut taken from the data on the non-magnetic reference sample LaZnPO. All the features in the LaFePO data are reproduced in the LaZnPO data. If a magnetic resonance was present in Fig. 6.7(a) it would be expected to appear as an enhancement in intensity below T_c, centred on the nesting wavevector of the Fermi surface of LaFePO ($Q_{\text{nest}} \approx 1.2\,\text{Å}^{-1}$ [51]). No such enhancement is found.

To be more quantitative I made cuts through the data, like those in Fig. 6.7(a), at each of the neutron incident energies measured on IN5, and subtracted the $10\,\text{K}$ data from the $1.6\,\text{K}$ data. I attempted to fit Gaussian peaks centred on $Q = 1.2\,\text{Å}^{-1}$ to the subtracted data. From the fit I estimate the maximum area of any such peak as 15 % of the peak area at the resonance energy of LiFeAs.

Figure 6.8 shows constant-energy cuts through the Sr_2ScO_3FeP data, averaged over an energy range of 6 to $8\,\text{meV}$, recorded at $20\,\text{K}$ and $6\,\text{K}$. This is the approximate

---

[2]As mentioned in § 6.1, Maier *et al.* [136] predicted the magnetic scattering to be broader in Q for a nodal superconductor. Ishikado *et al.* [137] performed a polycrystalline INS measurement of the nodal superconductor $BaFe_2(As_{0.65}P_{0.35})_2$ on the 4SEASONS spectrometer at J-PARC. They fitted the signal with a Gaussian function with a width that varied with neutron incident energy. They found $\sigma = 0.12$ and $0.11\,\text{Å}^{-1}$ for $E_i = 45.5$ and $21.6\,\text{meV}$, respectively, which is significantly narrower than the Gaussian fit to the LiFeAs data measured on MERLIN with $E_i = 25\,\text{meV}$. Therefore, it seems appropriate to fix the width of the Gaussian to the width that was found for a material measured under the same experimental conditions. Considering the results of Maier *et al.* [136], no significant reduction in the calculated integrated intensity of the scattering signal is anticipated to arise from this assumption.
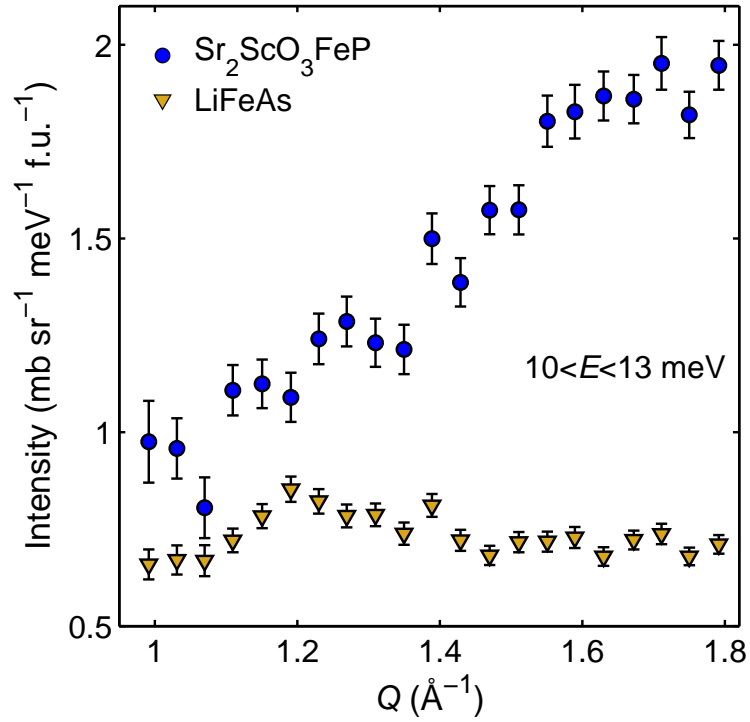
Figure 6.6: Sr$_2$ScO$_3$FeP and LiFeAs constant-energy cuts. Cuts showing the magnetic signal at $Q \approx 1.2\,\text{Å}^{-1}$ in LiFeAs and the same region of (Q, E) space for Sr$_2$ScO$_3$FeP. Data were measured on MERLIN at $T = 20\,\text{K}$, with an incident energy $E_\text{i} = 25\,\text{meV}$, and have been averaged over an energy range of 10–13 meV. The Sr$_2$ScO$_3$FeP data have been shifted down by 1 unit for clarity.
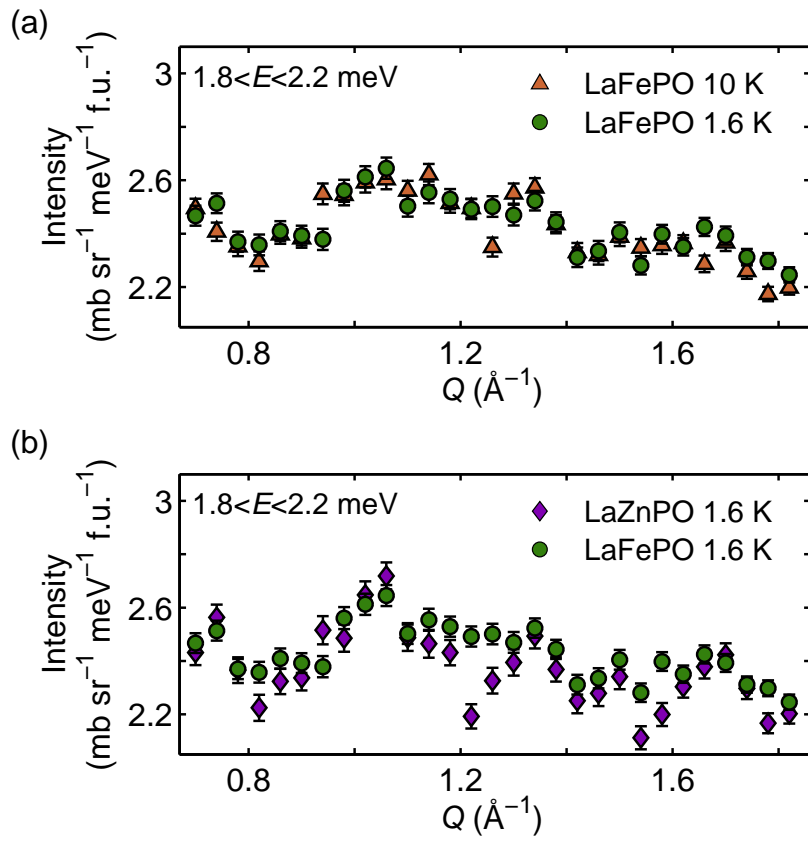
Figure 6.7: LaFePO low-energy cuts. Constant-energy cuts through data measured on IN5 with an incident energy $E_i = 3.27$ meV, averaged over an energy range of 1.8–2.2 meV. (a) Cuts through LaFePO data taken at 10 K and 1.6 K, above and below T_c, respectively. (b) The same LaFePO data as in (a) measured at 1.6 K, with data from LaZnPO at 1.6 K.
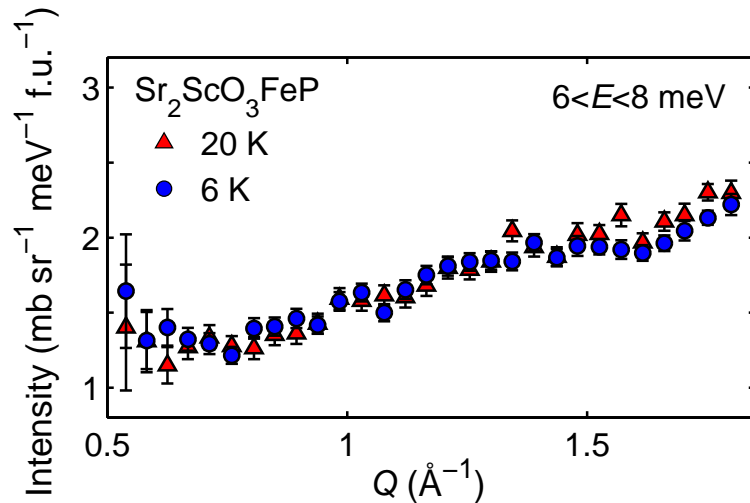
Figure 6.8: Sr_2ScO_3FeP constant-energy cuts. Cuts through Sr_2ScO_3FeP data measured at 6 K and 20 K on MERLIN with an incident energy $E_i = 25$ meV, averaged over an energy range of 6–8 meV.

energy at which a magnetic resonance is expected in iron-based superconductors with the same T_c as Sr_2ScO_3FeP (§ 2.4). To within the statistical error, there is no difference between these data sets from above and below T_c.

In addition to the representative cuts shown in Fig. 6.7 and 6.8, I examined the LaFePO and Sr_2ScO_3FeP spectra at all energies and wavevectors accessible in the measurements. I compared runs recorded at different temperatures, as well as (in the case of LaFePO) the samples with and without Fe. Cuts at constant wavevector were also inspected in a similar way. No signal attributable to magnetic fluctuations could be found either in the superconducting or in the normal state of either material.

6.6   Discussion

The goal of the work presented in this chapter was to determine whether prominent magnetic fluctuations, similar to those observed in other iron-based superconductors, are present in the iron-phosphide systems LaFePO and Sr_2ScO_3FeP. To within the limits of the experimental sensitivity, I find no evidence for any magnetic fluctuations in these systems. Either the magnetic fluctuations are weaker than in other iron-based superconductors, or their characteristic length and time scales are too short to allow detection by INS.

This null result is interesting because there are reasonable expectations that magnetic fluctuations might exist in the iron phosphides. Firstly, like many of the iron-arsenide and iron-chalcogenide materials, the two iron phosphides studied here have Fermi surfaces with quasi-nested hole and electron pockets centred on $(0, 0)$ and $(0.5, 0)$, respectively [51, 147–149]. As discussed in § 2.3 and § 2.5, in the arsenides and chalcogenides quasi-nesting is widely thought to drive the SDW transition and ex-

plain the presence of strong spin fluctuations across the phase diagrams of these compounds [15, 25, 49, 62]. In fact, as I discussed in Chapter 2, quasi-nesting may not even be a necessary condition for spin fluctuations. Secondly, in the case of LaFePO, there is experimental evidence of magnetism. Anomalous static magnetic correlations were found in μSR measurements [141], and an NMR study on Ca-doped LaFePO (Ca doping increases the T_c of LaFePO to 7 K [144]) reported evidence for moderate FM fluctuations [140, 150]. FM fluctuations would produce a peak in the neutron spectrum at $Q = 0$. If the fluctuations were 2D in character, as suggested by Nakai *et al.* [140], this peak would extend to $Q > 0$ with decreasing intensity; if the fluctuations were 3D they would result in additional peaks at $Q_{(001)} = 0.74\,\text{Å}^{-1}$, $Q_{(002)} = 1.48\,\text{Å}^{-1}$, etc. No magnetic signal is observed in the data above the background at these or at any other wavevector probed (see Fig. 6.7).

As the data are normalised in absolute units (§ 3.5.5), I have been able to constrain the size of any magnetic signal in the phosphides. LiFeAs was used as a reference because, despite poor Fermi surface nesting and no SDW order, the magnetic fluctuations observed at $Q \approx Q_{\text{SDW}}$ in LiFeAs are of a typical strength for FeAs-based superconductors (see Chapter 2 and Refs. [114, 123]). My analysis has shown that a magnetic peak of the type found in the normal state of LiFeAs, if present, would have to be at least a factor of 4 (Sr_2ScO_3FeP) or 7 (LaFePO) smaller than in other iron-based systems.

The absence of observable magnetic fluctuations in LaFePO is consistent with evidence that it is more metallic than iron-arsenide superconductors [144], and suggests that electronic correlations in LaFePO are weaker than in iron arsenides, as reported in some previous studies [83, 138]. Others, however, suggest that the correlations are of similar strength in the two families, based on Fermi surface measurements and calculations [51, 151]. In the iron-arsenide systems, a significant suppression of magnetic fluctuations has been observed in electron-overdoped samples of $Ba(Fe_{1-x}Co_x)_2As_2$ [152] and $LaFeAsO_{1-x}F_x$ [153]. However, T_c increases on electron doping in $LaFePO_{1-x}F_x$ [144], which implies that LaFePO is not an intrinsically electron-overdoped material. It is possible, therefore, that the suppression of magnetic fluctuations is intrinsic to LaFePO and would be reproduced across its entire phase diagram, with no SDW phase proximate to superconductivity. In such a scenario, superconductivity in LaFePO could be controlled not by spin fluctuations but by a different pairing instability, as has been suggested by Thomale *et al.* [142].

If spin fluctuations are involved in the pairing interaction then materials with weaker magnetic correlations would be expected to have lower T_c values. The results presented for LaFePO are compatible with this expectation, but those for Sr_2ScO_3FeP are not. The latter system has a relatively high maximum reported T_c of 17 K, yet the results show that it lacks the strong spin fluctuations characteristic of iron-arsenide and iron-chalcogenide superconductors with comparable T_c values. As discussed above, it appears that stoichiometric Sr_2ScO_3FeP is not a bulk superconductor. However, the results presented here along with the report by Ogino *et al.* [128] suggest that Sr_2ScO_3FeP is close to the superconducting instability. Strong magnetic fluctuations are therefore expected as a precursor to the superconducting state. The absence of strong magnetic fluctuations in stoichiometric Sr_2ScO_3FeP could imply that superconductivity is not

associated with a magnetic instability.

6.7   Conclusions

I have reported measurements of the INS response of two iron-phosphide materials, LaFePO and Sr_2ScO_3FeP. No evidence was found for any magnetic fluctuations in the spectrum of either material in the energy and wavevector ranges probed. I paid special attention to the wavevector Q_{SDW} at which fluctuations are seen in other iron-based systems, such as $SrFe_2As_2$ and LiFeAs (Chapters 4 and 5). The analysis shows that the magnetic signal, if present, is at least a factor of four (Sr_2ScO_3FeP) or seven (LaFePO) smaller than in the related iron-arsenide and iron-chalcogenide superconductors.

In the context of other iron-based superconductors this is a surprising result. Magnetic fluctuations are generally seen across the phase diagram of a superconducting family — particularly where the Fermi surface shows quasi-nesting — and strong suppression of the fluctuations has only been reported in electron-overdoped materials. LaFePO is not an electron-overdoped material, as Ca doping on the La site increases T_c. Because of its relatively high T_c (17 K), identification of the precise composition of the superconducting phase in Sr_2ScO_3FeP would be a significant step towards an understanding of the mechanism of superconductivity in the iron-phosphide systems.

The results presented in this chapter suggest that magnetic fluctuations are not as influential to the electronic properties of the iron-phosphide systems as they are in other iron-based superconductors. Thomale *et al.* [142] used a five-band model to explain the nodal gap symmetry in FeP systems, and suggested a possible reduction in SDW fluctuations. However, there is motivation for further models to explain the behaviour of the iron-phosphide materials and determine whether superconductivity is mediated by weak spin fluctuations or by a different pairing instability.

Spin waves and the magnetic resonance in $\mathbf{Cs}_x\mathbf{Fe}_{2-y}\mathbf{Se}_2$

Contents
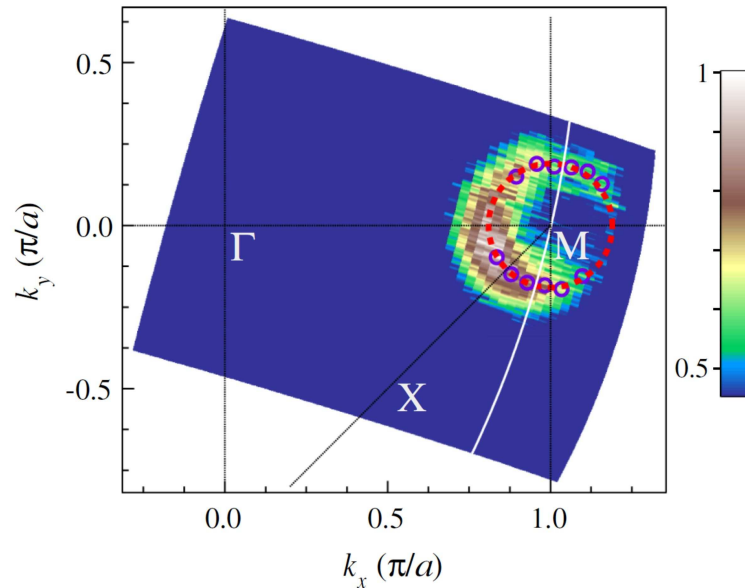
Figure 7.1: ARPES measurement of $K_x Fe_{2-y} Se_2$. ARPES intensity data from a measurement on a single crystal of $K_x Fe_{2-y} Se_2$. An electron pocket is visible at the point labelled M, which is $(0.5, 0)$ in one-Fe unit cell reciprocal lattice notation. No hole pocket is observed around the centre of the BZ, Γ. Reprinted figure with permission from T. Qian *et al.*, Phys. Rev. Lett., **106**, 187001, 2011 [160]. Copyright (2011) by the American Physical Society.

7.1   Introduction

In this chapter I report INS measurements on the normal and superconducting states of $Cs_{0.8}Fe_{1.9}Se_2$. This material is a member of the $A_x Fe_{2-y} Se_2$ (A = K, Rb, Cs or Tl) family of materials, which are based on iron-selenide layers rather than iron-pnictide layers like the materials discussed in the previous chapters. The $A_x Fe_{2-y} Se_2$ compounds present an interesting new twist in the field of iron-based superconductors. Superconductivity with $T_c \approx 30\,K$ was discovered in these systems [154–157] in samples that also host magnetic order with an unusually-high T_N of up to $559\,K$ and a large ordered moment of about $3.3\,\mu_B$ per Fe [158]. This discovery naturally raises the question: can superconductivity coexist microscopically with such a robust magnetic state? Although there are regions in the phase diagrams of iron-pnictide superconductors in which magnetism and superconductivity are believed to coexist microscopically (see § 2.3 and Fig. 2.3), the highest T_cs and bulk superconductivity are found when the magnetic state has been suppressed [15, 24, 28, 49]. Another distinct feature of the $A_x Fe_{2-y} Se_2$ systems is their band structure [159, 160]. As illustrated in Fig. 7.1, the Fermi surface lacks the large hole pocket at the zone centre that features prominently in theories of superconductivity and magnetism in other iron-based superconductors (§ 2.5).

The magnetic structure found in superconducting $A_x Fe_{2-y} Se_2$ samples is depicted in Figs. 7.2(a) and (c). It consists of blocks of four ferromagnetically-aligned Fe spins, with AFM alignment between these blocks. The spins are aligned along the c-axis, not in the

a–b-plane like the SDW state observed in many iron-based superconductors (Fig. 2.2). This magnetic state forms on a superstructure of ordered Fe vacancies described by tetragonal space group symmetry $I4/m$ [158, 161–164], shown by the black unit cell marked in Fig. 7.2(a) and by the pink square in Fig. 7.2(c). This vacancy structure has optimal composition $A_{0.8}Fe_{1.6}Se_2$. The magnetic structure has two domains, as illustrated in Fig. 7.2(c).

Initial experimental investigations of $A_xFe_{2-y}Se_2$ supported a picture of microscopic coexistence of the superconducting and AFM states [154, 156, 158, 158, 165–169]. These studies were backed up by calculations based on the AFM state [170–172]. Further work, however, has found evidence for a spatial separation of superconducting (metallic) and AFM (insulating or semiconducting) phases [163, 173–176]. Recent results from NMR [177], scanning electron microscopy [178, 179], optical spectroscopy [180], Raman scattering and optical microscopy [181], and μSR [182, 183] may help to explain the apparent discrepancies in the earlier work. They indicate that phase separation occurs with a complex plate-like morphology on a sub-micron scale. Proximity effects between nanodomains could therefore allow an interplay between superconducting and magnetic regions, and may explain the apparent bulk superconductivity despite estimates of a genuine superconducting phase fraction of only 5–10 %. Results from scanning tunnelling microscopy [184, 185], high-resolution x-ray diffraction [186], NMR [177], and combined x-ray and neutron diffraction [187] have indicated that the superconducting phase does not have the iron-vacancy structure of the main phase. Instead, the superconducting phase is described by the formula $A_xFe_2Se_2$, with x found to be in the range 0.3–1. The structure of this phase is shown in Fig. 7.2(b), using $x = 1$, and is similar to the structure of the paramagnetic phase of $SrFe_2As_2$ (Chapter 4) and $BaFe_2As_2$ (see Fig. 2.1). No static magnetic order associated with this phase has been found.

The interplay between superconductivity and static magnetic order remains a key issue in the $A_xFe_{2-y}Se_2$ family. The magnetic dynamics are also important as they are widely thought to play a role in mediating superconductivity in the iron-based superconductors, as discussed in the previous chapters. Initial investigations of the magnetic dynamics in $A_xFe_{2-y}Se_2$ materials focused on $Rb_xFe_{2-y}Se_2$. The spin-wave spectrum of the insulating parent AFM phase, $T_N = 475$ K, has been measured by INS in a non-superconducting sample [188]. Wang *et al.* [188] successfully modelled the results in terms of a local-moment Heisenberg Hamiltonian, and found no need to include itinerant effects to accurately describe the data, in contrast to the case of $SrFe_2As_2$ discussed in Chapter 4.

Superconducting samples of $Rb_xFe_{2-y}Se_2$, $T_c = 32$ K, have also been studied, and a magnetic resonance was discovered by Park *et al.* [189]. This magnetic resonance is quasi-2D and characterised by an increase in scattering intensity below T_c at an energy of approximately 14 meV ($\approx 5k_BT_c$) and at the wavevector $\boldsymbol{Q} = (0.25, 0.5)$ and equivalent positions [189]. This wavevector is not the same as the usual wavevector of the resonance in iron-based superconductors, $\boldsymbol{Q} = (0.5, 0)$, that was discussed in previous chapters.

The discovery by Park *et al.* [189] represents the first observation of a magnetic res-
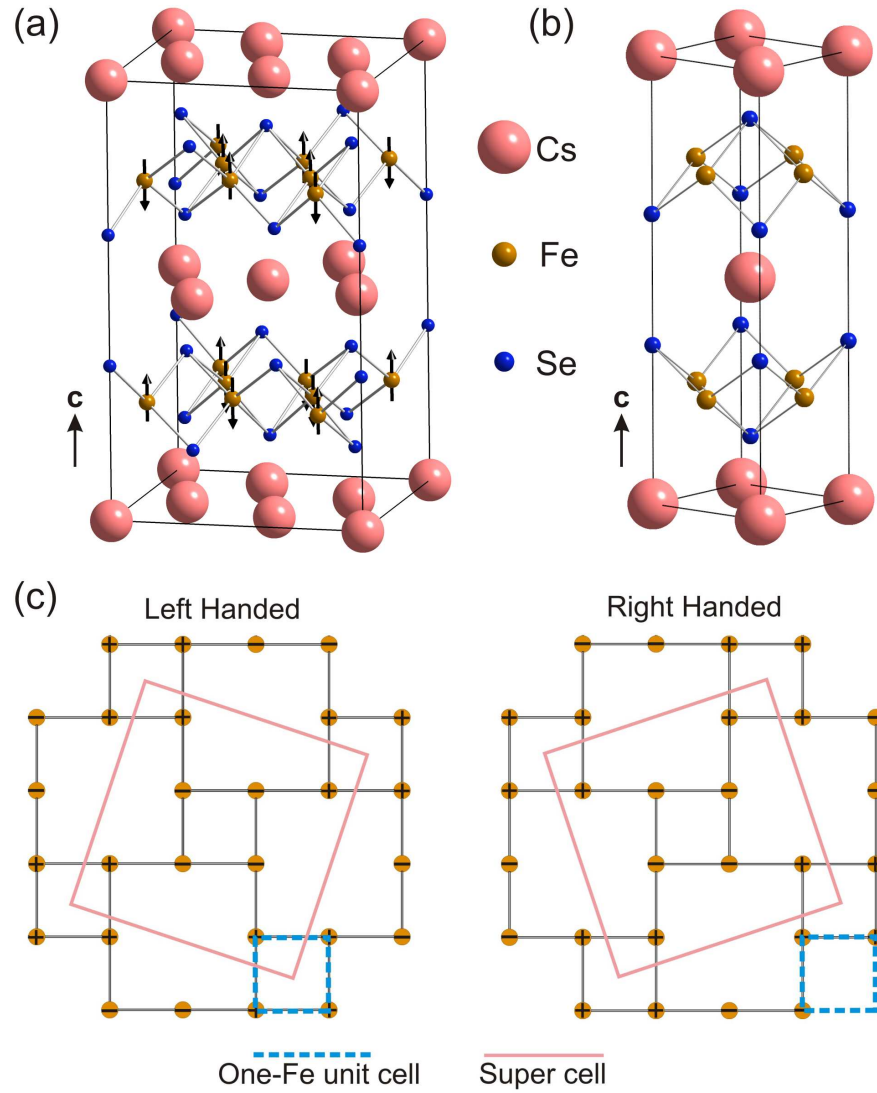
Figure 7.2: Structure of $A_x\mathbf{Fe}_{2-y}\mathbf{Se}_2$. (a) The magnetic and vacancy ordered structure of $A_x\mathrm{Fe}_{2-y}\mathrm{Se}_2$. The arrows represent the spins on the iron sites. The black lines mark one unit cell with space group symmetry $I4/m$. (b) The structure believed to correspond to the superconducting phase of $A_x\mathrm{Fe}_{2-y}\mathrm{Se}_2$ materials, with space group symmetry $I4/mmm$. This phase is free from iron vacancies, and has the chemical formula $A_x\mathrm{Fe}_2\mathrm{Se}_2$. It is illustrated with full occupancy on the A site for clarity. (c) A projection onto the a–b-plane of a single iron layer from the magnetic structure shown in (a), for both possible domains. Plus and minus symbols represent spins pointing into and out of the plane of the diagram, respectively.
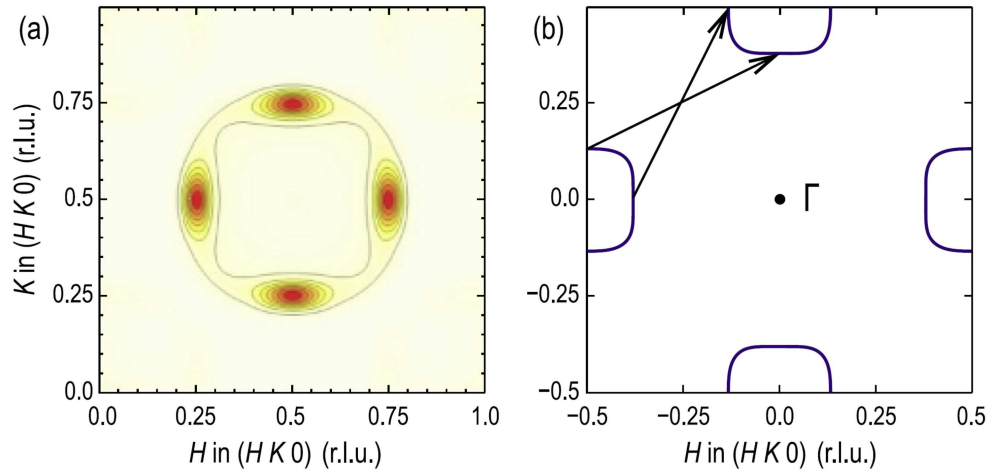
Figure 7.3: Model of magnetic resonance and Fermi surface. The results of random phase approximation calculations for A_xFe$_{2-y}$Se$_2$ systems, based on Ref. [191] and adjusted to fit the data from Rb$_x$Fe$_{2-y}$Se$_2$ in Ref. [190]. Panel (a) shows the difference between the superconducting and normal state calculations of the imaginary part of the dynamic susceptibility (Eq. 3.21), evaluated at the energy of the resonance. The $(H, K, 0)$ plane of the Fermi surface from the calculation is shown in (b), with the nesting wavevector $(0.25, 0.5)$ indicated by the black arrows. Reprinted figure with permission from G. Friemel *et al.*, Phys. Rev. B, **85**, 140511(R), 2012 [190]. Copyright (2012) by the American Physical Society.

onance away from $(0.5, 0)$ in the iron-based superconductors.[1] This is perhaps unsurprising given the absence of a hole pocket at $(0.5, 0)$ on the Fermi surface of A_xFe$_{2-y}$Se$_2$ systems (Fig. 7.1). The hole pocket is crucial to explaining the resonance in the discussion presented in § 2.5.

In Refs. [189, 190] it was suggested that the position of the magnetic resonance in Rb$_x$Fe$_{2-y}$Se$_2$ might instead be traced to the nesting of electron-like Fermi surface pockets, as illustrated in Fig. 7.3(b). Friemel *et al.* [190] modelled their INS results based on the theory of Maier *et al.* [191] who predicted a d-wave superconducting pairing state in the A_xFe$_{2-y}$Se$_2$ systems, unlike the $s_\pm$ pairing generally thought to be present in most other iron-based superconductors (§ 2.6). The d-wave gap symmetry implies a sign change between the electron pockets separated by $Q = (0.25, 0.5)$ [compare Fig. 2.7 to Fig. 7.3(b)]. Therefore, following the BCS coherence factor description (§ 2.5), Eq. 2.2 implies that a resonance feature would appear at $(0.25, 0.5)$ for d-wave pairing. A d-wave superconducting gap symmetry could therefore explain the results of Park *et al.* [189] within the framework described in § 2.5, although it is worth noting that the validity of a d-wave state for A_xFe$_{2-y}$Se$_2$ systems is disputed by Mazin in Ref. [192]. In another INS study of Rb$_x$Fe$_{2-y}$Se$_2$, a magnetic signal was reported close to $\boldsymbol{Q} = (0.5, 0) = \boldsymbol{Q}_{\text{SDW}}$, in addition to spin-wave excitations from the block AFM order and a magnetic-resonance-like feature at $\boldsymbol{Q} = (0.25, 0.5)$ [193].

---

[1]In some measurements the magnetic resonance has been observed at incommensurate wavevectors close to $(0.5, 0)$, as discussed in Chapter 5.

Here I report measurements of the spin excitations in single crystals of superconducting $Cs_xFe_{2-y}Se_2$, with particular focus on the low-energy magnetic features and their response to superconductivity. I set out to answer the questions: (i) are spin-wave excitations characteristic of the block AFM order present in $Cs_xFe_{2-y}Se_2$, (ii) if spin-wave excitations are present, are they modified by the presence of superconductivity, and (iii) is there a signal attributable to a resonance-like magnetic peak at any wavevector? I find that the spin excitations associated with the block AFM order have a similar spectrum to those observed in non-superconducting $Rb_xFe_{2-y}Se_2$ up to the highest energy probed ($\sim$150 meV), and are not affected by superconductivity. I also report the observation of a resonance-like magnetic peak localised in energy at 11 meV and at an in-plane wavevector of $(0.25, 0.5)$. This establishes that this feature is not confined to $Rb_xFe_{2-y}Se_2$. These observations are consistent with the notion of spatially separate magnetic and superconducting phases. I will discuss the implications of these results for theoretical models based on the interplay between magnetic fluctuations and superconductivity in the iron-based systems.

The results presented in this chapter have been published in Ref. [194].

7.2 Crystal synthesis and characterisation

The $Cs_xFe_{2-y}Se_2$ single crystals used in the experiment were grown by Anna Krzton-Maziopa, Ekaterina Pomjakushina and Kazimierz Conder at the Laboratory for Developments and Methods, Paul Scherrer Institute, Switzerland. The crystals were grown by the Bridgman process as described in Ref. [156]. The nominal composition of the crystals is $Cs_{0.8}Fe_{1.9}Se_2$, and their superconducting and magnetic properties are reported in Refs. [156, 161, 165]. The iron-vacancy-ordered phase (Fig. 7.2(a)) orders at $T_s \approx 500$ K with space group symmetry $I4/m$ and lattice parameters $a = 8.858$ Å and $c = 15.287$ Å. The magnetic ordering transition temperature is $T_N = 478.5$ K.

Magnetic susceptibility measurements established that the onset of bulk superconductivity occurs at $T_c = 27$ K (see Fig. 7.4). 'Bulk' here means that full flux exclusion is achieved after cooling in zero field. However, this does not necessarily imply superconducting volume fraction of 100 %, since non-superconducting regions can be screened by surface currents in a ZFC measurement (§ 3.2.2). A crystal from the same batch was analysed by scanning electron microscopy [178] and it was found that the superconducting phase makes up approximately 10 % of the sample.

7.3 Experimental set-up

To obtain a sample with a large enough mass to give an appreciable signal in the INS experiments, three small single crystals were coaligned using the ALF instrument at the ISIS facility (§ 3.5.6). The crystals were coated in Cytop varnish to protect them from air exposure during this process. They were checked for crystalline quality prior to the experiment. I remeasured a crystal from the neutron scattering sample after the experiment and found T_c to be unchanged.
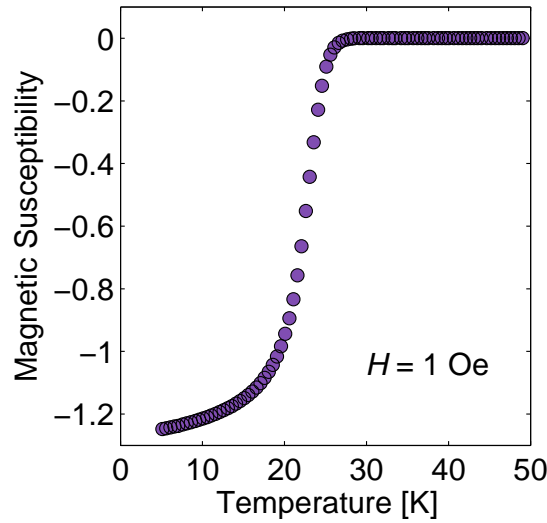
Figure 7.4: Susceptibility measurement. Magnetic susceptibility of one of the $Cs_{0.8}Fe_{1.9}Se_2$ single crystals, measured with a field of 1 Oe applied along the c-axis after cooling in zero field. Reprinted figure from A. E. Taylor *et al.*, Phys. Rev. B, **86**, 094528, 2012 [194]. Copyright (2012) by the American Physical Society.

The coalignment gave a sample of total mass 0.42 g, with a uniform mosaic of 2.5° (FWHM). The INS experiments were performed on the MERLIN spectrometer at the ISIS Facility (§ 3.5). The sample was mounted with the c-axis parallel to the incident neutron beam and the [110] direction horizontal. Therefore, in the data the out-of-plane wavevector component, L, varies with E (§ 3.5.3). Spectra were recorded with neutrons of incident energy $E_i = 33, 40, 50, 60, 100$ and 180 meV at $T = 4$ K, and $E_i = 33$ meV at $T = 4, 20, 34$ and 44 K. The scattering from a standard vanadium sample was used to normalise the spectra and place them on an absolute intensity scale (§ 3.5.5) with units mb sr^{-1} meV^{-1} f.u.$^{-1}$, where f.u. refers to $Cs_{0.8}Fe_{1.9}Se_2$.

7.4 Results

Figure 7.5(a) is a map of the (H, K) plane in 2D reciprocal space, showing the positions of the AFM Bragg peaks and the magnetic resonance signal reported in Ref. [189]. Positions in reciprocal space are indexed with respect to the one-Fe sublattice, which has lattice parameters $a = b = 2.8$ Å, $c = 7.7$ Å. Figure 7.5(b) is a map of the neutron scattering intensity averaged over the energy range 10 to 20 meV and projected onto the same region of the (H, K) plane as shown in Fig. 7.5(a). The strong scattering signal localised at $Q_{AFM} = (0.1, 0.3)$ and equivalent positions is due to magnetic fluctuations associated with the block AFM order on the Fe-vacancy superstructure (Figs. 7.2(a) and (c)). The eight-fold symmetry of the magnetic spectrum, which derives from the superposition of two four-fold patterns from left-handed and right-handed magnetic structures (Fig. 7.2(c)), is apparent from this figure. All spectra presented hereafter have been folded into one octant to improve statistics.
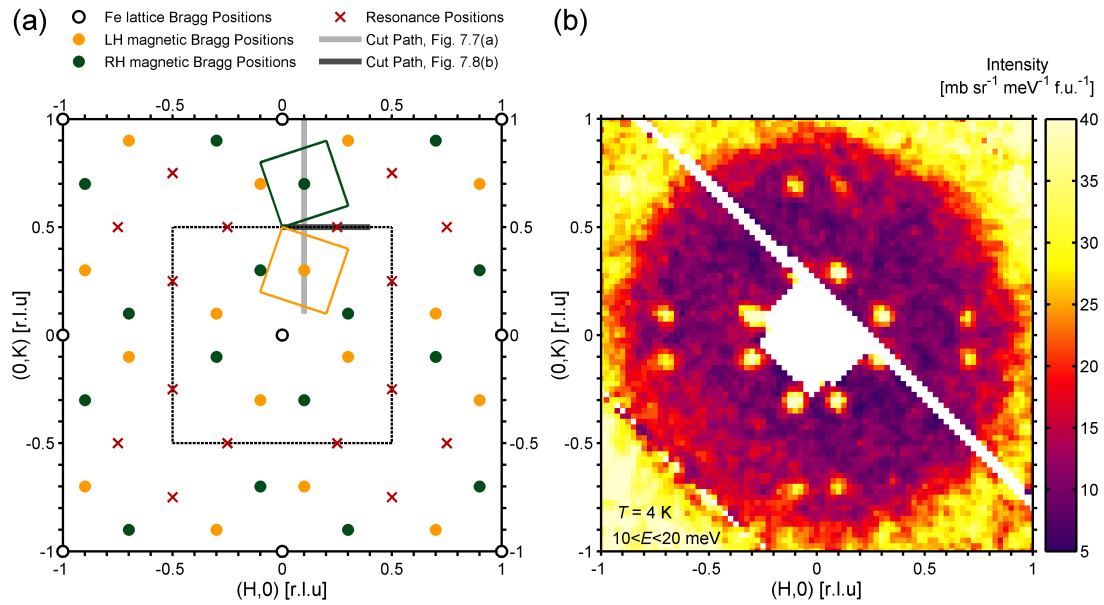
Figure 7.5: Map of reciprocal space. (a) Map of 2D reciprocal space for $Cs_xFe_{2-y}Se_2$, showing positions of the magnetic ordering vectors and the magnetic resonance signals with respect to the one-Fe unit cell. The dashed square is the first BZ for this unit cell. The two small tilted squares are the first BZs for the unit cells of the left-handed (LH) and right-handed (RH) magnetic domains (Fig. 7.2(c)). The paths along which cuts shown in later figures were taken are represented by thick solid lines. (b) Neutron scattering intensity map of $Cs_{0.8}Fe_{1.9}Se_2$ in the same area of reciprocal space as shown in (a). The data were recorded with $E_i = 100\,meV$ and averaged over an energy range of 10 to 20 meV. The areas of missing data are due to the beam stop and masked detectors. Reprinted figure from A. E. Taylor *et al.*, Phys. Rev. B, **86**, 094528, 2012 [194]. Copyright (2012) by the American Physical Society.

The magnetic spectrum is revealed in more detail in Fig. 7.6, which shows a strongly dispersive spin-wave band extending from below 20 meV up to 63 meV, and a second band between 85 and 120 meV. The existence of the latter is demonstrated in Fig. 7.6(a) via two energy scans recorded at fixed wavevectors of $(0.1, 0.5)$ and $(0.1, 1)$. These positions were chosen after inspection of an intensity map like that in Fig. 7.5(b) but at an energy of 100 meV, which showed a regular pattern of diffuse magnetic scattering with maximum intensity at $(0.1, 0.5)$ and minimum at $(0.1, 1)$.

Figure 7.6(b) plots the in-plane dispersion of the lower spin-wave band. In constant-energy maps in the (H, K) plane, the low-energy spin-wave scattering appears as a ring of intensity centred on the $\boldsymbol{Q}_{\mathrm{AFM}}$ positions. The points in Fig. 7.6(b) were obtained as follows. I made Gaussian fits to peaks in constant-energy cuts along the line $(0.1, K)$ passing through the magnetic wavevectors $\boldsymbol{Q}_{\mathrm{AFM}} = (0.1, 0.3)$ and $(0.1, 0.7)$ [see Fig. 7.5(a)]. Gaussian functions fitted to pairs of peaks symmetrically displaced either side of each $\boldsymbol{Q}_{\mathrm{AFM}}$ were constrained to have the same area and width. The peak positions were corrected for the systematic shift caused by the curvature of the dispersion surface over the width ΔH of the cuts. Where appropriate, a non-magnetic background was estimated from cuts taken along nearby lines in reciprocal space. The two peaks could not be resolved for energies below 20 meV. The points at the magnetic BZ boundaries (marked in Fig. 7.6(b) by dashed lines) were obtained from a Gaussian fit to the peak in a background-corrected energy cut. The minimum point on the dispersion was determined from an energy cut at $\boldsymbol{Q}_{\mathrm{AFM}}$ through the $E_{\mathrm{i}} = 60$ meV data.

The results shown in Fig. 7.6 bear a very close resemblance to the magnetic spectrum of non-superconducting $\mathrm{Rb}_x\mathrm{Fe}_{2-y}\mathrm{Se}_2$ reported in Ref. [188]. The data are not sufficient to determine the detailed dispersion in the out-of-plane direction $(0, 0, L)$. However, the spectra measured with different E_{i} in order to probe $\boldsymbol{Q}_{\mathrm{AFM}}$ at different L values (see § 3.5.3) are consistent with a minimum anisotropy gap of 7 ± 1 meV and a maximum of about 20 meV, somewhat lower than the maximum of 30 meV reported for $\mathrm{Rb}_x\mathrm{Fe}_{2-y}\mathrm{Se}_2$ [188]. In Ref. [188], a third spin-wave band was observed in $\mathrm{Rb}_x\mathrm{Fe}_{2-y}\mathrm{Se}_2$, with a dispersion from 180 to 230 meV. The measurements reported here did not extend high enough in energy to confirm the existence of this band in $\mathrm{Cs}_x\mathrm{Fe}_{2-y}\mathrm{Se}_2$.

Figure 7.7 shows the temperature dependence of the spin-wave peak at $\boldsymbol{Q}_{\mathrm{AFM}} = (0.1, 0.3)$ averaged over the energy range 13 to 15 meV. Figure 7.7(a) shows wavevector scans recorded at four different temperatures, two below T_{c} and two above T_{c}. The peaks show no discernible change within this temperature range. To check this quantitatively I fitted the data to a Gaussian function on a linear background, allowing the width, centre and area of the Gaussian, and the slope and intercept of the background to vary. To correct for the increase in signal due to the thermal population of spin waves, I normalised the data by the Bose population factor (§ 3.4.6). Figure 7.7(b) plots the areas of the fitted peaks as a function of temperature. To within the experimental error of about 3 % there is no change upon crossing T_{c}.

Finally, I consider the magnetic dynamics at wavevectors away from the $\boldsymbol{Q}_{\mathrm{AFM}}$ points in reciprocal space. Figure 7.8(a) shows an intensity map recorded at 4 K and averaged over the energy range 9 to 13 meV. The data have been folded onto an octant of reciprocal space to improve statistics. To within the experimental error there is no
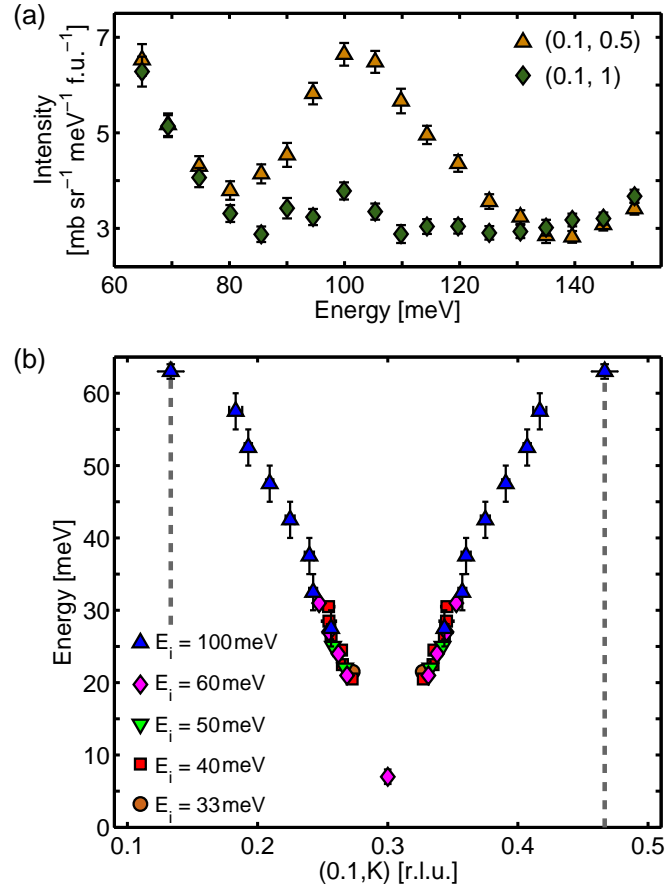
Figure 7.6: Spin-wave spectrum of $Cs_xFe_{2-y}Se_2$. (a) Energy cuts showing the band of magnetic scattering around 100 meV. The data are from a run with $E_i = 180$ meV at 4 K. The orange triangles were recorded at the wavevector $(0.1, 0.5)$, where there is a clear magnetic signal with maximum intensity near 105 meV. The green diamonds are a similar cut from the nearby position $(0.1, 1)$, which is away from any magnetic scattering. (b) Spin-wave dispersion of the low-energy band, measured at 4 K. The method used to obtain the data points is described in the text. The different coloured symbols indicate data obtained with different E_i. The dashed lines mark the magnetic BZ boundaries. For energies below 60 meV, the vertical error bars represent the width of the cut in energy and the horizontal error bars represent the error in the fitted peak position. For the two points at 63 meV, the horizontal error bar is the width of the cut in wavevector and the vertical error bar is the error from the fit. The point at 7 meV is the minimum anisotropy gap and has an out-of-plane wavevector component $L \approx 0.5$ r.l.u. Reprinted figure from A. E. Taylor *et al.*, Phys. Rev. B, **86**, 094528, 2012 [194]. Copyright (2012) by the American Physical Society.
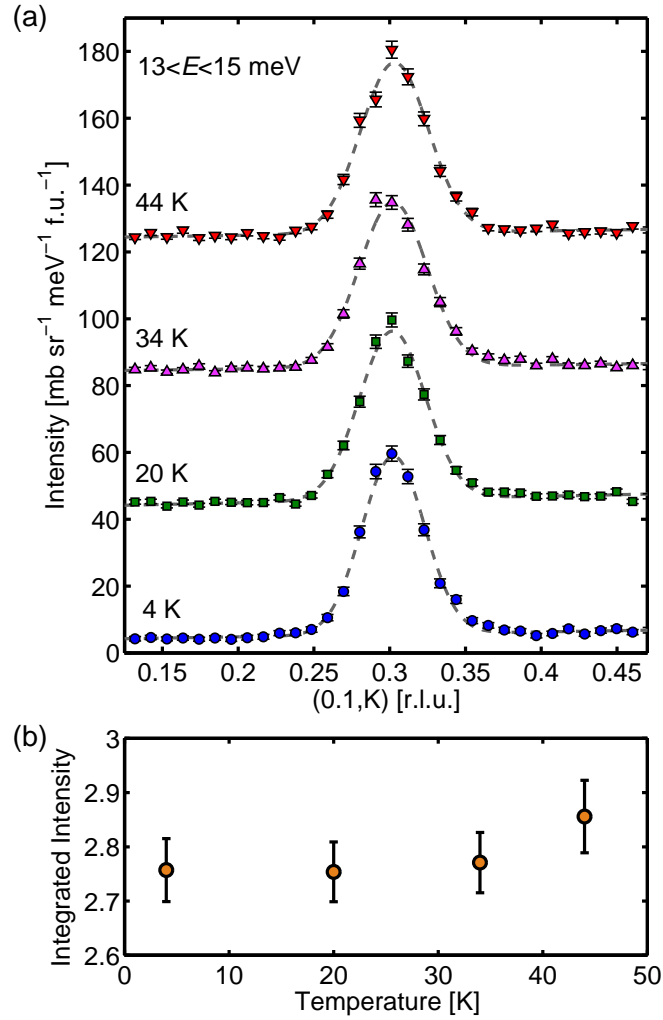
Figure 7.7: Temperature dependence of spin waves. (a) Constant-energy cuts through $Q_{AFM} = (0.1, 0.3)$ showing the temperature dependence of the spin-wave scattering averaged over the energy range 13 to 15 meV. Data were recorded with $E_i = 33$ meV, giving an out-of-plane wavevector component $L = 1.28$ r.l.u. Successive cuts are displaced vertically by 40 units for clarity. Dashed lines are fits to Gaussian peaks on a linear background, as described in the main text. (b) The integrated intensity (in mb sr^{-1} meV^{-1} f.u.$^{-1}$ r.l.u.), given by the area of the fitted Gaussian peaks, as a function of temperature. The data have been normalised by the Bose factor $[1 - \exp(-E/k_B T)]^{-1}$. Reprinted figure from A. E. Taylor *et al.*, Phys. Rev. B, **86**, 094528, 2012 [194]. Copyright (2012) by the American Physical Society.

evidence for the excitations observed near $(0.5, 0) \equiv (0, 0.5)$ by Wang *et al.* [193] in similar measurements on superconducting $Rb_xFe_{2-y}Se_2$. However, the data do reveal a weak signal centred on $(0.25, 0.5)$ with a maximum at an energy of about $11\,meV$ ($5k_BT_c \approx 12\,meV$), as shown in the inset to Fig. 7.8(a). Wavevector cuts through this peak in the $(H, 0)$ direction averaged over 9–$15\,meV$ are shown in Fig. 7.8(b), at a series of temperatures. The cut at $4\,K$, well below T_c, shows a well defined peak which I fitted with a Gaussian function on a linear background, shown as a dotted line. Fits were made to the cuts at higher temperatures with the width and centre of the Gaussian fixed to the values found at $4\,K$. The inset to Fig. 7.8(b) shows the integrated intensity of the fitted Gaussian peaks as a function of temperature. The signal increases as the temperature decreases, consistent with a magnetic resonance peak. To determine the absolute strength of the peak I have converted its integrated intensity into the **Q**-averaged or local susceptibility $\chi''(E)$ [see § 3.4.6 and Eq. 3.22]. I assumed the peak to be 2D and used the dipole form factor of Fe^{2+} (see § 3.4.4). The inset to Fig. 7.8(a) shows the energy dependence of $\chi''(E)$ at $T = 4\,K$.

In Fig. 7.9 I investigate the anisotropy of the signal at $(0.25, 0.5)$. I made cuts through the peak parallel to $(H, 0)$ and $(0, K)$, and fitted these to Gaussian functions on linear and quadratic backgrounds, respectively. Phonon scattering, which depends on Q^2 [76], dominates the background for the cut along $(0.25, K)$ [see also Fig. 7.8], hence the quadratic background was necessary in the fit. The FWHM of the peaks in the $(H, 0.5)$ and $(0.25, K)$ cuts were found to be $0.066 \pm 0.010\,r.l.u.$ and $0.070 \pm 0.016\,r.l.u.$, respectively.

7.5 Discussion

One of the goals of this work was to determine whether the spin dynamics of the block AFM phase in superconducting samples of $A_xFe_{2-y}Se_2$ are different to those in insulating samples, and whether they respond to superconductivity. Figure 7.6 presents a clear demonstration that the AFM spin-waves persist in superconducting $Cs_xFe_{2-y}Se_2$ and have a similar spectrum to that of insulating $Rb_xFe_{2-y}Se_2$ [188]. I found the top of the low-energy spin-wave branch to be $63 \pm 1\,meV$, and the centre of the medium energy band to be $105 \pm 5\,meV$, compared with $\sim$67 meV and $\sim$115 meV, respectively, found in $Rb_xFe_{2-y}Se_2$ [188].

I have found no evidence for a coupling between the low-energy spin waves and superconductivity. This is illustrated in Fig. 7.7 for an energy near $14\,meV$ where the scattering is strongest. I also examined the data from $8\,meV$ up to $27\,meV$ and found no change in the spin-wave scattering on cooling through T_c at any energy in this range. From these results, any superconductivity-induced change at low energies greater than 3–$4\,\%$ can be ruled out. By contrast, previous studies on superconducting $K_xFe_{2-y}Se_2$ reported systematic reductions of $5\,\%$ or more in the intensities of a magnetic Bragg peak and a two-magnon Raman peak at $\sim$200 meV on cooling below T_c [158, 181]. One possibility is that the size of the effect depends on the energy probed, however a more plausible explanation is based on the notion that these samples are phase separated
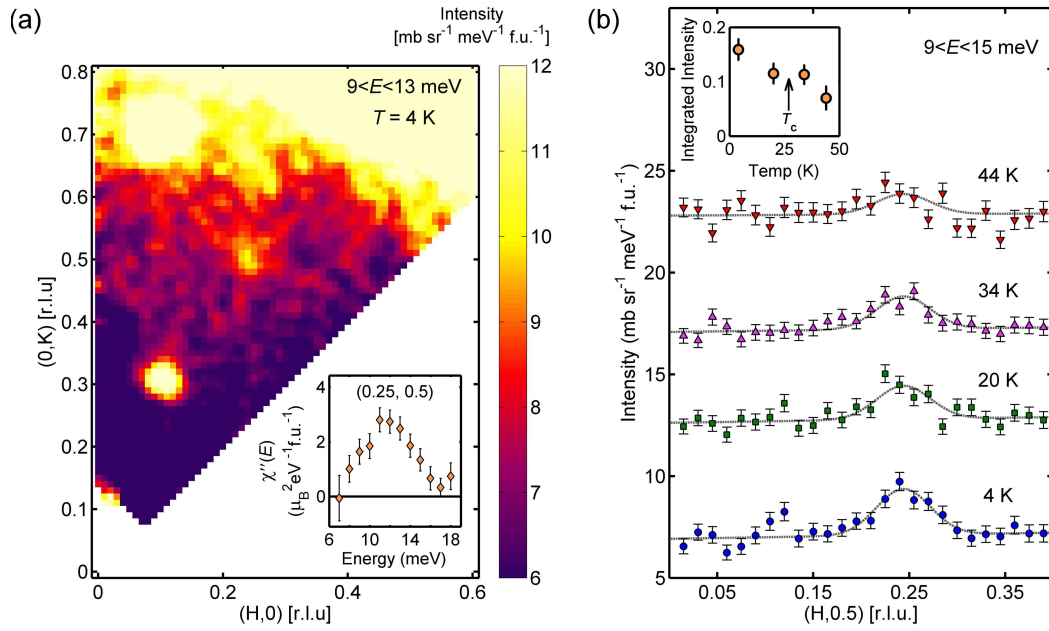
Figure 7.8: Magnetic resonance signal. (a) Neutron scattering intensity map of $Cs_xFe_{2-y}Se_2$ averaged over energies between 9 and 13 meV. The data were recorded at 4 K with $E_i = 33$ meV. The weak signal centred on $(0.25, 0.5)$ is identified with the resonance peak. The inset shows the resonance peak intensity as a function of energy, where the intensity is given as the imaginary part of the local susceptibility (§ 3.4.6). (b) Constant-energy cuts showing the temperature dependence of the resonance peak. The out-of-plane wavevector at the peak is $L = 1.3$ r.l.u. Successive cuts are displaced vertically by 5 units for clarity. The dotted lines are fits to a Gaussian peak on a linear background. The inset in (b) shows the integrated intensity (in mb sr^{-1} meV^{-1} f.u.$^{-1}$ r.l.u.) given by the Gaussian fits as a function of temperature. The data have been normalised by the Bose factor $[1 - \exp(-E/k_BT)]^{-1}$. Reprinted figure from A. E. Taylor *et al.*, Phys. Rev. B, **86**, 094528, 2012 [194]. Copyright (2012) by the American Physical Society.
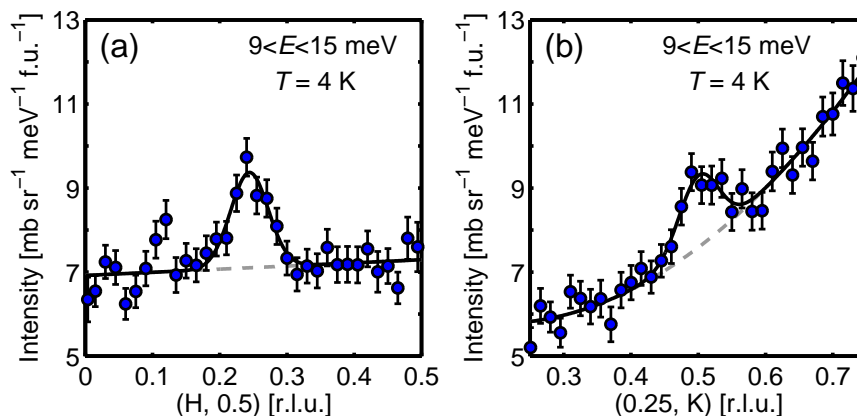
Figure 7.9: Anisotropy of signal. Constant-energy cuts through the resonance peak parallel to the (a) $(H, 0)$ and (b) $(0, K)$ directions. The data were recorded at $4\,\mathrm{K}$ with $E_\mathrm{i} = 33\,\mathrm{meV}$. The solid lines are fits to a Gaussian peak on a linear [panel (a)] or quadratic [panel (b)] background. Reprinted figure from A. E. Taylor *et al.*, Phys. Rev. B, **86**, 094528, 2012 [194]. Copyright (2012) by the American Physical Society.

on a nanoscale into superconducting and magnetically-ordered (non-superconducting) regions which only interact at the interfaces [177, 178, 180]. Below T_c, the superconducting proximity effect could suppress magnetic order near the phase boundaries, so that samples with different interfacial surface areas would respond to superconductivity by different amounts.

Although I found no effect of superconductivity on the magnetic excitations associated with the block AFM order, I have found the magnetic resonance peak at $(0.25, 0.5)$ [Fig. 7.8 (a)] previously reported in the spectrum of superconducting $\mathrm{Rb}_x\mathrm{Fe}_{2-y}\mathrm{Se}_2$ [189, 190, 193]. As shown in Fig. 7.8(b), the magnetic signal at $(0.25, 0.5)$ increases in intensity on cooling below T_c, and the peak persists at temperatures above T_c in agreement with the observations of Friemel *et al.* [190]. I have observed the resonance feature at $E \approx 11\,\mathrm{meV}$ (inset to Fig. 7.8(a)) which is consistent with the $E_\mathrm{r} \approx 5k_\mathrm{B}T_\mathrm{c}$ scaling relationship found in other iron-based superconductors (§ 2.4). However, one notable difference is the shape of the resonance peak in momentum space, which for $\mathrm{Rb}_x\mathrm{Fe}_{2-y}\mathrm{Se}_2$ was found to be highly elliptical with an aspect ratio 2.1 [190]. For $\mathrm{Cs}_x\mathrm{Fe}_{2-y}\mathrm{Se}_2$ the resonance peak is more isotropic, with an aspect ratio of 1.1 ± 0.3 (see Fig. 7.9).

The existence of resonance peaks in iron pnictides has been explained in terms of quasi-nesting features in the Fermi surface and BCS coherence effects (§ 2.5). Within this framework, and with a realistic band structure model, Friemel *et al.* [190] were able to reproduce the position and anisotropy of the magnetic resonance in $\mathrm{Rb}_x\mathrm{Fe}_{2-y}\mathrm{Se}_2$ assuming a *d*-wave superconducting gap [191] (Fig. 7.3(a)). This model is disputed in some other theoretical work on the $A_x\mathrm{Fe}_{2-y}\mathrm{Se}_2$ systems due to symmetry considerations [192] and the effects of stronger electron correlations than other iron-based superconductors [195–198], but it is supported by others [199–202]. Further theoretical work is needed to understand the magnetic resonance in detail [203], but the results presented here at least establish that the $(0.25, 0.5)$ resonance is present in another

$A_x\mathrm{Fe}_{2-y}\mathrm{Se}_2$ superconductor. This suggests that the resonance could be a characteristic feature of superconductivity in this family. After publication of the results presented in this chapter, the resonance at $(0.25, 0.5)$ was also observed in $\mathrm{K}_x\mathrm{Fe}_{2-y}\mathrm{Se}_2$ [204]. The wavevector, energy, and integrated spectral weight of the magnetic resonance in $\mathrm{K}_x\mathrm{Fe}_{2-y}\mathrm{Se}_2$ are very similar to those found here for $\mathrm{Cs}_x\mathrm{Fe}_{2-y}\mathrm{Se}_2$.

By contrast, I have not found evidence for the magnetic signal reported by Wang *et al.* [193] at $(0, 0.5)$ and equivalent wavevectors in similar measurements on superconducting $\mathrm{Rb}_x\mathrm{Fe}_{2-y}\mathrm{Se}_2$. This affirms that the $A_x\mathrm{Fe}_{2-y}\mathrm{Se}_2$ compounds are distinct from other families of iron-based superconductors.

Finally, it is worthwhile to make some remarks about the absolute intensities of the magnetic features. The scattering intensities of measurements have been given in absolute units of cross-section here for $\mathrm{Cs}_x\mathrm{Fe}_{2-y}\mathrm{Se}_2$, and by Wang *et al.* [193] for $\mathrm{Rb}_x\mathrm{Fe}_{2-y}\mathrm{Se}_2$, which allows comparison of the strengths of the magnetic signals (§ 3.5.5). The amplitude of the spin-wave peak at 14 meV for $\mathrm{Cs}_x\mathrm{Fe}_{2-y}\mathrm{Se}_2$ (Fig. 7.7) is about $55\,\mathrm{mb\,sr}^{-1}\,\mathrm{meV}^{-1}\,\mathrm{f.u.}^{-1}$, which is similar to the amplitude of $\sim 40\,\mathrm{mb\,sr}^{-1}\,\mathrm{meV}^{-1}\,\mathrm{f.u.}^{-1}$ at 10 meV that Wang *et al.* [193] found for $\mathrm{Rb}_x\mathrm{Fe}_{2-y}\mathrm{Se}_2$. The amplitude of the resonance peak in $\mathrm{Cs}_x\mathrm{Fe}_{2-y}\mathrm{Se}_2$, however, is $\sim 2.5\,\mathrm{mb\,sr}^{-1}\,\mathrm{meV}^{-1}\,\mathrm{f.u.}^{-1}$, which is approximately five times larger than that reported for $\mathrm{Rb}_x\mathrm{Fe}_{2-y}\mathrm{Se}_2$. Caution must be taken when comparing peak amplitudes. Nevertheless, it does appear that the resonance peak is more prominent in $\mathrm{Cs}_x\mathrm{Fe}_{2-y}\mathrm{Se}_2$ than in $\mathrm{Rb}_x\mathrm{Fe}_{2-y}\mathrm{Se}_2$. This could indicate an intrinsic difference between the two materials, or that the crystal used here has a higher volume fraction of superconducting phase than that used in Ref. [193].

It is also interesting to compare the strength of the resonance peak with that in other iron-based superconductors. Results for $\chi''(E)$ have been reported previously for $\mathrm{BaFe}_{1.85}\mathrm{Co}_{0.15}\mathrm{As}_2$, $\mathrm{BaFe}_{1.87}\mathrm{Co}_{0.13}\mathrm{As}_2$ and $\mathrm{BaFe}_{1.9}\mathrm{Ni}_{0.1}\mathrm{As}_2$, Refs. [205], [206] and [207], respectively. With the latter two materials, the resonance peak enhancement (i.e. the increase on cooling below T_c) estimated from the presented spectra is 3–$4\,\mu_B{}^2\,\mathrm{eV}^{-1}\,\mathrm{f.u.}^{-1}$ and the enhancement in the energy-integrated signal is $\sim 0.015\,\mu_B{}^2\,\mathrm{f.u.}^{-1}$. The values for $\mathrm{BaFe}_{1.85}\mathrm{Co}_{0.15}\mathrm{As}_2$ are about a factor of two larger [208]. In the case of $\mathrm{Cs}_x\mathrm{Fe}_{2-y}\mathrm{Se}_2$, assuming the $T > T_c$ signal to be about 40 % of that at $T = 4\,\mathrm{K}$ based on the ratio of 44 K to 4 K data shown in the inset to Fig. 7.8(b), the enhancements in the peak and energy-integrated local susceptibilities are $(1.8 \pm 0.5)\,\mu_B{}^2\,\mathrm{eV}^{-1}\,\mathrm{f.u.}^{-1}$ and $(0.009 \pm 0.003)\,\mu_B{}^2\,\mathrm{f.u.}^{-1}$, respectively. These are comparable with the values found for the arsenide superconductors. Since the arsenides were studied near optimal doping they are expected to be bulk superconductors with close to 100 % superconducting volume fraction. This does not, however, necessarily imply that the resonance peak and hence superconductivity in $\mathrm{Cs}_x\mathrm{Fe}_{2-y}\mathrm{Se}_2$ are associated with electrons in most or all of the sample volume. There are several other factors that could influence the size of the resonance peak, e.g. the degree of nesting, strength of magnetic correlations, etc., and these may differ from one material to another. I simply note that the resonance peak in $\mathrm{Cs}_x\mathrm{Fe}_{2-y}\mathrm{Se}_2$ is similar in strength to that in other iron-based superconductors, despite the apparent low volume fraction of superconducting phase, estimated to be $\sim 10\,\%$ [178].

7.6 Conclusions

The measurement of the magnetic dynamics in $Cs_x Fe_{2-y} Se_2$ has provided insight as to the nature of magnetism in the $A_x Fe_{2-y} Se_2$ systems, which is important in the wider context of their relationship with other iron-based superconductors. In contrast to other iron-based systems (Chapters 2 and 4–6), the magnetic spectrum of the superconducting $Cs_{0.8} Fe_{1.9} Se_2$ studied here comprises two components. There is a low-energy resonance-like excitation with wavevector $(0.25, 0.5)$ which responds to superconductivity and is similar in strength to the corresponding feature found in other iron-based superconductors. There are also spin-wave excitations of the block AFM order centred on wavevector $\boldsymbol{Q}_{\mathrm{AFM}} = (0.1, 0.3)$.

I have shown that the spin-wave component of the magnetic scattering closely resembles that of non-superconducting $Rb_x Fe_{2-y} Se_2$. To within experimental error, I found no influence of superconductivity on the low-energy magnetic excitations from the block AFM order, in contrast to the response of the magnetic Bragg peak and a two-magnon Raman peak which both show a small anomaly in intensity on cooling below T_c [158, 181]. The magnetic resonance feature at wavevector $(0.25, 0.5)$, however, does respond to T_c. The observation of this signal in $Cs_x Fe_{2-y} Se_2$ establishes that this feature is not confined to $Rb_x Fe_{2-y} Se_2$, but is present in other members of the $A_x Fe_{2-y} Se_2$ family, confirming this family's place as a new class of iron-based superconductor. An appropriate model of the superconducting pairing state in these materials must explain the magnetic resonance signal at $(0.25, 0.5)$. However, the origin of the resonance and its relationship to the superconducting pairing symmetry remain unresolved [203]. Particular attributes such as the strength of the signal (inset to Fig. 7.8(a)) and the anisotropy of the signal in the H–K-plane (Fig. 7.9) could prove important in understanding the origins of the magnetic resonance [191, 192].

Together with other recent studies, the results presented in this chapter are consistent with a microstructure composed of spatially separate superconducting and non-superconducting domains, with the Fe vacancy superstructure and block antiferromagnetism confined to the non-superconducting phase. It remains a materials challenge to try to maximise the volume fraction of the superconducting phase. Isolation of this phase would allow for further experiments that may help to unravel the physics of the $A_x Fe_{2-y} Se_2$ systems and explain their relationship to other iron-based superconductors.

Magnetic fluctuations in molecular-intercalated FeSe

Contents

8.1 Introduction

In this chapter I discuss another new set of materials that are based on iron-selenide layers. The molecular-intercalated FeSe compounds are synthesised from pure FeSe (an $\sim 8\,\mathrm{K}$ superconductor) by soft chemical techniques that allow molecules, such as ammonia/amide and pyridine, to be included between the FeSe layers [209, 210]. The resulting compounds have T_cs of up to 45 K, notably high among the iron-based superconductors. Given the apparent link between magnetic dynamics and superconductivity in iron-based systems, the character and strength of magnetic fluctuations in these $T_\mathrm{c} \approx 45\,\mathrm{K}$ materials are of great interest.

The inclusion of molecules in addition to alkali metal ions between FeSe layers appears to lengthen the c-axis and promote higher T_cs than ever before seen in FeSe-based systems [209–213]. The synthesis of these compounds uses FeSe as a starting material, and therefore an individual FeSe layer in the product is similar to a layer of pure FeSe (Fig. 2.1). However, the stacking of the layers along the c-axis is similar to $A_x\mathrm{Fe}_{2-y}\mathrm{Se}_2$ systems rather than FeSe (compare Fig. 8.1 with Figs. 2.1 and 7.2(b)). So far, the mechanism for the increased T_c and its relationship with the $\mathrm{FeSe}_{1-x}\mathrm{Te}_x$ and $A_x\mathrm{Fe}_{2-y}\mathrm{Se}_2$ superconductors remains unclear.

The maximum T_c of the $\mathrm{FeSe}_{1-x}\mathrm{Te}_x$ series is $\sim 14.5\,\mathrm{K}$ at ambient pressure [214, 215], rising to nearly 37 K at pressures of 8.9 kbar [216]. Superconductivity has been found up to 30 K in $A_x\mathrm{Fe}_{2-y}\mathrm{Se}_2$ systems at ambient pressure, but only in inhomogeneous samples, making the physics in these materials difficult to unravel (see Chapter 7). A magnetic resonance feature has been observed associated with the superconductivity in both these classes of material. In common with many iron-arsenide superconductors, the magnetic resonance peak of optimally-doped $\mathrm{FeSe}_{1-x}\mathrm{Te}_x$ is found at $\boldsymbol{Q} = (0.5, 0)$ [46], as discussed in § 2.4. The $A_x\mathrm{Fe}_{2-y}\mathrm{Se}_2$ systems, however, have $\boldsymbol{Q}_\mathrm{res} = (0.5, 0.25)$, as shown in Chapter 7. As discussed in previous chapters, these magnetic resonance signals, in conjunction with Fermi-surface data, have been cited as evidence in favour of $s_\pm$ and d-wave pairing states in $\mathrm{FeSe}_{1-x}\mathrm{Te}_x$ and $A_x\mathrm{Fe}_{2-y}\mathrm{Se}_2$, respectively.

It is currently unclear where the molecular-intercalated FeSe systems fit into this picture. Yan and Gao [217] performed Fermi surface calculations for alkali-metal-ion-intercalated FeSe, predicting different crystal structures and very different Fermi surfaces for $T_\mathrm{c} \sim 30\,\mathrm{K}$ and $\sim 40\,\mathrm{K}$ systems. For the latter, they found the electronic structure to be very similar to that of the iron-arsenide systems. The $\mathrm{Li}_x(\mathrm{ND}_2)_y(\mathrm{ND}_3)_{1-y}\mathrm{Fe}_2\mathrm{Se}_2$ system shows $T_\mathrm{c} \approx 43\,\mathrm{K}$, and a diffraction study determined its structure to be consistent with Yan and Gao's 40 K model [210] — note that the alkali metal ion does not occupy the same site in $\mathrm{Li}_x(\mathrm{ND}_2)_y(\mathrm{ND}_3)_{1-y}\mathrm{Fe}_2\mathrm{Se}_2$ as in $A_x\mathrm{Fe}_{2-y}\mathrm{Se}_2$ (compare Fig. 8.1 with 7.2(b)). In addition, μSR measurements on both $\mathrm{Li}_x(\mathrm{NH}_2)_y(\mathrm{NH}_3)_{1-y}\mathrm{Fe}_2\mathrm{Se}_2$ [210] and $\mathrm{Li}_x(\mathrm{C}_5\mathrm{H}_5\mathrm{N})_y\mathrm{Fe}_{2-z}\mathrm{Se}_2$ [218] found that the temperature dependence of the superconducting penetration depth is consistent with an $s_\pm$ model similar to $\mathrm{FeSe}_{1-x}\mathrm{Te}_x$. These results seem to indicate that the molecular-intercalated FeSe systems are similar to $\mathrm{FeSe}_{1-x}\mathrm{Te}_x$, and present different physics to $A_x\mathrm{Fe}_{2-y}\mathrm{Se}_2$. However, experiments with other techniques are needed to piece together a more complete picture of the superconductivity in these high-T_c systems.
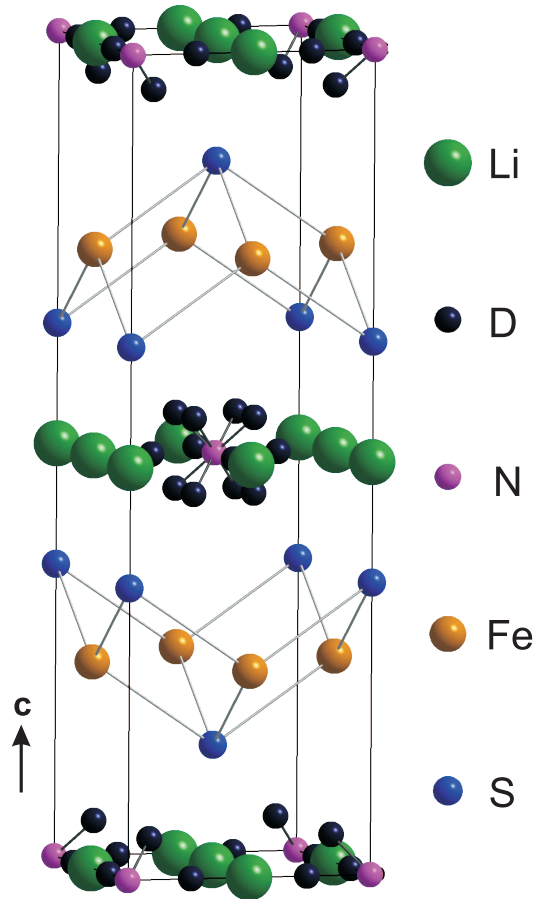
Figure 8.1: Crystal structure of $Li_{0.6}(ND_2)_{0.2}(ND_3)_{0.8}Fe_2Se_2$. The crystal structure of $Li_x(ND_2)_y(ND_3)_{1-y}Fe_2Se_2$ determined from low-temperature (8 K) high-resolution neutron powder diffraction measurements [210]. All sites are shown with full occupancy, although the refined stoichiometry is $Li_{0.6}(ND_2)_{0.2}(ND_3)_{0.8}Fe_2Se_2$. One unit cell with space group symmetry $I4/mmm$ is shown.

If an $s_\pm$ model similar to $FeSe_{1-x}Te_x$ does describe the molecular-intercalated FeSe superconductors, then based on the evidence in Chapters 2 and 5, a magnetic resonance might be expected to appear at $\boldsymbol{Q} = (0.5, 0)$ in the INS spectrum of these materials. Here I present an INS investigation of the molecular-intercalated FeSe superconductor $Li_x(ND_2)_y(ND_3)_{1-y}Fe_2Se_2$ ($T_c = 43\,K$). I set out to answer the questions: (i) are there strong magnetic fluctuations present in the INS spectrum of $Li_x(ND_2)_y(ND_3)_{1-y}Fe_2Se_2$, (ii) at what wavevector do any such magnetic fluctuations appear, and (iii) does the magnetic scattering respond to T_c? The molecular-intercalated FeSe materials are only available as polycrystalline samples, but the results presented in Chapter 5 showed that these questions can be addressed in a polycrystalline INS measurement. I present the results of an experiment on polycrystalline $Li_{0.6}(ND_2)_{0.2}(ND_3)_{0.8}Fe_2Se_2$, and find that strong magnetic fluctuations are present in the INS spectrum. The signal increases with intensity on cooling below T_c, consistent with a magnetic resonance. The observation of magnetic fluctuations helps to establish the material's relationship to other iron-based systems. I discuss what new information this potentially reveals about the superconducting state.

The results presented in this chapter have been published in Ref. [219].

8.2 Synthesis

The molecular-intercalated FeSe materials are prepared via soft chemical techniques and can only be produced in polycrystalline form. Stefan Sedlmaier and Simon Cassidy prepared $Li_x(ND_2)_y(ND_3)_{1-y}Fe_2Se_2$ in the Inorganic Chemistry Laboratory, University of Oxford, UK. The sample was prepared from tetragonal FeSe by the intercalation of lithium and deuterated ammonia between the layers via the route described in Ref. [210]. Deuterated material was used to avoid a large incoherent scattering from protons in the neutron scattering experiments (§ 3.4.3). The crystal structure and typical magnetisation measurements are reported in Ref. [210]. For a sample with $T_c = 43\,K$, Rietveld refinement against high-resolution neutron powder diffraction data revealed a composition $Li_{0.6}(ND_2)_{0.2}(ND_3)_{0.8}Fe_2Se_2$, with lattice parameters $a = 3.8059(1)\,\text{Å}$ and $c = 16.1795(6)\,\text{Å}$ at $8\,K$ for the space group $I4/mmm$ (Fig. 8.1). The results of µSR experiments indicate that the superconducting volume fraction of this material is $\sim 50\,\%$.

In $FeSe_{1-x}Te_x$ systems, interstitial Fe ions (which result in the chemical formula $Fe_{1+\delta}Se_{1-x}Te_x$) have been shown to adversely effect the superconducting properties [220, 221], and to influence the magnetic dynamics [222, 223]. The synthesis technique used to produce $Li_x(ND_2)_y(ND_3)_{1-y}Fe_2Se_2$ is expected to completely remove the interstitial Fe ions from the $Fe_{1+\delta}Se$ used as a starting material, and no evidence for interstitial Fe was found in the final samples [210].

8.3 Experimental set-up

The INS experiments were performed on the MERLIN spectrometer at the ISIS Facility (§ 3.5). 11.4 g of $Li_{0.6}(ND_2)_{0.2}(ND_3)_{0.8}Fe_2Se_2$ powder was sealed inside a cylindrical aluminium can and mounted in a top-loading closed-cycle refrigerator (§ 3.5.6). All handling was carried out in an inert gas atmosphere, and remeasurement of portions of the sample by SQUID magnetometry and x-ray and neutron diffraction confirmed that the sample was unchanged after the experiment. Spectra were recorded with neutrons of incident energy $E_i = 80$ meV and chopper frequencies of 300 and 350 Hz with the sample at temperatures of 5, 30 and 48 K. Additional measurements were made with $E_i = 80$ meV and chopper frequency 350 Hz at temperatures 11, 16, 20, 25, 35, 39, 58 and 67 K. The energy resolution in this configuration was ∼5.5 meV, estimated from the FWHM of the incoherent part of the elastic peak. The presented spectra come from this higher-resolution configuration, and the data have been normalised by the Bose population factor (§ 3.4.6). The scattering from a standard vanadium sample was used to normalise the spectra (§ 3.5.5) and place them on an absolute intensity scale with units $mb\,sr^{-1}\,meV^{-1}\,f.u.^{-1}$, where the f.u. is $Li_{0.6}(ND_2)_{0.2}(ND_3)_{0.8}Fe_2Se_2$.

8.4 Results

Figure 8.2 compares the scattering intensity from $Li_x(ND_2)_y(ND_3)_{1-y}Fe_2Se_2$ at temperatures above and below T_c for three energies between 16 and 28 meV. Runs performed at 58 and 67 K were used for the $T > T_c$ reference data, and were combined in order to improve the statistics. The justification for averaging these runs is that there was no detectable difference between the intensities measured at 58 and 67 K after correction for the Bose population factor (see the inverted triangles in Fig. 8.4).

All three constant-energy cuts shown in Fig. 8.2 exhibit a significant difference between the response at 5 K and at $T > T_c$. The scattering intensity at these energies is expected to be due to inelastic-magnetic and phonon scattering processes, with phonon scattering accounting for the general increase in signal with Q seen in Fig. 8.2 (similar effects are visible in the data from polycrystalline measurements in Chapters 5 and 6). However, within the (Q, E) region shown the Bose factor correction can reasonably be expected to nullify the change in phonon scattering intensity with temperature, so I attribute the extra intensity at 5 K to magnetic scattering.

A clearer picture of the magnetic scattering is provided by Fig. 8.3, which displays the difference between the intensity at 5 K and at $T > T_c$. Each cut contains two peaks, one centred at $Q_1 \approx 1.4$ Å^{-1} and the other at $Q_2 \approx 2$ Å^{-1}. To quantify these peaks I fitted the subtracted data to two Gaussian functions, allowing the width, centre, and amplitude of each Gaussian to vary independently. The fitted centres (Q_i) and widths (σ_i) are given in Table 8.1. In subsequent fits at other temperatures the peak centres and widths were constrained to the values in Table 8.1 and only the areas of the peaks were allowed to vary. This is similar to the fitting procedure used for LiFeAs (§ 5.4).

Figure 8.4 uses the peak area (integrated intensity) as a measure of the strength of the magnetic fluctuations, similar to Fig. 5.8. The areas of the fitted $Q_1 \approx 1.4$ Å^{-1}
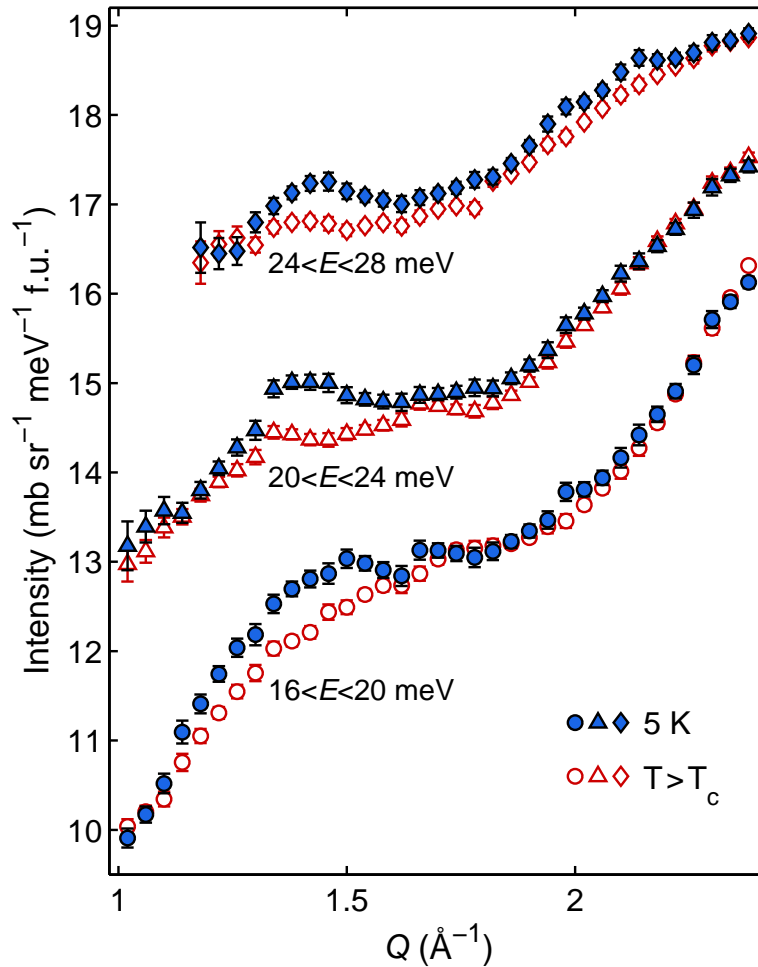
Figure 8.2: INS response of $Li_x(ND_2)_y(ND_3)_{1-y}Fe_2Se_2$. Neutron scattering intensity from polycrystalline $Li_{0.6}(ND_2)_{0.2}(ND_3)_{0.8}Fe_2Se_2$ as a function of wavevector. Data are shown averaged over three energy ranges as indicated, the upper two having being displaced vertically for clarity. The filled blue symbols represent data collected at 5 K, and the open red symbols represent the $T > T_c$ data, a combination of 58 K and 67 K data as described in the text. The intensities have been normalised by the Bose factor $[1 - \exp(-E/k_B T)]^{-1}$. Reprinted figure from A. E. Taylor *et al.*, Phys. Rev. B, **87**, 220508(R), 2013 [219]. Copyright (2013) by the American Physical Society.

Energy (meV)	Q_1 (Å^{-1})	σ_1 (Å^{-1})	Q_2 (Å^{-1})	σ_2 (Å^{-1})
$16 < E < 20$	1.37(2)	0.16(2)	2.03(4)	0.09(4)
$20 < E < 24$	1.42(1)	0.11(1)	1.86(5)	0.15(5)
$24 < E < 28$	1.47(2)	0.13(3)	2.01(4)	0.18(5)

Table 8.1: Results of fitting. Results of fitting two Gaussian functions to the data shown in Fig. 8.3. The best-fit parameters and errors (in brackets) are the result of a least-squares fitting procedure. The Q_i are the Gaussian peak centres and the σ_i are the corresponding standard deviations, where $\sigma = \text{FWHM}/(2\sqrt{2\ln 2})$.
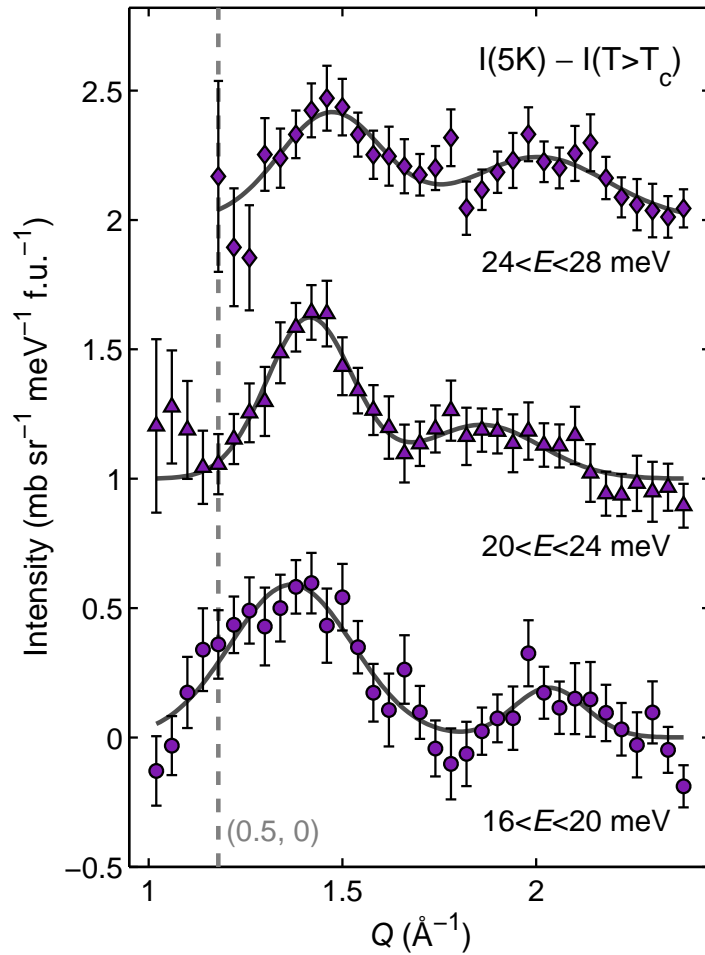
Figure 8.3: Enhancement of the signal at 5 K. Difference between the intensity measured at $T < T_c$ and $T > T_c$ for each pair of constant-energy cuts shown in Fig. 8.2. Successive plots are displaced vertically by one unit for clarity. The solid lines are the results of fits to two Gaussian peaks, as described in the text. The wavevector corresponding to the position $(0.5, 0, 0)$ in momentum space is marked by the dashed line for reference. Reprinted figure from A. E. Taylor *et al.*, Phys. Rev. B, **87**, 220508(R), 2013 [219]. Copyright (2013) by the American Physical Society.
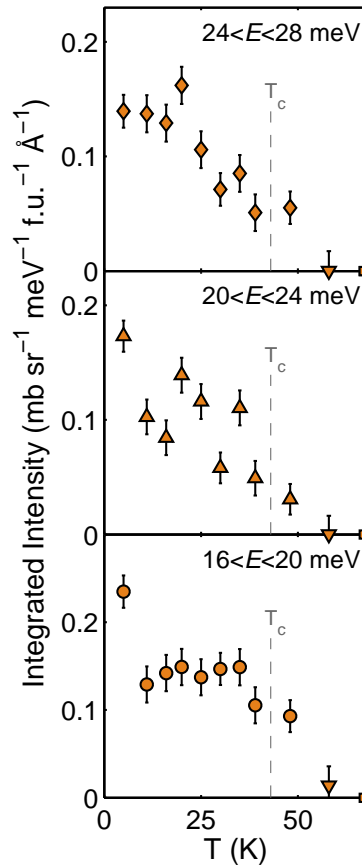
Figure 8.4: Temperature dependence of signal. Integrated intensity of the signal at $Q \approx 1.4\,\text{Å}^{-1}$ as a function of temperature for the three energy ranges indicated. Diamonds, upright triangles and circles all represent results of fits to $I(5\,\text{K}) - I(T > T_c)$, where the $T > T_c$ data is a combination of $58\,\text{K}$ and $67\,\text{K}$ data as described in the text. Inverted triangles are from similar fits to $I(58\,\text{K}) - I(67\,\text{K})$. Square symbols mark the zero reference point at $T = 67\,\text{K}$. Reprinted figure from A. E. Taylor *et al.*, Phys. Rev. B, **87**, 220508(R), 2013 [219]. Copyright (2013) by the American Physical Society.

peaks are plotted as a function of temperature. There is a general trend of increasing area with decreasing temperature below T_c. The data are not of sufficient statistical quality to extract a meaningful trend for the area of the $Q_2 \approx 2\,\text{Å}^{-1}$ peak as a function of temperature, however this peak was included in all fits to avoid attributing excess signal to the lower-Q peak.

8.5 Discussion

In answer to the first question posed in the introduction (§ 8.1), strong magnetic fluctuations do appear to be present in the INS spectrum of $\text{Li}_x(\text{ND}_2)_y(\text{ND}_3)_{1-y}\text{Fe}_2\text{Se}_2$. To interpret the results, however, the powder-averaged Q values of the magnetic peaks need to be related to wavevectors in the BZ, which can pose difficulties, as discussed
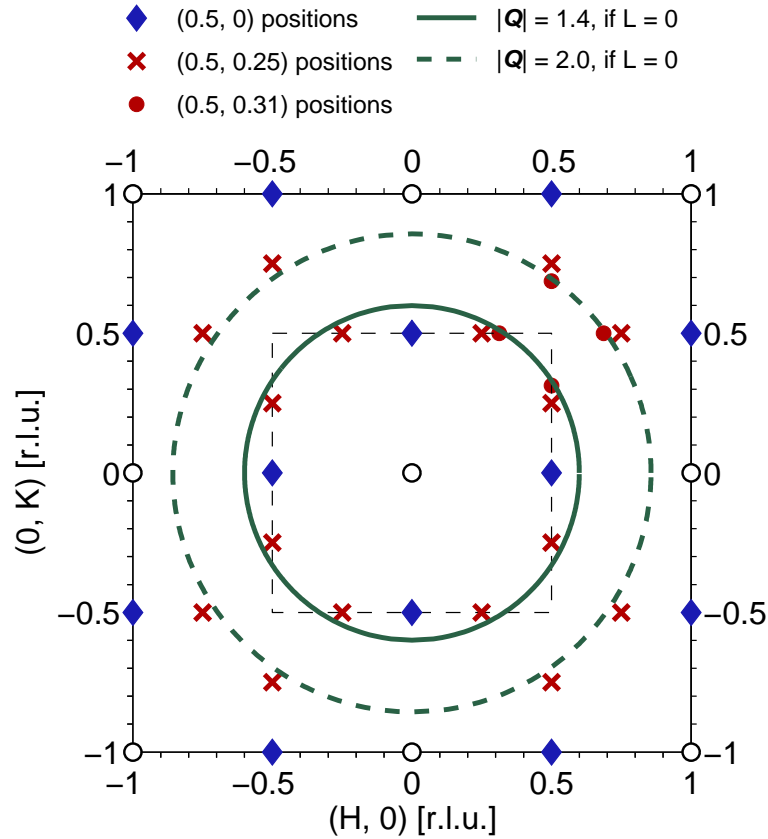
Figure 8.5: Map of reciprocal space. Map of 2D reciprocal space for $Li_x(ND_2)_y(ND_3)_{1-y}Fe_2Se_2$ referred to the one-Fe unit cell. The dashed square marks the first BZ boundary. The solid and dashed rings show the values of Q where magnetic signals are observed in the powder data, if that signal is assumed to have no out-of-plane component. The additional symbols in the upper-right quadrant show the first and second order resonance peak positions predicted in Ref. [191]. Reprinted figure from A. E. Taylor *et al.*, Phys. Rev. B, **87**, 220508(R), 2013 [219]. Copyright (2013) by the American Physical Society.

in § 3.5.4 and § 5.5. Figure 8.5 is a map of the (H, K) plane in 2D reciprocal space. I neglect the out-of-plane wavevector component for now, and I index positions with respect to the one-Fe unit cell which has in-plane lattice parameter $a = b = 2.691$ Å. The map shows the positions of previous observations of a magnetic resonance in iron-based superconductors at $(0.5, 0)$ and $(0.5, 0.25)$. The circles represent the locus of points in the 2D BZ that have $Q = 1.4$ Å^{-1} and 2.0 Å^{-1}, corresponding to the two peak positions in Fig. 8.3.

It is immediately clear from Fig. 8.5 that the wavevector $(0.5, 0)$ and equivalent positions cannot account for the Q_1 and Q_2 values at which magnetic scattering is seen. The wavevector corresponding to $(0.5, 0)$ is also marked on Fig. 8.3 to show that it is displaced away from the maximum of the Q_1 peak. Both $FeSe_{1-x}Te_x$ and $A_xFe_{2-y}Se_2$ show magnetic order in their phase diagrams, therefore the wavevectors

describing those orders are also worth considering. $(0.25, 0.75)$ $[Q = 1.85 \text{Å}^{-1}]$ and equivalent positions describe the magnetic order and fluctuations on the tellurium-rich side of the $\text{FeSe}_{1-x}\text{Te}_x$ phase diagram [224, 225]. Magnetic order and strong magnetic fluctuations are observed at $(0.7, 0.1)$ $[Q = 1.65 \text{Å}^{-1}]$ in the Fe-vacancy-ordered phase of the bi-phasic $A_x\text{Fe}_{2-y}\text{Se}_2$ superconductors (see Fig. 7.5). Neither of these wavevectors account for the magnetic scattering observed in $\text{Li}_{0.6}(\text{ND}_2)_{0.2}(\text{ND}_3)_{0.8}\text{Fe}_2\text{Se}_2$. However, the circles of radius Q_1 and Q_2 pass quite close to the $(0.5, 0.25)$ set of wavevectors and their second order positions $(0.5, 0.75)$, etc., where the resonance is seen in $A_x\text{Fe}_{2-y}\text{Se}_2$ superconductors.

I now consider the effect of the out-of-plane wavevector component, L, on the peak positions. The magnetic fluctuations are likely to be 2D, like those in $\text{FeSe}_{1-x}\text{Te}_x$ and $A_x\text{Fe}_{2-y}\text{Se}_2$ [46, 190], therefore the magnetic signal is expected to be highly extended in the $(0, 0, L)$ direction, as discussed in § 3.5.4. The effect of powder averaging on 2D scattering is to shift the peak to a higher Q than $Q = |(H, K, 0)|$. I estimate this shift from the INS measurements on powder and single crystal samples of LiFeAs that were discussed in Chapter 5 [45, 114]. The magnetic peak in the LiFeAs powder data is at $Q = 1.24 \text{Å}^{-1}$, whereas the in-plane wavevector observed in a single crystal, $(0.5, \pm 0.07)$ [45], has magnitude $Q = 1.19 \text{Å}^{-1}$. This suggests a shift due to powder averaging of $\Delta Q = 0.05 \text{Å}^{-1}$. Applying this correction to the resonance wavevector of $A_x\text{Fe}_{2-y}\text{Se}_2$ results in $Q_{\text{res}} = |(0.5, 0.25, 0)| + \Delta Q = 1.36 \text{Å}^{-1}$, which is close to, but smaller than $Q_1 = 1.4 \text{Å}^{-1}$ observed here.

This analysis suggests that the peak at Q_1 cannot be explained simply by the effect of powder averaging a 2D signal with wavevector $(0.5, 0.25, L)$. This conclusion is supported by the fact that $Q_2 \approx 2.0 \text{Å}^{-1}$ is lower than the value expected from $|(0.5, 0.75, 0)| = 2.10 \text{Å}^{-1}$ (Fig. 8.5). Interestingly, however, the wavevector $\mathbf{Q}_{\text{res}} = (0.5, 0.31)$ predicted from band structure calculations of $A_x\text{Fe}_{2-y}\text{Se}_2$ (Ref. [191]) reproduces both the Q_1 and Q_2 peaks very well, as shown in Fig. 8.5. I will return to this point after discussing other properties of the magnetic scattering.

The temperature dependence of the magnetic peak (Fig. 8.4) is similar to that of resonance peaks observed in other iron-based superconductors including LiFeAs (Fig. 5.8), with an increase in the intensity with decreasing temperature below T_c (or starting slightly above T_c). The lowest temperature point of the $16 < E < 20 \text{ meV}$ data in Fig. 8.4 has an anomalously high integrated intensity, which correlates with an anomalously large peak width (see Table 8.1). Inspection of Figs. 8.2 and 8.3 shows that this increased width appears to be caused by additional intensity on the low-Q side of the peak. The origin of this additional scattering is not known, but one possibility is the presence of a magnetic resonance mode with a wavevector near $(0.5, 0)$. This could originate from a secondary superconducting phase with a T_c of between 5 and 10 K. An impurity of tetragonal FeSe would be a potential secondary phase in $\text{Li}_x(\text{ND}_2)_y(\text{ND}_3)_{1-y}\text{Fe}_2\text{Se}_2$, but x-ray and neutron diffraction measurements on the sample used in this experiment rule out FeSe above the 4 wt % level. Another possible origin would be a two-gap behaviour, as was tentatively suggested by Burrard-Lucas *et al.* [210] for temperatures below ~ 10 K from their μSR data. If present, a second gap could conceivably produce a resonance at $(0.5, 0)$ at lower energies. Unfortunately, the

range of the present data is insufficient to allow further comment.

The magnetic resonance in iron-based superconductors is usually observed over a limited range of energy around $E_r \sim 5k_B T_c$ (§ 2.4). For the $Li_{0.6}(ND_2)_{0.2}(ND_3)_{0.8}Fe_2Se_2$ sample studied here $5k_B T_c \approx 19\,meV$, so the enhancement in intensity observed below T_c in Fig. 8.4 is consistent with a magnetic resonance with $E_r \sim 5k_B T_c$. However, to confirm this it is desirable for future measurements of the spectrum to extend to higher and lower energies than could be probed in this experiment. Energies below $16\,meV$ were contaminated with strong phonon and elastic scattering. At energies above $28\,meV$ the low-Q cut off imposed by the lowest-angle detectors prevents the Q_1 peak from being measured (see Fig. 8.2).

Since the intensity measurements are calibrated, I can again compare the strength of the magnetic signal found here to that observed for other iron-based superconductors. The integrated intensity for the $24 < E < 28\,meV$ wavevector cut at $5\,K$ (Fig. 8.4) is $0.07(1)\,mb\,sr^{-1}\,meV^{-1}\,\text{Å}^{-1}$ per Fe (the f.u. contains two Fe atoms). In the similar powder measurement on superconducting LiFeAs reported in Chapter 5, I found the integrated intensity at the peak energy of the magnetic resonance to be $0.073(5)\,mb\,sr^{-1}\,meV^{-1}\,\text{Å}^{-1}$ per Fe at $6\,K$. This is known to be similar in strength to the signal found in other iron-based superconductors [114, 123], including $A_x Fe_{2-y}Se_2$ [194, 204] (Chapter 7). Therefore, the magnetic signal observed in $Li_x(ND_2)_y(ND_3)_{1-y}Fe_2Se_2$ is consistent in strength with the resonance peaks in other iron-based superconductors.

The observation of resonance-like magnetic peaks is not unexpected, but their positions at Q_1 and Q_2 away from $|(0.5, 0)|$ (see Fig. 8.5) is surprising given the results of μSR [210, 218] and Fermi surface calculations [217] which suggested that these materials are similar to $FeSe_{1-x}Te_x$ and iron-arsenide superconductors. It is also intriguing that, despite similar temperature dependence, energy scale, and absolute intensity, the signal is also not fully explained by $\boldsymbol{Q}_{res} = (0.5, 0.25)$ as observed for $A_x Fe_{2-y}Se_2$, but is very close to an initial prediction made from calculations by Maier *et al.* [191]. $\boldsymbol{Q} = (0.5, 0.31)$ was the position of the resonance originally predicted for $A_x Fe_{2-y}Se_2$ based on a *d*-wave superconducting pairing symmetry (see Ref. [191] and Chapter 7). The resonance was subsequently observed at $\boldsymbol{Q}_{res} = (0.5, 0.25)$ in INS experiments [189], so the calculation was modified[1] by Friemel *et al.* [190] to reproduce the data, as illustrated in Fig. 7.3. If the *d*-wave model is correct, then the observation that the original calculation agrees well with the positions of the Q_1 and Q_2 peaks could be a consequence of slight differences in the detailed band structure of $Li_x(ND_2)_y(ND_3)_{1-y}Fe_2Se_2$ compared with $A_x Fe_{2-y}Se_2$. The results presented in this chapter cannot address this point, but do provide motivation for band structure calculations and theory to understand the nature of superconductivity in this material.

8.6   Conclusions

In this chapter I have reported INS measurements of the magnetic excitation spectrum of $Li_x(ND_2)_y(ND_3)_{1-y}Fe_2Se_2$. These results have been informative as to the nature

---

[1]A rigid band shift was applied to the chemical potential of the bands.

of superconductivity in this material in relation to the $FeSe_{1-x}Te_x$ and $A_xFe_{2-y}Se_2$ systems. A strong magnetic scattering signal was measured at a wavevector $Q \approx$ 1.4 $Å^{-1}$ from a powder sample of the molecular-intercalated FeSe superconductor $Li_{0.6}(ND_2)_{0.2}(ND_3)_{0.8}Fe_2Se_2$. Despite previous evidence in favour of an $s_\pm$ superconducting state [210, 217, 218], the wavevector $\boldsymbol{Q}_{SDW} = (0.5, 0)$ that characterises magnetic fluctuations in several other iron-based superconductors is not consistent with the data.

The wavevector $(0.25, 0.5)$ of the superconducting resonance signal in $A_xFe_{2-y}Se_2$ appears to offer a far better explanation of the data presented, though the match is not perfect. By investigating the temperature dependence and absolute intensity of the signal, as well as noting the energy at which it was observed, I have found that the magnetic scattering in $Li_{0.6}(ND_2)_{0.2}(ND_3)_{0.8}Fe_2Se_2$ is consistent with a superconductivity-induced resonance peak. These results suggest that $Li_x(ND_2)_y(ND_3)_{1-y}Fe_2Se_2$ could be similar to the minority superconducting phase found in $A_xFe_{2-y}Se_2$. The mismatch between the observed wavevectors of the resonance in $Li_x(ND_2)_y(ND_3)_{1-y}Fe_2Se_2$ and $A_xFe_{2-y}Se_2$ might be explained by the d-wave band structure model proposed by Maier *et al.* [191], but the data presented here cannot determine the validity of this model. Since the position of the magnetic resonance has important implications for the symmetry of the pairing function, it is important for band structure calculations and theory to elucidate the nature of superconductivity in the molecular-intercalated FeSe systems.

Conclusions and outlook

In this thesis I have utilised INS to probe the magnetic dynamics in a variety of iron-based materials. The overarching purpose of this research was to explore the interplay between magnetic fluctuations and superconductivity. I began with an investigation of the non-superconducting parent-phase $SrFe_2As_2$ in order to elucidate the nature of magnetism in iron-based systems, and provide a backdrop to subsequent discussions of superconducting materials. I showed that strong magnetic fluctuations associated with the SDW state are present in $SrFe_2As_2$. Importantly, it appears that these fluctuations are best described by a model based on itinerant electron magnetism, not by a localised model. Throughout the rest of this thesis I searched for magnetic fluctuations associated with superconductivity, and discussed them in the context of itinerant magnetism.

Investigating a variety of iron-based superconductors has shown that a magnetic resonance is an almost ubiquitous feature of the INS spectra. This implies a strong link between magnetic dynamics and the superconducting state, despite the fact that magnetic order appears to be detrimental to superconductivity. The materials that were discovered early on, including LiFeAs, revealed a magnetic resonance at, or close to, $\boldsymbol{Q} = \boldsymbol{Q}_{\mathrm{SDW}} = (0.5, 0)$. This highlights the importance of the correlations that cause the static magnetism observed in parent-phase compounds like $SrFe_2As_2$. Newer materials, however, have revealed that the position of the resonance in $\boldsymbol{Q}$-space is not unique, demonstrating that $(0.5, 0)$-type fluctuations are not essential to promoting superconductivity. The observation of a resonance-type signal at $\boldsymbol{Q} = (0.25, 0.5)$, alongside ARPES measurements, has driven models relying on a new Fermi-surface interaction. The results possibly imply that the superconducting pairing state in alkali-metal-containing FeSe-based materials is different to that found in most iron-based superconductors. Further theory and experiments are highly desirable to clarify which gap symmetry describes the systems.

The phosphide materials are a notable exception to the above observations, as no magnetic fluctuations were observed in the INS spectra of LaFePO or Sr_2ScO_3FeP to within experimental error. Having found previously that strong magnetic fluctuations are present in the spectra of both superconducting and non-superconducting materials, the result in the phosphides is an interesting anomaly. It suggests that magnetic fluctuations are not as influential to the electronic properties of the iron-phosphide systems as they are in other iron-based superconductors. This result provides motivation for models to explain the behaviour of the iron-phosphide materials and determine whether superconductivity is mediated by weak spin fluctuations or by a different pairing instability.

While the validity of a link between superconductivity and magnetism in iron-

arsenide and iron-selenide superconductors has been verified, of the compounds discussed in this thesis only LiFeAs naturally fits the model of itinerant magnetism with a localised enhancement due to an $s_\pm$ gap. It is clear from the results presented in this thesis that current models of iron-based systems do not adequately describe all of the materials.

The work on $SrFe_2As_2$ in particular highlights that the microscopic origins of magnetism are still not well understood. While an itinerant model provided the best match to the data, there remain open questions about the degree of itinerancy versus localised magnetism. The $A_xFe_{2-y}Se_2$ systems show that localised magnetism can be present in the phase diagram of an iron-based superconductor, whereas the phosphide materials seem to host weaker electronic correlations. It is important to understand the microscopic origins of magnetism and the strength of correlations in these systems if a complete understanding of the relationship between superconductivity and magnetism is to be achieved.

The FeSe-based materials investigated in this thesis highlight the role that chemistry and materials development have to play in furthering the understanding of iron-based superconductors. The discovery of new materials, in conjunction with INS experiments, has directly led to the development of new models that attempt to describe superconductivity in these systems.

There are a number of directions for future work that could help to elucidate the interactions in the materials I have discussed in this thesis. It would be valuable to compare the data from $SrFe_2As_2$ to itinerant models that go beyond the mean field approximation. These models should be based on the experimentally determined band structure, which has now been measured in both ARPES and quantum oscillations experiments. Additionally, it would be helpful to clarify whether any models based on nematic fluctuations can accurately reproduce the anisotropy in the magnetic spectrum up to room temperature. Ultimately, models based on a combination of, or intermediate between, itinerant and localised interactions may be required to fully describe the data. It would be highly desirable to repeat INS experiments on detwinned samples of $SrFe_2As_2$, so that the a–b anisotropy can be fully examined. XFe_2As_2 systems can be detwinned by application of pressure, but, due to limitations caused by placing bulky pressure apparatus in the neutron beam, this sort of experiment would be very difficult to perform currently. As an alternative, resonant inelastic x-ray scattering could be used to probe the magnetic dynamics in this system, and it feasible that a pressure cell could be used in such an experiment.

In the case of LiFeAs, subsequent to the work presented in this thesis, single crystals became available. This allowed further INS experiments that helped to confirm the presence of a magnetic resonance and verify its position in reciprocal space. However, some open questions remain. The properties of this system seem to be very sensitive to doping and substitution of Li by Fe. Performing ARPES and INS measurements on the same single crystals (or perhaps crystals from the same batch) would give a more detailed picture of how the magnetic scattering evolves with changes to the Fermi surface. This could help to resolve the question regarding the size of the normal-state spin gap, and why it varies greatly between non-superconducting and superconducting

single crystals.

An important next step in the study of iron phosphides is to determine the composition of the superconducting phase in the Sr_2ScO_3FeP system. It is desirable to do a complete study of the chemistry in this system, and attempt to make pure bulk-superconducting samples. In the seemingly non-superconducting stoichiometric phase, as well as in superconducting samples, a full analysis of the composition of the phases should be performed, using high-intensity, high-resolution combined neutron and x-ray diffraction, and microstructural analysis techniques. Further INS experiments might also be helpful in these materials, particularly if single-phase bulk superconducting Sr_2ScO_3FeP can be produced, as a magnetic resonance might still be found. A polarised neutron scattering experiment would ensure that any magnetic scattering can be isolated from the background, but given that any fluctuations are apparently very weak in these systems, the loss of intensity inherent in any such measurement may mean this technique would not improve on the results presented here.

A first step in further investigation of $Cs_xFe_{2-y}Se_2$ would be INS experiments to gain better resolution on the measurement of the anisotropy of the resonance peak. This could be performed using a triple axis spectrometer that would allow a higher-intensity measurement than that reported here. This is important because an anisotropy is measured in both $Rb_xFe_{2-y}Se_2$ and $K_xFe_{2-y}Se_2$ systems, and is reproduced in the model based on a d-wave superconducting gap. Confirming the degree of anisotropy of the resonance in $Cs_xFe_{2-y}Se_2$ would be most useful in conjunction with detailed Fermi surface measurements. This would allow determination of whether the degree of anisotropy is consistent with the structure of the electron pockets in this system, and help to clarify the importance of the electron pocket interactions.

In the molecular intercalated-FeSe system it would be useful to extend the INS measurements to higher and lower energies in order to confirm whether the scattering is peaked in energy, as would be expected from a magnetic resonance. In this case, given the strong scattering observed, a polarised neutron scattering experiment might be feasible and would be useful. This would allow the gap in the magnetic excitation spectrum to be determined by eliminating the problem of high contamination from nuclear scattering at low energies that I encountered. This would also provide unambiguous confirmation of the magnetic nature of the peak at $Q \approx 2\,\text{Å}^{-1}$, and, as it would remove uncertainty in the background, it would allow for a clearer determination of the centre of this peak (although still within the limits of a powder measurement). Polarised neutron scattering would also resolve whether the anomaly I observed at low temperature and low energy is due to magnetic scattering.

There are many other routes that are likely to provide more detailed information on the magnetic resonance and its origins in iron-based superconductors. For example, INS studies of features of the magnetic resonance such as its dispersion, its magnetic field dependence, and its detailed evolution as the superconducting gap opens, are all still in relatively early stages. Developments in these areas are likely to drive theory, and ultimately rule out particular models of the origins of the magnetic resonance.

The results of INS experiments, including the results presented in this thesis, have already had a high impact in the field of iron-based superconductors. They have driven

forward theoretical models by demonstrating a link between magnetic fluctuations and T_c, and have provided clues as to the superconducting gap symmetries in the materials. It is clear that comparison of INS results to theoretical models can provide valuable information about both superconductivity and magnetism, but many open questions remain in this field. Both theory and experiment must continue to advance for the role of magnetism in both promoting and destroying superconductivity to be understood.

Bibliography

[1] H. K. Onnes, Further experiments with liquid helium: On the sudden change in the rate at which the resistance of mercury disappears, *Commun. Phys. Lab. Univ. Leiden* **124** (1911).

[2] W. Meissner and R. Ochsenfeld, Ein neuer Effekt bei Eintritt der Supraleit-fähigkeit, *Naturwissenschaften* **21**, 44, 787–788 (1933).

[3] J. Bardeen, L. N. Cooper and J. R. Schrieffer, Theory of Superconductivity, *Phys. Rev.* **108**, 1175–1204 (1957).

[4] F. Steglich, J. Aarts, C. D. Bredl, W. Lieke, D. Meschede, W. Franz and H. Schäfer, Superconductivity in the Presence of Strong Pauli Paramagnetism: $CeCu_2Si_2$, *Phys. Rev. Lett.* **43**, 1892–1896 (1979).

[5] J. G. Bednorz and K. A. Müller, Possible high T_c superconductivity in the Ba–La–Cu–O system, *Z. Phys. B Con. Mat.* **64**, 2 (1986).

[6] M. K. Wu, J. R. Ashburn, C. J. Torng, P. H. Hor, R. L. Meng, L. Gao, Z. J. Huang, Y. Q. Wang and C. W. Chu, Superconductivity at $93\,K$ in a new mixed-phase Y–Ba–Cu–O compound system at ambient pressure, *Phys. Rev. Lett.* **58**, 908–910 (1987).

[7] N. P. Armitage, P. Fournier and R. L. Greene, Progress and perspectives on electron-doped cuprates, *Rev. Mod. Phys.* **82**, 2421–2487 (2010).

[8] C. Varma, High-temperature superconductivity: Mind the pseudogap, *Nature* **468**, 184–185 (2010).

[9] D. J. Scalapino, A common thread: The pairing interaction for unconventional superconductors, *Rev. Mod. Phys.* **84**, 1383–1417 (2012).

[10] M. R. Norman and C. Pépin, The electronic nature of high temperature cuprate superconductors, *Rep. Prog. Phys.* **66**, 10, 1547 (2003).

[11] J. M. Tranquada, Neutron Scattering Studies of Antiferromagnetic Correlations in Cuprates, *arXiv:cond-mat/0512115* (2005).

[12] M. Vojta, Lattice symmetry breaking in cuprate superconductors: stripes, nematics, and superconductivity, *Adv. Phys.* **58**, 6, 699–820 (2009).

[13] J. Rossat-Mignod, L. Regnault, C. Vettier, P. Bourges, P. Burlet, J. Bossy, J. Henry and G. Lapertot, Neutron scattering study of the $YBa_2Cu_3O_{6+x}$ system, *Physica C* **185–189**, 86–92 (1991).

[14] Y. Kamihara, T. Watanabe, M. Hirano and H. Hosono, Iron-Based Layered Superconductor La[$O_{1-x}F_x$]FeAs (x = 0.05–0.12) with T_c = 26 K, *J. Am. Chem. Soc.* **130**, 11, 3296–3297 (2008).

[15] D. C. Johnston, The puzzle of high temperature superconductivity in layered iron pnictides and chalcogenides, *Adv. Phys.* **59**, 6, 803–1061 (2010).

[16] C. de la Cruz, Q. Huang, J. W. Lynn, J. Li, W. R. Ii, J. L. Zarestky, H. A. Mook, G. F. Chen, J. L. Luo, N. L. Wang and P. Dai, Magnetic order close to superconductivity in the iron-based layered $LaO_{1-x}F_x$FeAs systems, *Nature* **453**, 7197, 899–902 (2008).

[17] C. Wang, L. Li, S. Chi, Z. Zhu, Z. Ren, Y. Li, Y. Wang, X. Lin, Y. Luo, S. Jiang, X. Xu, G. Cao and Z. Xu, Thorium-doping-induced superconductivity up to 56 K in $Gd_{1-x}Th_x$FeAsO, *Europhys. Lett.* **83**, 6, 67006 (2008).

[18] W. Qing-Yan, L. Zhi, Z. Wen-Hao *et al.*, Interface-Induced High-Temperature Superconductivity in Single Unit-Cell FeSe Films on $SrTiO_3$, *Chinese Phys. Lett.* **29**, 3, 037402 (2012).

[19] S. He, J. He, W. Zhang *et al.*, Phase diagram and electronic indication of high-temperature superconductivity at 65 K in single-layer FeSe films, *Nat. Mater.* **12**, 7, 605–610 (2013).

[20] M. Rotter, M. Tegel and D. Johrendt, Superconductivity at 38 K in the Iron Arsenide $(Ba_{1-x}K_x)Fe_2As_2$, *Phys. Rev. Lett.* **101**, 107006 (2008).

[21] Q. Huang, J. Zhao, J. W. Lynn, G. F. Chen, J. L. Luo, N. L. Wang and P. Dai, Doping evolution of antiferromagnetic order and structural distortion in $LaFeAsO_{1-x}F_x$, *Phys. Rev. B* **78**, 054529 (2008).

[22] M. Rotter, M. Tegel, D. Johrendt, I. Schellenberg, W. Hermes and R. Pöttgen, Spin-density-wave anomaly at 140 K in the ternary iron arsenide $BaFe_2As_2$, *Phys. Rev. B* **78**, 020503 (2008).

[23] J. Paglione and R. L. Greene, High-temperature superconductivity in iron-based materials, *Nature Phys.* **6**, 9, 645–658 (2010).

[24] M. D. Lumsden and A. D. Christianson, Magnetism in Fe-based superconductors, *J. Phys.: Condens. Matter* **22**, 20, 203203 (2010).

[25] P. Dai, J. Hu and E. Dagotto, Magnetism and its microscopic origin in iron-based high-temperature superconductors, *Nature Phys.* **8**, 10, 709–718 (2012).

[26] J. T. Park, D. S. Inosov, A. Yaresko *et al.*, Symmetry of spin excitation spectra in the tetragonal paramagnetic and superconducting phases of 122-ferropnictides, *Phys. Rev. B* **82**, 134503 (2010).

[27] H. Chen, Y. Ren, Y. Qiu, W. Bao, R. H. Liu, G. Wu, T. Wu, Y. L. Xie, X. F. Wang, Q. Huang and X. H. Chen, Coexistence of the spin-density wave and superconductivity in $Ba_{1-x}K_xFe_2As_2$, *Europhys. Lett.* **85**, 1 (2009).

[28] J. D. Wright, T. Lancaster, I. Franke, A. J. Steele, J. S. Möller, M. J. Pitcher, A. J. Corkett, D. R. Parker, D. G. Free, F. L. Pratt, P. J. Baker, S. J. Clarke and S. J. Blundell, Gradual destruction of magnetism in the superconducting family $NaFe_{1-x}Co_xAs$, *Phys. Rev. B* **85**, 054503 (2012).

[29] Y. Laplace, J. Bobroff, F. Rullier-Albenque, D. Colson and A. Forget, Atomic coexistence of superconductivity and incommensurate magnetic order in the pnictide $Ba(Fe_{1-x}Co_x)_2As_2$, *Phys. Rev. B* **80**, 140501 (2009).

[30] D. K. Pratt, W. Tian, A. Kreyssig, J. L. Zarestky, S. Nandi, N. Ni, S. L. Bud'ko, P. C. Canfield, A. I. Goldman and R. J. McQueeney, Coexistence of Competing Antiferromagnetic and Superconducting Phases in the Underdoped $Ba(Fe_{0.953}Co_{0.047})_2As_2$ Compound Using X-ray and Neutron Scattering Techniques, *Phys. Rev. Lett.* **103**, 087001 (2009).

[31] E. Wiesenmayer, H. Luetkens, G. Pascua, R. Khasanov, A. Amato, H. Potts, B. Banusch, H.-H. Klauss and D. Johrendt, Microscopic Coexistence of Superconductivity and Magnetism in $Ba_{1-x}K_xFe_2As_2$, *Phys. Rev. Lett.* **107**, 237001 (2011).

[32] S. Blundell, Magnetism in Condensed Matter. (Oxford University Press, Oxford) (2001).

[33] K. Yosida, Theory of Magnetism (Springer, Berlin; New York) (1996).

[34] P. Mohn, Magnetism in the Solid State: An Introduction (Springer, Berlin; New York) (2006).

[35] Y. Ishikawa, G. Shirane, J. A. Tarvin and M. Kohgi, Magnetic excitations in the weak itinerant ferromagnet MnSi, *Phys. Rev. B* **16**, 4956 (1977).

[36] H. A. Mook, R. M. Nicklow, E. D. Thompson and M. K. Wilkinson, Spin-Wave Spectrum of Nickel Metal, *J. Appl. Phys.* **40**, 3, 1450 (1969).

[37] H. A. Mook and R. M. Nicklow, Neutron Scattering Investigation of the Magnetic Excitations in Iron, *Phys. Rev. B* **7**, 336–342 (1973).

[38] R. A. Ewings, T. G. Perring, R. I. Bewley, T. Guidi, M. J. Pitcher, D. R. Parker, S. J. Clarke and A. T. Boothroyd, High-energy spin excitations in $BaFe_2As_2$ observed by inelastic neutron scattering, *Phys. Rev. B* **78**, 220501 (2008).

[39] M. Ishikado, R. Kajimoto, S.-i. Shamoto, M. Arai, A. Iyo, K. Miyazawa, P. M. Shirage, H. Kito, H. Eisaki, S. Kim, H. Hosono, T. Guidi, R. Bewley and S. M. Bennington, Two-Dimensional Spin Density Wave State in LaFeAsO, *J. Phys. Soc. Jpn.* **78**, 4, 043705 (2009).

[40] A. Christianson, E. A. Goremychkin, R. Osborn, S. Rosenkranz, M. D. Lumsden, C. D. Malliakas, I. S. Todorov, H. Claus, D. Y. Chung, M. G. Kanatzidis, R. I. Bewley and T. Guidi, Unconventional superconductivity in $Ba_{0.6}K_{0.4}Fe_2As_2$ from inelastic neutron scattering, *Nature* **456**, 7224, 930–932 (2008).

[41] C. Stock, C. Broholm, Y. Zhao, F. Demmel, H. J. Kang, K. C. Rule and C. Petrovic, Magnetic Field Splitting of the Spin Resonance in $CeCoIn_5$, *Phys. Rev. Lett.* **109**, 167207 (2012).

[42] G. Yu, Y. Li, E. M. Motoyama and M. Greven, A universal relationship between magnetic resonance and superconducting gap in unconventional superconductors, *Nature Phys.* **5**, 12, 873–875 (2009).

[43] S. Chi, A. Schneidewind, J. Zhao, L. W. Harriger, L. Li, Y. Luo, G. Cao, Z. Xu, M. Loewenhaupt, J. Hu and P. Dai, Inelastic Neutron-Scattering Measurements of a Three-Dimensional Spin Resonance in the FeAs-Based $BaFe_{1.9}Ni_{0.1}As_2$ Superconductor, *Phys. Rev. Lett.* **102**, 107006 (2009).

[44] M. D. Lumsden, A. D. Christianson, D. Parshall *et al.*, Two-dimensional resonant magnetic excitation in $BaFe_{1.84}Co_{0.16}As_2$, *Phys. Rev. Lett.* **102**, 107005 (2009).

[45] N. Qureshi, P. Steffens, Y. Drees, A. C. Komarek, D. Lamago, Y. Sidis, L. Harnagea, H.-J. Grafe, S. Wurmehl, B. Büchner and M. Braden, Inelastic Neutron-Scattering Measurements of Incommensurate Magnetic Excitations on Superconducting LiFeAs Single Crystals, *Phys. Rev. Lett.* **108**, 117001 (2012).

[46] Y. Qiu, W. Bao, Y. Zhao, C. Broholm, V. Stanev, Z. Tesanovic, Y. C. Gasparovic, S. Chang, J. Hu, B. Qian, M. Fang and Z. Mao, Spin Gap and Resonance at the Nesting Wave Vector in Superconducting $FeSe_{0.4}Te_{0.6}$, *Phys. Rev. Lett.* **103**, 067008 (2009).

[47] I. Mazin and J. Schmalian, Pairing symmetry and pairing state in ferropnictides: Theoretical overview, *Physica C: Supercond.* **469**, 9–12, 614–627 (2009).

[48] S. Li and P. Dai, Superconductivity and spin fluctuations, *Front. Phys.* **6**, 4, 429–439 (2011).

[49] G. R. Stewart, Superconductivity in iron compounds, *Rev. Mod. Phys.* **83**, 1589–1652 (2011).

[50] D. Singh, Electronic structure of Fe-based superconductors, *Physica C: Supercond.* **469**, 9–12, 418–424 (2009).

[51] A. I. Coldea, J. D. Fletcher, A. Carrington, J. G. Analytis, A. F. Bangura, J.-H. Chu, A. S. Erickson, I. R. Fisher, N. E. Hussey and R. D. McDonald, Fermi Surface of Superconducting LaFePO Determined from Quantum Oscillations, *Phys. Rev. Lett.* **101**, 216402 (2008).

[52] T. Kondo, A. F. Santander-Syro, O. Copie, C. Liu, M. E. Tillman, E. D. Mun, J. Schmalian, S. L. Bud'ko, M. A. Tanatar, P. C. Canfield and A. Kaminski, Momentum Dependence of the Superconducting Gap in $NdFeAsO_{0.9}F_{0.1}$ Single Crystals Measured by Angle Resolved Photoemission Spectroscopy, *Phys. Rev. Lett.* **101**, 147003 (2008).

[53] D. S. Inosov, J. S. White, D. V. Evtushinsky *et al.*, Weak Superconducting Pairing and a Single Isotropic Energy Gap in Stoichiometric LiFeAs, *Phys. Rev. Lett.* **104**, 187001 (2010).

[54] K. Nakayama, T. Sato, P. Richard, T. Kawahara, Y. Sekiba, T. Qian, G. F. Chen, J. L. Luo, N. L. Wang, H. Ding and T. Takahashi, Angle-Resolved Photoemission Spectroscopy of the Iron-Chalcogenide Superconductor $Fe_{1.03}Te_{0.7}Se_{0.3}$: Strong Coupling Behavior and the Universality of Interband Scattering, *Phys. Rev. Lett.* **105**, 197001 (2010).

[55] Y. Xia, D. Qian, L. Wray, D. Hsieh, G. F. Chen, J. L. Luo, N. L. Wang and M. Z. Hasan, Fermi Surface Topology and Low-Lying Quasiparticle Dynamics of Parent $Fe_{1+x}Te/Se$ Superconductor, *Phys. Rev. Lett.* **103**, 037002 (2009).

[56] H. Ding, P. Richard, K. Nakayama *et al.*, Observation of Fermi-surface-dependent nodeless superconducting gaps in $Ba_{0.6}K_{0.4}Fe_2As_2$, *Europhys. Lett.* **83**, 4, 47001 (2008).

[57] P. Vilmercati, A. Fedorov, I. Vobornik, U. Manju, G. Panaccione, A. Goldoni, A. S. Sefat, M. A. McGuire, B. C. Sales, R. Jin, D. Mandrus, D. J. Singh and N. Mannella, Evidence for three-dimensional Fermi-surface topology of the layered electron-doped iron superconductor $Ba(Fe_{1-x}Co_x)_2As_2$, *Phys. Rev. B* **79**, 220503 (2009).

[58] P. J. Hirschfeld, M. M. Korshunov and I. I. Mazin, Gap symmetry and structure of Fe-based superconductors, *Rep. Prog. Phys.* **74**, 12, 124508 (2011).

[59] M. R. Norman, Relation of neutron incommensurability to electronic structure in high-temperature superconductors, *Phys. Rev. B* **61**, 14751 (2000).

[60] J.-P. Castellan, S. Rosenkranz, E. A. Goremychkin *et al.*, Effect of Fermi Surface Nesting on Resonant Spin Excitations in $Ba_{1-x}K_xFe_2As_2$, *Phys. Rev. Lett.* **107**, 177003 (2011).

[61] T. A. Maier and D. J. Scalapino, Theory of neutron scattering as a probe of the superconducting gap in the iron pnictides, *Phys. Rev. B* **78**, 020514 (2008).

[62] I. I. Mazin, D. J. Singh, M. D. Johannes and M. H. Du, Unconventional Superconductivity with a Sign Reversal in the Order Parameter of $LaFeAsO_{1-x}F_x$, *Phys. Rev. Lett.* **101**, 057003 (2008).

[63] A. Chubukov, Renormalization group analysis of competing orders and the pairing symmetry in Fe-based superconductors, *Physica C: Supercond.* **469**, 9–12, 640–650 (2009).

[64] R. Thomale, C. Platt, W. Hanke, J. Hu and B. A. Bernevig, Exotic d-Wave Superconducting State of Strongly Hole-Doped $K_xBa_{1-x}Fe_2As_2$, *Phys. Rev. Lett.* **107**, 117001 (2011).

[65] S. Maiti, M. M. Korshunov, T. A. Maier, P. J. Hirschfeld and A. V. Chubukov, Evolution of symmetry and structure of the gap in iron-based superconductors with doping and interactions, *Phys. Rev. B* **84**, 224505 (2011).

[66] M. M. Korshunov and I. Eremin, Theory of magnetic excitations in iron-based layered superconductors, *Phys. Rev. B* **78**, 140509 (2008).

[67] T. Saito, S. Onari and H. Kontani, Orbital fluctuation theory in iron pnictides: Effects of As-Fe-As bond angle, isotope substitution, and Z^2-orbital pocket on superconductivity, *Phys. Rev. B* **82**, 144510 (2010).

[68] H. Kontani and S. Onari, Orbital-Fluctuation-Mediated Superconductivity in Iron Pnictides: Analysis of the Five-Orbital Hubbard-Holstein Model, *Phys. Rev. Lett.* **104**, 157001 (2010).

[69] S. Onari, H. Kontani and M. Sato, Structure of neutron-scattering peaks in both s_{++}-wave and $s_\pm$-wave states of an iron pnictide superconductor, *Phys. Rev. B* **81**, 060504 (2010).

[70] S. Onari and H. Kontani, Neutron inelastic scattering peak by dissipationless mechanism in the s_{++}-wave state in iron-based superconductors, *Phys. Rev. B* **84**, 144518 (2011).

[71] D. J. Singh and M.-H. Du, Density Functional Study of $LaFeAsO_{1-x}F_x$: A Low Carrier Density Superconductor Near Itinerant Magnetism, *Phys. Rev. Lett.* **100**, 237003 (2008).

[72] A. C. Larson and R. B. Von Dreele, General Structure Analysis System (GSAS) (1994).

[73] B. H. Toby, EXPGUI, a graphical user interface for GSAS, *J. Appl. Crystallogr.* **34**, 2, 210–213 (2001).

[74] T. Chatterji, Neutron Scattering from Magnetic Materials (Elsevier, Oxford) (2006).

[75] G. L. Squires, Introduction to the Theory of Thermal Neutron Scattering (Dover, Mineola, New York) (1996).

[76] D. Sivia, Elementary Scattering Theory (Oxford University Press, Oxford) (2011).

[77] B. Willis and C. Carlile, Experimental neutron scattering (Oxford University Press, Oxford) (2009).

[78] V. F. Sears, Neutron scattering lengths and cross sections, *Neutron News* **3**, 26–37 (1992).

[79] A.-J. Dianoux and G. Lander, Neutron Data Booklet (Institut Laue-Langevin), 2nd ed. (2003).

[80] R. Bewley, R. Eccleston, K. McEwen, S. Hayden, M. Dove, S. Bennington, J. Treadgold and R. Coleman, MERLIN, a new high count rate spectrometer at ISIS, *Physica B: Condens. Matter* **385–386**, 1029–1031 (2006).

[81] J. Ollivier and H. Mutka, IN5 Cold Neutron Time-of-Flight Spectrometer, Prepared to Tackle Single Crystal Spectroscopy, *J. Phys. Soc. Jpn.* **80**, Supplement B, SB003 (2011).

[82] For more information on Homer see the following websites: `http://www.libisis.org/Using_Homer_and_Getting_Started` and `http://www.mantidproject.org/Homer`.

[83] Q. Si and E. Abrahams, Strong Correlations and Magnetic Frustration in the High T_c Iron Pnictides, *Phys. Rev. Lett.* **101**, 076401 (2008).

[84] S. O. Diallo, V. P. Antropov, T. G. Perring, C. Broholm, J. J. Pulikkotil, N. Ni, S. L. Bud'ko, P. C. Canfield, A. Kreyssig, A. I. Goldman and R. J. McQueeney, Itinerant Magnetic Excitations in Antiferromagnetic $CaFe_2As_2$, *Phys. Rev. Lett.* **102**, 187206 (2009).

[85] J. Zhao, D. T. Adroja, D.-X. Yao, R. Bewley, S. Li, X. F. Wang, G. Wu, X. H. Chen, J. Hu and P. Dai, Spin waves and magnetic exchange interactions in $CaFe_2As_2$, *Nature Phys.* **5**, 8, 555–560 (2009).

[86] C. Fang, H. Yao, W.-F. Tsai, J. Hu and S. A. Kivelson, Theory of electron nematic order in LaFeAsO, *Phys. Rev. B* **77**, 224509 (2008).

[87] C.-C. Chen, B. Moritz, J. van den Brink, T. P. Devereaux and R. R. P. Singh, Finite-temperature spin dynamics and phase transitions in spin-orbital models, *Phys. Rev. B* **80**, 180418 (2009).

[88] J.-H. Chu, J. G. Analytis, K. D. Greve, P. L. McMahon, Z. Islam, Y. Yamamoto and I. R. Fisher, In-Plane Resistivity Anisotropy in an Underdoped Iron Arsenide Superconductor, *Science* **329**, 5993, 824–826 (2010).

[89] J. Zhao, D.-X. Yao, S. Li, T. Hong, Y. Chen, S. Chang, W. Ratcliff, J. W. Lynn, H. A. Mook, G. F. Chen, J. L. Luo, N. L. Wang, E. W. Carlson, J. Hu and P. Dai, Low Energy Spin Waves and Magnetic Interactions in $SrFe_2As_2$, *Phys. Rev. Lett.* **101**, 167203 (2008).

[90] R. A. Ewings, T. G. Perring, J. Gillett, S. D. Das, S. E. Sebastian, A. E. Taylor, T. Guidi and A. T. Boothroyd, Itinerant spin excitations in $SrFe_2As_2$ measured by inelastic neutron scattering, *Phys. Rev. B* **83**, 214519 (2011).

[91] J. Gillett, S. D. Das, P. Syers, A. K. T. Ming, J. I. Espeso, C. M. Petrone and S. E. Sebastian, Dimensional Tuning of the Magnetic-Structural Transition in $A(Fe_{1-x}Co_x)_2As_2$ (A=Sr,Ba), *arXiv:1005.1330* (2010).

[92] S. E. Sebastian, J. Gillett, N. Harrison, P. H. C. Lau, D. J. Singh, C. H. Mielke and G. G. Lonzarich, Quantum oscillations in the parent magnetic phase of an iron arsenide high temperature superconductor, *J. Phys.: Condens. Matter* **20**, 42, 422203 (2008).

[93] M. Tegel, M. Rotter, V. Weiß, F. M. Schappacher, R. Pöttgen and D. Johrendt, Structural and magnetic phase transitions in the ternary iron arsenides $SrFe_2As_2$ and $EuFe_2As_2$, *J. Phys.: Condens. Matter* **20**, 45, 452201 (2008).

[94] E. Kaneshita and T. Tohyama, Spin and charge dynamics ruled by antiferromagnetic order in iron pnictide superconductors, *Phys. Rev. B* **82**, 094441 (2010).

[95] T. G. Perring *et al.*, see: http://tobyfit.isis.rl.ac.uk.

[96] R. M. Fernandes, L. H. VanBebber, S. Bhattacharya, P. Chandra, V. Keppens, D. Mandrus, M. A. McGuire, B. C. Sales, A. S. Sefat and J. Schmalian, Effects of Nematic Fluctuations on the Elastic Properties of Iron Arsenide Superconductors, *Phys. Rev. Lett.* **105**, 157003 (2010).

[97] J. Knolle, I. Eremin, A. V. Chubukov and R. Moessner, Theory of itinerant magnetic excitations in the spin-density-wave phase of iron-based superconductors, *Phys. Rev. B* **81**, 140506 (2010).

[98] W. Lv, F. Krüger and P. Phillips, Orbital ordering and unfrustrated $(\pi, 0)$ magnetism from degenerate double exchange in the iron pnictides, *Phys. Rev. B* **82**, 045125 (2010).

[99] A. A. Kordyuk, Iron-based superconductors: Magnetism, superconductivity, and electronic structure (Review Article), *Low Temp. Phys.* **38**, 9, 888–899 (2012).

[100] J. H. Tapp, Z. Tang, B. Lv, K. Sasmal, B. Lorenz, P. C. W. Chu and A. M. Guloy, LiFeAs: An intrinsic FeAs-based superconductor with T_c=18 K, *Phys. Rev. B* **78**, 060505 (2008).

[101] M. J. Pitcher, D. R. Parker, P. Adamson, S. J. C. Herkelrath, A. T. Boothroyd, R. M. Ibberson, M. Brunelli and S. J. Clarke, Structure and superconductivity of LiFeAs, *Chem. Commun.* **45**, 5918–5920 (2008).

[102] X. Wang, Q. Liu, Y. Lv, W. Gao, L. Yang, R. Yu, F. Li and C. Jin, The superconductivity at 18 K in LiFeAs system, *Solid State Commun.* **148**, 11–12, 538–540 (2008).

[103] C. Chu, F. Chen, M. Gooch, A. Guloy, B. Lorenz, B. Lv, K. Sasmal, Z. Tang, J. Tapp and Y. Xue, The synthesis and characterization of LiFeAs and NaFeAs, *Physica C: Supercond.* **469**, 9–12, 326–331.

[104] M. J. Pitcher, T. Lancaster, J. D. Wright, I. Franke, A. J. Steele, P. J. Baker, F. L. Pratt, W. T. Thomas, D. R. Parker, S. J. Blundell and S. J. Clarke, Compositional Control of the Superconducting Properties of LiFeAs, *J. Am. Chem. Soc.* **132**, 30, 10467–10476 (2010).

[105] Y.-F. Li and B.-G. Liu, Striped antiferromagnetic order and electronic properties of stoichiometric LiFeAs from first-principles calculations, *Eur. Phys. J. B* **72**, 2, 153–157 (2009).

[106] Z. Li, J. S. Tse and C. Q. Jin, Crystal, spin, and electronic structure of the superconductor LiFeAs, *Phys. Rev. B* **80**, 092503 (2009).

[107] X. Zhang, H. Wang and Y. Ma, First-principles study of the magnetic, structural and electronic properties of LiFeAs, *J. Phys.: Condens. Matter* **22**, 4, 046006 (2010).

[108] M. Mito, M. J. Pitcher, W. Crichton, G. Garbarino, P. J. Baker, S. J. Blundell, P. Adamson, D. R. Parker and S. J. Clarke, Response of Superconductivity and Crystal Structure of LiFeAs to Hydrostatic Pressure, *J. Am. Chem. Soc.* **131**, 8, 2986–2992 (2009).

[109] S. J. Zhang, X. C. Wang, R. Sammynaiken, J. S. Tse, L. X. Yang, Z. Li, Q. Q. Liu, S. Desgreniers, Y. Yao, H. Z. Liu and C. Q. Jin, Effect of pressure on the iron arsenide superconductor Li_xFeAs (x=0.8,1.0,1.1), *Phys. Rev. B* **80**, 014506 (2009).

[110] F. L. Pratt, P. J. Baker, S. J. Blundell, T. Lancaster, H. J. Lewtas, P. Adamson, M. J. Pitcher, D. R. Parker and S. J. Clarke, Enhanced superfluid stiffness, lowered superconducting transition temperature, and field-induced magnetic state of the pnictide superconductor LiFeAs, *Phys. Rev. B* **79**, 052508 (2009).

[111] S. V. Borisenko, V. B. Zabolotnyy, D. V. Evtushinsky, T. K. Kim, I. V. Morozov, A. N. Yaresko, A. A. Kordyuk, G. Behr, A. Vasiliev, R. Follath and B. Büchner, Superconductivity without Nesting in LiFeAs, *Phys. Rev. Lett.* **105**, 067002 (2010).

[112] A. Lankau, K. Koepernik, S. Borisenko, V. Zabolotnyy, B. Büchner, J. van den Brink and H. Eschrig, Absence of surface states for LiFeAs investigated using density functional calculations, *Phys. Rev. B* **82**, 184518 (2010).

[113] P. M. R. Brydon, M. Daghofer, C. Timm and J. van den Brink, Theory of magnetism and triplet superconductivity in LiFeAs, *Phys. Rev. B* **83**, 060501 (2011).

[114] A. E. Taylor, M. J. Pitcher, R. A. Ewings, T. G. Perring, S. J. Clarke and A. T. Boothroyd, Antiferromagnetic spin fluctuations in LiFeAs observed by neutron scattering, *Phys. Rev. B* **83**, 220514 (2011).

[115] M. Zinkin, E. Farhi and D. McMorrow, Mfit, see: http://www.ill.eu/?id=2304. Updated version by R. Coldea.

[116] P. Jeglič, A. Potočnik, M. Klanjšek, M. Bobnar, M. Jagodič, K. Koch, H. Rosner, S. Margadonna, B. Lv, A. M. Guloy and D. Arčon, ^{75}As nuclear magnetic resonance study of antiferromagnetic fluctuations in the normal state of LiFeAs, *Phys. Rev. B* **81**, 140511 (2010).

[117] L. Ma, J. Zhang, G. F. Chen and W. Yu, NMR evidence of strongly correlated superconductivity in LiFeAs: Tuning toward a spin-density-wave ordering, *Phys. Rev. B* **82**, 180501 (2010).

[118] Z. Li, Y. Ooe, X.-C. Wang, Q.-Q. Liu, C.-Q. Jin, M. Ichioka and G.-q. Zheng, ^{75}As NQR and NMR Studies of Superconductivity and Electron Correlations in Iron Arsenide LiFeAs, *J. Phys. Soc. Jpn.* **79**, 8, 083702 (2010).

[119] C. Platt, R. Thomale and W. Hanke, Superconducting state of the iron pnictide LiFeAs: A combined density-functional and functional-renormalization-group study, *Phys. Rev. B* **84**, 235121 (2011).

[120] J. D. Wright, M. J. Pitcher, W. Trevelyan-Thomas, T. Lancaster, P. J. Baker, F. L. Pratt, S. J. Clarke and S. J. Blundell, Magnetic fluctuations and spin freezing in nonsuperconducting LiFeAs derivatives, *Phys. Rev. B* **88**, 060401 (2013).

[121] Y. J. Song, J. S. Ghim, J. H. Yoon, K. J. Lee, M. H. Jung, H.-S. Ji, J. H. Shim, Y. Bang and Y. S. Kwon, Small anisotropy of the lower critical field and the $s_{\pm}$-wave two-gap feature in single-crystal LiFeAs, *Europhys. Lett.* **94**, 5, 57008 (2011).

[122] K. Cho, H. Kim, M. A. Tanatar, Y. J. Song, Y. S. Kwon, W. A. Coniglio, C. C. Agosta, A. Gurevich and R. Prozorov, Anisotropic upper critical field and possible Fulde-Ferrel-Larkin-Ovchinnikov state in the stoichiometric pnictide superconductor LiFeAs, *Phys. Rev. B* **83**, 060502 (2011).

[123] M. Wang, X. C. Wang, D. L. Abernathy, L. W. Harriger, H. Q. Luo, Y. Zhao, J. W. Lynn, Q. Q. Liu, C. Q. Jin, C. Fang, J. Hu and P. Dai, Antiferromagnetic spin excitations in single crystals of nonsuperconducting Li$_{1-x}$FeAs, *Phys. Rev. B* **83**, 220515 (2011).

[124] J. Knolle, V. B. Zabolotnyy, I. Eremin, S. V. Borisenko, N. Qureshi, M. Braden, D. V. Evtushinsky, T. K. Kim, A. A. Kordyuk, S. Sykora, C. Hess, I. V. Morozov, S. Wurmehl, R. Moessner and B. Büchner, Incommensurate magnetic fluctuations and Fermi surface topology in LiFeAs, *Phys. Rev. B* **86**, 174519 (2012).

[125] C. Putzke, A. I. Coldea, I. Guillamón, D. Vignolles, A. McCollam, D. LeBoeuf, M. D. Watson, I. I. Mazin, S. Kasahara, T. Terashima, T. Shibauchi, Y. Matsuda and A. Carrington, de Haas-van Alphen Study of the Fermi Surfaces of Superconducting LiFeP and LiFeAs, *Phys. Rev. Lett.* **108**, 047002 (2012).

[126] Y. Kamihara, H. Hiramatsu, M. Hirano, R. Kawamura, H. Yanagi, T. Kamiya and H. Hosono, Iron-Based Layered Superconductor: LaOFeP, *J. Am. Chem. Soc.* **128**, 31, 10012–10013 (2006).

[127] T. M. McQueen, M. Regulacio, A. J. Williams, Q. Huang, J. W. Lynn, Y. S. Hor, D. V. West, M. A. Green and R. J. Cava, Intrinsic properties of stoichiometric LaFePO, *Phys. Rev. B* **78**, 024521 (2008).

[128] H. Ogino, Y. Matsumura, Y. Katsura, K. Ushiyama, S. Horii, K. Kishio and J. Shimoyama, Superconductivity at $17\,\mathrm{K}$ in $(Fe_2P_2)(Sr_4Sc_2O_6)$: a new superconducting layered pnictide oxide with a thick perovskite oxide layer, *Supercond. Sci. Technol.* **22**, 7, 075008 (2009).

[129] Z. Deng, X. C. Wang, Q. Q. Liu, S. J. Zhang, Y. X. Lv, J. L. Zhu, R. C. Yu and C. Q. Jin, A new 111 type iron pnictide superconductor LiFeP, *Europhys. Lett.* **87**, 3, 37004 (2009).

[130] K. Mydeen, E. Lengyel, Z. Deng, X. C. Wang, C. Q. Jin and M. Nicklas, Temperature-pressure phase diagram of the superconducting iron pnictide LiFeP, *Phys. Rev. B* **82**, 014514 (2010).

[131] C. W. Hicks, T. M. Lippman, M. E. Huber, J. G. Analytis, J.-H. Chu, A. S. Erickson, I. R. Fisher and K. A. Moler, Evidence for a Nodal Energy Gap in the Iron-Pnictide Superconductor LaFePO from Penetration Depth Measurements by Scanning SQUID Susceptometry, *Phys. Rev. Lett.* **103**, 127003 (2009).

[132] J. D. Fletcher, A. Serafin, L. Malone, J. G. Analytis, J.-H. Chu, A. S. Erickson, I. R. Fisher and A. Carrington, Evidence for a Nodal-Line Superconducting State in LaFePO, *Phys. Rev. Lett.* **102**, 147001 (2009).

[133] M. Sutherland, J. Dunn, W. H. Toews, E. O'Farrell, J. Analytis, I. Fisher and R. W. Hill, Low-energy quasiparticles probed by heat transport in the iron-based superconductor LaFePO, *Phys. Rev. B* **85**, 014517 (2012).

[134] K. A. Yates, I. T. M. Usman, K. Morrison, J. D. Moore, A. M. Gilbertson, A. D. Caplin, L. F. Cohen, H. Ogino and J. Shimoyama, Evidence for nodal superconductivity in $Sr_2ScFePO_3$, *Supercond. Sci. Technol.* **23**, 2, 022001 (2010).

[135] K. Hashimoto, S. Kasahara, R. Katsumata, Y. Mizukami, M. Yamashita, H. Ikeda, T. Terashima, A. Carrington, Y. Matsuda and T. Shibauchi, Nodal versus Nodeless Behaviors of the Order Parameters of LiFeP and LiFeAs Superconductors from Magnetic Penetration-Depth Measurements, *Phys. Rev. Lett.* **108**, 047003 (2012).

[136] T. A. Maier, S. Graser, D. J. Scalapino and P. Hirschfeld, Neutron scattering resonance and the iron-pnictide superconducting gap, *Phys. Rev. B* **79**, 134520 (2009).

[137] M. Ishikado, Y. Nagai, K. Kodama *et al.*, $s_{\pm}$-like spin resonance in the iron-based nodal superconductor $BaFe_2(As_{0.65}P_{0.35})_2$ observed using inelastic neutron scattering, *Phys. Rev. B* **84**, 144517 (2011).

[138] M. M. Qazilbash, J. J. Hamlin, R. E. Baumbach, L. Zhang, D. J. Singh, M. B. Maple and D. N. Basov, Electronic correlations in the iron pnictides, *Nature Phys.* **5**, 9, 647–650 (2009).

[139] S. Kasahara, K. Hashimoto, H. Ikeda, T. Terashima, Y. Matsuda and T. Shibauchi, Contrasts in electron correlations and inelastic scattering between LiFeP and LiFeAs revealed by charge transport, *Phys. Rev. B* **85**, 060503 (2012).

[140] Y. Nakai, K. Ishida, Y. Kamihara, M. Hirano and H. Hosono, Spin Dynamics in Iron-Based Layered Superconductor $(La_{0.87}Ca_{0.13})FePO$ Revealed by ^{31}P and ^{139}La NMR Studies, *Phys. Rev. Lett.* **101**, 077006 (2008).

[141] J. Carlo, Y. Uemura, T. Goko *et al.*, Static Magnetic Order and Superfluid Density of RFeAs(O,F) (R=La,Nd,Ce) and LaFePO Studied by Muon Spin Relaxation: Unusual Similarities with the Behavior of Cuprate Superconductors, *Phys. Rev. Lett.* **102**, 087001 (2009).

[142] R. Thomale, C. Platt, W. Hanke and B. A. Bernevig, Mechanism for Explaining Differences in the Order Parameters of FeAs-Based and FeP-Based Pnictide Superconductors, *Phys. Rev. Lett.* **106**, 187003 (2011).

[143] A. E. Taylor, R. A. Ewings, T. G. Perring, D. R. Parker, J. Ollivier, S. J. Clarke and A. T. Boothroyd, Absence of strong magnetic fluctuations in FeP-based systems LaFePO and Sr_2ScO_3FeP, *J. Phys.: Condens. Matter* **25**, 42, 425701 (2013).

[144] Y. Kamihara, M. Hirano, H. Yanagi, T. Kamiya, Y. Saitoh, E. Ikenaga, K. Kobayashi and H. Hosono, Electromagnetic properties and electronic structure of the iron-based layered superconductor LaFePO, *Phys. Rev. B* **77**, 214515 (2008).

[145] K. Kayanuma, H. Hiramatsu, M. Hirano, R. Kawamura, H. Yanagi, T. Kamiya and H. Hosono, Apparent bipolarity and Seebeck sign inversion in a layered semiconductor: LaZnOP, *Phys. Rev. B* **76**, 195325 (2007).

[146] M. Reehuis and W. Jeitschko, Structure and magnetic properties of the phosphides $CaCo_2P_2$ and LnT_2P_2 with $ThCr_2Si_2$ structure and LnTP with PbFCl structure (Ln = Lanthanoids, T = Fe, Co, Ni), *J. Phys. Chem. Solids* **51**, 8, 961–968 (1990).

[147] D. H. Lu, M. Yi, S.-K. Mo, A. S. Erickson, J. Analytis, J.-H. Chu, D. J. Singh, Z. Hussain, T. H. Geballe, I. R. Fisher and Z.-X. Shen, Electronic structure of the iron-based superconductor LaOFeP, *Nature* **455**, 7209, 81–84 (2008).

[148] I. R. Shein and A. L. Ivanovskii, Structural and electronic properties of the 17 K superconductor $Sr_2ScFePO_3$ in comparison to $Sr_2ScFeAsO_3$ from first principles calculations, *Phys. Rev. B* **79**, 245115 (2009).

[149] H. Nakamura and M. Machida, Highly Two-dimensional Electronic Structure and Strong Fermi-Surface Nesting of the Iron-Based Superconductor $Sr_2ScFePO_3$: A First-Principles Study, *J. Phys. Soc. Jpn.* **79**, 1, 013705 (2010).

[150] M.-H. Julien, Enhanced Low-Energy Spin Dynamics with Diffusive Character in the Iron-Based Superconductor $(La_{0.87}Ca_{0.13})FePO$: Analogy with High T_c Cuprates, *J. Phys. Soc. Jpn.* **77**, 12, 125002 (2008).

[151] S. L. Skornyakov, N. A. Skorikov, A. V. Lukoyanov, A. O. Shorikov and V. I. Anisimov, LDA+DMFT spectral functions and effective electron mass enhancement in the superconductor LaFePO, *Phys. Rev. B* **81**, 174522 (2010).

[152] K. Matan, S. Ibuka, R. Morinaga, S. Chi, J. W. Lynn, A. D. Christianson, M. D. Lumsden and T. J. Sato, Doping dependence of spin dynamics in electron-doped $Ba(Fe_{1-x}Co_x)_2As_2$, *Phys. Rev. B* **82**, 054515 (2010).

[153] S. Wakimoto, K. Kodama, M. Ishikado, M. Matsuda, R. Kajimoto, M. Arai, K. Kakurai, F. Esaka, A. Iyo, H. Kito, H. Eisaki and S.-i. Shamoto, Degradation of Superconductivity and Spin Fluctuations by Electron Overdoping in $LaFeAsO_{1-x}F_x$, *J. Phys. Soc. Jpn.* **79**, 7, 074715 (2010).

[154] J. Guo, S. Jin, G. Wang, S. Wang, K. Zhu, T. Zhou, M. He and X. Chen, Superconductivity in the iron selenide $K_xFe_2Se_2$ ($0 \leq x \leq 1.0$), *Phys. Rev. B* **82**, 180520 (2010).

[155] A. F. Wang, J. J. Ying, Y. J. Yan, R. H. Liu, X. G. Luo, Z. Y. Li, X. F. Wang, M. Zhang, G. J. Ye, P. Cheng, Z. J. Xiang and X. H. Chen, Superconductivity at 32 K in single-crystalline $Rb_xFe_{2-y}Se_2$, *Phys. Rev. B* **83**, 060512 (2011).

[156] A. Krzton-Maziopa, Z. Shermadini, E. Pomjakushina, V. Pomjakushin, M. Bendele, A. Amato, R. Khasanov, H. Luetkens and K. Conder, Synthesis and crystal growth of $Cs_{0.8}(FeSe_{0.98})_2$: a new iron-based superconductor with $T_c = 27$ K, *J. Phys.: Condens. Matter* **23**, 5, 052203 (2011).

[157] M.-H. Fang, H.-D. Wang, C.-H. Dong, Z.-J. Li, C.-M. Feng, J. Chen and H. Q. Yuan, Fe-based superconductivity with $T_c = 31$ K bordering an antiferromagnetic insulator in $(TI,K)Fe_xSe_2$, *Europhys. Lett.* **94**, 27009 (2011).

[158] W. Bao, Q. Huang, G. Chen, D. Wang, J. He and Y. Qiu, A Novel Large Moment Antiferromagnetic Order in $K_{0.8}Fe_{1.6}Se_2$ Superconductor, *Chin. Phys. Lett.* **28**, 8, 086104 (2011).

[159] Y. Zhang, L. X. Yang, M. Xu *et al.*, Nodeless superconducting gap in $A_x\text{Fe}_2\text{Se}_2$ ($A =$K,Cs) revealed by angle-resolved photoemission spectroscopy, *Nat. Mater.* **10**, 4, 273–277 (2011).

[160] T. Qian, X. P. Wang, W. C. Jin, P. Zhang, P. Richard, G. Xu, X. Dai, Z. Fang, J. G. Guo, X. L. Chen and H. Ding, Absence of a Holelike Fermi Surface for the Iron-Based $\text{K}_{0.8}\text{Fe}_{1.7}\text{Se}_2$ Superconductor Revealed by Angle-Resolved Photoemission Spectroscopy, *Phys. Rev. Lett.* **106**, 187001 (2011).

[161] V. Y. Pomjakushin, D. V. Sheptyakov, E. V. Pomjakushina, A. Krzton-Maziopa, K. Conder, D. Chernyshov, V. Svitlyk and Z. Shermadini, Iron-vacancy superstructure and possible room-temperature antiferromagnetic order in superconducting $\text{Cs}_y\text{Fe}_{2-x}\text{Se}_2$, *Phys. Rev. B* **83**, 144410 (2011).

[162] V. Y. Pomjakushin, E. V. Pomjakushina, A. Krzton-Maziopa, K. Conder and Z. Shermadini, Room temperature antiferromagnetic order in superconducting $X_y\text{Fe}_{2-x}\text{Se}_2$ ($X =$Rb, K): a neutron powder diffraction study, *J. Phys.: Condens. Matter* **23**, 15, 156003 (2011).

[163] M. Wang, M. Wang, G. N. Li *et al.*, Antiferromagnetic order and superlattice structure in nonsuperconducting and superconducting $\text{Rb}_y\text{Fe}_{1.6+x}\text{Se}_2$, *Phys. Rev. B* **84**, 094504 (2011).

[164] F. Ye, S. Chi, W. Bao, X. F. Wang, J. J. Ying, X. H. Chen, H. D. Wang, C. H. Dong and M. Fang, Common Crystalline and Magnetic Structure of Superconducting $A_2\text{Fe}_4\text{Se}_5$ ($A=$K,Rb,Cs,Tl) Single Crystals Measured Using Neutron Diffraction, *Phys. Rev. Lett.* **107**, 137003 (2011).

[165] Z. Shermadini, A. Krzton-Maziopa, M. Bendele, R. Khasanov, H. Luetkens, K. Conder, E. Pomjakushina, S. Weyeneth, V. Pomjakushin, O. Bossen and A. Amato, Coexistence of Magnetism and Superconductivity in the Iron-Based Compound $\text{Cs}_{0.8}(\text{FeSe}_{0.98})_2$, *Phys. Rev. Lett.* **106**, 117602 (2011).

[166] D. A. Torchetti, M. Fu, D. C. Christensen, K. J. Nelson, T. Imai, H. C. Lei and C. Petrovic, ^{77}Se NMR investigation of the $\text{K}_x\text{Fe}_{2-y}\text{Se}_2$ high-T_c superconductor ($T_c = 33\,\text{K}$), *Phys. Rev. B* **83**, 104508 (2011).

[167] W. Yu, L. Ma, J. B. He, D. M. Wang, T. L. Xia, G. F. Chen and W. Bao, ^{77}Se NMR Study of the Pairing Symmetry and the Spin Dynamics in $\text{K}_y\text{Fe}_{2-x}\text{Se}_2$, *Phys. Rev. Lett.* **106**, 197001 (2011).

[168] L. Ma, G. F. Ji, J. Zhang, J. B. He, D. M. Wang, G. F. Chen, W. Bao and W. Yu, Superconducting and normal-state properties of single-crystalline $\text{Tl}_{0.47}\text{Rb}_{0.34}\text{Fe}_{1.63}\text{Se}_2$ as seen via ^{77}Se and ^{87}Rb NMR, *Phys. Rev. B* **83**, 174510 (2011).

[169] H. Kotegawa, Y. Hara, H. Nohara, H. Tou, Y. Mizuguchi, H. Takeya and Y. Takano, Possible Superconducting Symmetry and Magnetic Correlations in $K_{0.8}Fe_2Se_2$: A ^{77}Se-NMR Study, *J. Phys. Soc. Jpn.* **80**, 043708 (2011).

[170] T. Das and A. V. Balatsky, Modulated superconductivity due to vacancy and magnetic order in $A_yFe_{2-x/2}Se_2$ [$A =$Cs, K, (Tl,Rb), (Tl,K)] iron-selenide superconductors, *Phys. Rev. B* **84**, 115117 (2011).

[171] X. W. Yan, M. Gao, Z. Y. Lu and T. Xiang, Electronic Structures and Magnetic Order of Ordered-Fe-Vacancy Ternary Iron Selenides $TlFe_{1.5}Se_2$ and $AFe_{1.5}Se_2$ ($A =$K, Rb, or Cs), *Phys. Rev. Lett.* **106**, 087005 (2011).

[172] G. M. Zhang, Z. Y. Lu and T. Xiang, Superconductivity mediated by the antiferromagnetic spin wave in chalcogenide iron-based superconductors, *Phys. Rev. B* **84**, 052502 (2011).

[173] A. Charnukha, J. Deisenhofer, D. Pröpper, M. Schmidt, Z. Wang, Y. Goncharov, A. N. Yaresko, V. Tsurkan, B. Keimer, A. Loidl and A. V. Boris, Optical conductivity of superconducting $Rb_2Fe_4Se_5$ single crystals, *Phys. Rev. B* **85**, 100504(R) (2012).

[174] A. Ricci, N. Poccia, G. Campi, B. Joseph, G. Arrighetti, L. Barba, M. Reynolds, M. Burghammer, H. Takeya, Y. Mizuguchi, Y. Takano, M. Colapietro, N. L. Saini and A. Bianconi, Nanoscale phase separation in the iron chalcogenide superconductor $K_{0.8}Fe_{1.6}Se_2$ as seen via scanning nanofocused x-ray diffraction, *Phys. Rev. B* **84**, 060511 (2011).

[175] F. Chen, M. Xu, Q. Q. Ge, Y. Zhang, Z. R. Ye, L. X. Yang, J. Jiang, B. P. Xie, R. C. Che, M. Zhang, A. F. Wang, X. H. Chen, D. W. Shen, J. P. Hu and D. L. Feng, Electronic Identification of the Parental Phases and Mesoscopic Phase Separation of $K_xFe_{2-y}Se_2$ Superconductors, *Phys. Rev. X* **1**, 021020 (2011).

[176] V. Ksenofontov, G. Wortmann, S. A. Medvedev, V. Tsurkan, J. Deisenhofer, A. Loidl and C. Felser, Phase separation in superconducting and antiferromagnetic $Rb_{0.8}Fe_{1.6}Se_2$ probed by Mössbauer spectroscopy, *Phys. Rev. B* **84**, 180508 (2011).

[177] Y. Texier, J. Deisenhofer, V. Tsurkan, A. Loidl, D. S. Inosov, G. Friemel and J. Bobroff, NMR Study in the Iron-Selenide $Rb_{0.74}Fe_{1.6}Se_2$: Determination of the Superconducting Phase as Iron Vacancy-Free $Rb_{0.3}Fe_2Se_2$, *Phys. Rev. Lett.* **108**, 237002 (2012).

[178] S. C. Speller, T. B. Britton, G. M. Hughes, A. Krzton-Maziopa, E. Pomjakushina, K. Conder, A. T. Boothroyd and C. R. M. Grovenor, Microstructural analysis of phase separation in iron chalcogenide superconductors, *Supercond. Sci. Tech.* **25**, 8, 084023 (2012).

[179] S. Landsgesell, D. Abou-Ras, T. Wolf, D. Alber and K. Prokeš, Direct evidence of chemical and crystallographic phase separation in $K_{0.65}Fe_{1.74}Se_2$, *Phys. Rev. B* **86**, 224502 (2012).

[180] R. H. Yuan, T. Dong, Y. J. Song, P. Zheng, G. F. Chen, J. P. Hu, J. Q. Li and N. L. Wang, Nanoscale phase separation of antiferromagnetic order and superconductivity in $K_{0.75}Fe_{1.75}Se_2$, *Sci. Rep.* **2**, 221 (2012).

[181] A. M. Zhang, J. H. Xiao, Y. S. Li, J. B. He, D. M. Wang, G. F. Chen, B. Normand, Q. M. Zhang and T. Xiang, Two-magnon Raman scattering in $A_{0.8}Fe_{1.6}Se_2$ systems (A =K, Rb, Cs, and Tl): Competition between superconductivity and antiferromagnetic order, *Phys. Rev. B* **85**, 214508 (2012).

[182] A. Charnukha, A. Cvitkovic, T. Prokscha, D. Pröpper, N. Ocelic, A. Suter, Z. Salman, E. Morenzoni, J. Deisenhofer, V. Tsurkan, A. Loidl, B. Keimer and A. V. Boris, Nanoscale layering of antiferromagnetic and superconducting phases in $Rb_2Fe_4Se_5$ single crystals, *Phys. Rev. Lett.* **109**, 017003 (2012).

[183] C. N. Wang, P. Marsik, R. Schuster, A. Dubroka, M. Rössle, C. Niedermayer, G. D. Varma, A. F. Wang, X. H. Chen, T. Wolf and C. Bernhard, Macroscopic phase segregation in superconducting $K_{0.73}Fe_{1.67}Se_2$ as seen by muon spin rotation and infrared spectroscopy, *Phys. Rev. B* **85**, 214503 (2012).

[184] W. Li, H. Ding, P. Deng, K. Chang, C. Song, K. He, L. Wang, X. Ma, J. Hu, X. Chen and Q. Xue, Phase separation and magnetic order in K-doped iron selenide superconductor, *Nat. Phys.* **8**, 2, 126–130 (2012).

[185] W. Li, H. Ding, Z. Li, P. Deng, K. Chang, K. He, S. Ji, L. Wang, X. Ma, J.-P. Hu, X. Chen and Q.-K. Xue, KFe_2Se_2 is the Parent Compound of K-Doped Iron Selenide Superconductors, *Phys. Rev. Lett.* **109**, 057003 (2012).

[186] D. P. Shoemaker, D. Y. Chung, H. Claus, M. C. Francisco, S. Avci, A. Llobet and M. G. Kanatzidis, Phase relations in $K_xFe_{2-y}Se_2$ and the structure of superconducting $K_xFe_2Se_2$ via high-resolution synchrotron diffraction, *Phys. Rev. B* **86**, 184511 (2012).

[187] V. Y. Pomjakushin, A. Krzton-Maziopa, E. V. Pomjakushina, K. Conder, D. Chernyshov, V. Svitlyk and A. Bosak, Intrinsic crystal phase separation in the antiferromagnetic superconductor $Rb_yFe_{2-x}Se_2$: a diffraction study, *J. Phys.: Condens. Matter* **24**, 43, 435701 (2012).

[188] M. Wang, C. Fang, D. Yao, G. Tan, L. W. Harriger, Y. Song, T. Netherton, C. Zhang, M. Wang, M. B. Stone, W. Tian, J. Hu and P. Dai, Spin waves and magnetic exchange interactions in insulating $Rb_{0.89}Fe_{1.58}Se_2$, *Nat. Commun.* **2**, 580 (2011).

[189] J. T. Park, G. Friemel, Y. Li, J. Kim, V. Tsurkan, J. Deisenhofer, H. Krug von Nidda, A. Loidl, A. Ivanov, B. Keimer and D. S. Inosov, Magnetic Resonant Mode

in the Low-Energy Spin-Excitation Spectrum of Superconducting $Rb_2Fe_4Se_5$ Single Crystals, *Phys. Rev. Lett.* **107**, 177005 (2011).

[190] G. Friemel, J. T. Park, T. A. Maier, V. Tsurkan, Y. Li, J. Deisenhofer, H. A. Krug von Nidda, A. Loidl, A. Ivanov, B. Keimer and D. S. Inosov, Reciprocal-space structure and dispersion of the magnetic resonant mode in the superconducting phase of $Rb_xFe_{2-y}Se_2$ single crystals, *Phys. Rev. B* **85**, 140511 (2012).

[191] T. A. Maier, S. Graser, P. J. Hirschfeld and D. J. Scalapino, *d*-wave pairing from spin fluctuations in the $K_xFe_{2-y}Se_2$ superconductors, *Phys. Rev. B* **83**, 100515 (2011).

[192] I. I. Mazin, Symmetry analysis of possible superconducting states in $K_xFe_ySe_2$ superconductors, *Phys. Rev. B* **84**, 024529 (2011).

[193] M. Wang, C. Li, D. L. Abernathy, Y. Song, S. V. Carr, X. Lu, S. Li, Z. Yamani, J. Hu, T. Xiang and P. Dai, Neutron scattering studies of spin excitations in superconducting $Rb_{0.82}Fe_{1.68}Se_2$, *Phys. Rev. B* **86**, 024502 (2012).

[194] A. E. Taylor, R. A. Ewings, T. G. Perring, J. S. White, P. Babkevich, A. Krzton-Maziopa, E. Pomjakushina, K. Conder and A. T. Boothroyd, Spin-wave excitations and superconducting resonant mode in $Cs_xFe_{2-y}Se_2$, *Phys. Rev. B* **86**, 094528 (2012).

[195] C. Fang, Y.-L. Wu, R. Thomale, B. A. Bernevig and J. Hu, Robustness of s-Wave Pairing in Electron-Overdoped $A_{1-y}Fe_{2-x}Se_2$ (A =K,Cs), *Phys. Rev. X* **1**, 011009 (2011).

[196] R. Yu, J.-X. Zhu and Q. Si, Mott Transition in Modulated Lattices and Parent Insulator of $(K,Tl)_yFe_xSe_2$ Superconductors, *Phys. Rev. Lett.* **106**, 186401 (2011).

[197] R. Yu and Q. Si, Orbital-Selective Mott Phase in Multiorbital Models for Alkaline Iron Selenides $K_{1-x}Fe_{2-y}Se_2$, *Phys. Rev. Lett.* **110**, 146402 (2013).

[198] M. Yi, D. H. Lu, R. Yu *et al.*, Observation of Temperature-Induced Crossover to an Orbital-Selective Mott Phase in $A_xFe_{2-y}Se_2$ (A =K, Rb) Superconductors, *Phys. Rev. Lett.* **110**, 067003 (2013).

[199] T. Das and A. V. Balatsky, Stripes, spin resonance, and nodeless *d*-wave pairing symmetry in Fe_2Se_2-based layered superconductors, *Phys. Rev. B* **84**, 014521 (2011).

[200] F. Wang, F. Yang, M. Gao, Z. Lu, T. Xiang and D. Lee, The electron pairing of $K_xFe_{2-y}Se_2$, *Europhys. Lett.* **93**, 5, 57003 (2011).

[201] T. Zhou and Z. D. Wang, A minimum single-band model for low-energy excitations in superconducting $A_xFe_{2-y}Se_2$, *Eur. J. Phys. B* **85**, 7 (2012).

[202] T. A. Maier, P. J. Hirschfeld and D. J. Scalapino, Evolution of the neutron resonances in AFe$_2$Se$_2$, *Phys. Rev. B* **86**, 094514 (2012).

[203] E. Dagotto, Colloquium: The unexpected properties of alkali metal iron selenide superconductors, *Rev. Mod. Phys.* **85**, 849–867 (2013).

[204] G. Friemel, W. P. Liu, E. A. Goremychkin, Y. Liu, J. T. Park, O. Sobolev, C. T. Lin, B. Keimer and D. S. Inosov, Conformity of spin fluctuations in alkali-metal iron selenide superconductors inferred from the observation of a magnetic resonant mode in K$_x$Fe$_{2-y}$Se$_2$, *Europhys. Lett.* **99**, 6, 67004 (2012).

[205] D. S. Inosov, J. T. Park, P. Bourges, D. L. Sun, Y. Sidis, A. Schneidewind, K. Hradil, D. Haug, C. T. Lin, B. Keimer and V. Hinkov, Normal-state spin dynamics and temperature-dependent spin-resonance energy in optimally doped BaFe$_{1.85}$Co$_{0.15}$As$_2$, *Nature Phys.* **6**, 12, 178–181 (2010).

[206] C. Lester, J.-H. Chu, J. G. Analytis, T. G. Perring, I. R. Fisher and S. M. Hayden, Dispersive spin fluctuations in the nearly optimally doped superconductor Ba(Fe$_{1-x}$Co$_x$)$_2$As$_2$ ($x = 0.065$), *Phys. Rev. B* **81**, 064505 (2010).

[207] M. Liu, L. W. Harriger, H. Luo, M. Wang, R. A. Ewings, T. Guidi, H. Park, K. Haule, G. Kotliar, S. M. Hayden and P. Dai, Nature of magnetic excitations in superconducting BaFe$_{1.9}$Ni$_{0.1}$As$_2$, *Nature Phys.* **8**, 5, 376–381 (2012).

[208] D. S. Inosov, *Private Communication* (2013).

[209] T. P. Ying, X. L. Chen, G. Wang, S. F. Jin, T. T. Zhou, X. F. Lai, H. Zhang and W. Y. Wang, Observation of superconductivity at 30–46 K in A_xFe$_2$Se$_2$ ($A =$Li, Na, Ba, Sr, Ca, Yb, and Eu), *Sci. Rep.* **2**, 426 (2012).

[210] M. Burrard-Lucas, D. G. Free, S. J. Sedlmaier, J. D. Wright, S. J. Cassidy, Y. Hara, A. J. Corkett, T. Lancaster, P. J. Baker, S. J. Blundell and S. J. Clarke, Enhancement of the superconducting transition temperature of FeSe by intercalation of a molecular spacer layer, *Nat. Mater.* **12**, 1, 15–19 (2013).

[211] E. Scheidt, V. Hathwar, D. Schmitz, A. Dunbar, W. Scherer, F. Mayr, V. Tsurkan, J. Deisenhofer and A. Loidl, Superconductivity at $T_c = 44$ K in Li$_x$Fe$_2$Se$_2$(NH$_3$)$_y$, *Eur. Phys. J. B* **85**, 8, 1–5 (2012).

[212] A. Krzton-Maziopa, E. V. Pomjakushina, V. Y. Pomjakushin, F. von Rohr, A. Schilling and K. Conder, Synthesis of a new alkali metal-organic solvent intercalated iron selenide superconductor with $T_c \approx 45$ K, *J. Phys.: Condens. Matter* **24**, 38, 382202 (2012).

[213] T. Ying, X. Chen, G. Wang, S. Jin, X. Lai, T. Zhou, H. Zhang, S. Shen and W. Wang, Superconducting Phases in Potassium-Intercalated Iron Selenides, *J. Am. Chem. Soc.* **135**, 8, 2951–2954 (2013).

[214] K.-W. Yeh, T.-W. Huang, Y.-l. Huang, T.-K. Chen, F.-C. Hsu, P. M. Wu, Y.-C. Lee, Y.-Y. Chu, C.-L. Chen, J.-Y. Luo, D.-C. Yan and M.-K. Wu, Tellurium substitution effect on superconductivity of the α-phase iron selenide, *Europhys. Lett.* **84**, 3, 37002 (2008).

[215] M. H. Fang, H. M. Pham, B. Qian, T. J. Liu, E. K. Vehstedt, Y. Liu, L. Spinu and Z. Q. Mao, Superconductivity close to magnetic instability in $Fe(Se_{1-x}Te_x)_{0.82}$, *Phys. Rev. B* **78**, 224503 (2008).

[216] S. Medvedev, T. M. McQueen, I. A. Troyan, T. Palasyuk, M. I. Eremets, R. J. Cava, S. Naghavi, F. Casper, V. Ksenofontov, G. Wortmann and C. Felser, Electronic and magnetic phase diagram of β-$Fe_{1.01}Se$ with superconductivity at $36.7\,K$ under pressure, *Nat. Mater.* **8**, 8, 630–633 (2009).

[217] X.-W. Yan and M. Gao, The effect of the Wyckoff position of the K atom on the crystal structure and electronic properties of the compound KFe_2Se_2, *J. Phys.: Condens. Matter* **24**, 45, 455702 (2012).

[218] P. K. Biswas, A. Krzton-Maziopa, R. Khasanov, H. Luetkens, E. Pomjakushina, K. Conder and A. Amato, Two-Dimensional Superfluid Density in an Alkali Metal-Organic Solvent Intercalated Iron Selenide Superconductor $Li(C_5H_5N)_{0.2}Fe_2Se_2$, *Phys. Rev. Lett.* **110**, 137003 (2013).

[219] A. E. Taylor, S. J. Sedlmaier, S. J. Cassidy, E. A. Goremychkin, R. A. Ewings, T. G. Perring, S. J. Clarke and A. T. Boothroyd, Spin fluctuations away from $(\pi, 0)$ in the superconducting phase of molecular-intercalated FeSe, *Phys. Rev. B* **87**, 220508 (2013).

[220] T. M. McQueen, Q. Huang, V. Ksenofontov, C. Felser, Q. Xu, H. Zandbergen, Y. S. Hor, J. Allred, A. J. Williams, D. Qu, J. Checkelsky, N. P. Ong and R. J. Cava, Extreme sensitivity of superconductivity to stoichiometry in $Fe_{1+\delta}Se$, *Phys. Rev. B* **79**, 014522 (2009).

[221] E. E. Rodriguez, C. Stock, P.-Y. Hsieh, N. P. Butch, J. Paglione and M. A. Green, Chemical control of interstitial iron leading to superconductivity in $Fe_{1+x}Te_{0.7}Se_{0.3}$, *Chem. Sci.* **2**, 9 (2011).

[222] C. Stock, E. E. Rodriguez, M. A. Green, P. Zavalij and J. A. Rodriguez-Rivera, Interstitial iron tuning of the spin fluctuations in the nonsuperconducting parent phase $Fe_{1+x}Te$, *Phys. Rev. B* **84**, 045124 (2011).

[223] C. Stock, E. E. Rodriguez and M. A. Green, Spin fluctuations and superconductivity in powders of $Fe_{1+x}Te_{0.7}Se_{0.3}$ as a function of interstitial iron concentration, *Phys. Rev. B* **85**, 094507 (2012).

[224] D. Fruchart, P. Convert, P. Wolfers, R. Madar, J. Senateur and R. Fruchart, Structure antiferroma gnetique de $Fe_{1.125}Te$ accompagnee d'une deformation monoclinique, *Mater. Res. Bull.* **10**, 3, 169–174 (1975).

[225] R. Khasanov, M. Bendele, A. Amato, P. Babkevich, A. T. Boothroyd, A. Cervellino, K. Conder, S. N. Gvasaliya, H. Keller, H.-H. Klauss, H. Luetkens, V. Pomjakushin, E. Pomjakushina and B. Roessli, *Coexistence of incommensurate magnetism and superconductivity in* $Fe_{1+y}Se_xTe_{1-x}$, *Phys. Rev. B* **80**, 140511 (2009).